The Tissue-reduced Virtual Family Models for RF-induced Heating Evaluation of Passive Medical Implants at 1.5 T and 3 T

by

Meiqi Xia

A dissertation submitted to the Department of Electrical and Computer Engineering,
Cullen College of Engineering
in partial fulfillment of the requirements for the degree of

Doctor of Philosophy

in Electrical Engineering

Committee Chair: Dr. Ji Chen

Committee Member: Dr. David R. Jackson

Committee Member: Dr. Jiefu Chen

Committee Member: Dr. Benhaddou Driss

Committee Member: Dr. Wolfgang Kainz

University of Houston

May 2022

ACKNOWLEDGMENTS

Great thanks to all the people around me for supporting me during my Ph.D. program. I really and especially appreciate my advisor Dr. Ji Chen who has always been patient and kind to me and leads and guides me during my research. I have always met problems and difficulties during the past 5 years, both in research and life. He is always there to answer my questions and teach me how to solve problems.

Moreover, I would also like to show my great appreciation to the other committee members. Dr. David Jackson, who is from the electromagnetic (EM) group, taught me many EM basic courses, such as microwave engineering, which helped me find my first job. Dr. Jiefu Chen from the same group, from him I have learned the basic knowledge about the EM waves, which established my essential understanding for my research field. Dr. Driss Benhaddou has given me significant suggestions about how to introduce and summarize my research. And Dr. Wolfgang Kainz, as a scientist from the FDA, helped me understand the FDA standard and gave me many suggestions for my journal papers.

Finally, I would also like to thank Dr. Jianfeng Zheng, the post-doc scholar in our laboratory. He has helped and taught me everything at the beginning of my joining this laboratory. And I would also thank my friends and colleagues with the most significant appreciation, Dr. Qi Zeng, Dr. Ran Guo, Dr. Rui Yang, Dr. Xiaohe Ji, Dr. Mengping Yu, Dr. Zhichao Wang, Dr. Yu Wang, Dr. Shuo Song, Dr. Qianlong Lan, Mr. Wei Hu, Mr. Jiajun Chang, Ms. Xiaolin Yang, Ms. Yongqi Xiao, Dr. Fangshi Zhu, and Ms. Yuanzhuo Liu, without your support and company, I would never finish this journey.

ABSTRACT

RF-induced heating is an important safety concern for patients with implantable medical devices under magnetic resonance imaging (MRI) scanning. The implanted device may lead to a high temperature rise near device edges and cause tissue damage. Thus, the RF-induced heating near the device needs to be properly evaluated for the safety of patients. The study in ASTM phantom and human models is adopted to evaluate the RF-induced heating near the medical implants.

To make the experiment in human models more practical, the tissue-reduced virtual family models were proposed for RF-induced heating simulation and possible experiments in the future. Simplified human body models with a reduced number of tissues were developed using the Gaussian Mixture Model (GMM). Different tissues were grouped into several clusters based on the electrical parameters. Using three human body models (the Duke, the Ella, and the FATS) from the virtual family, electromagnetic simulations were conducted for the original and simplified human models under 1.5 T and 3 T MRI systems. The electric field distributions were extracted for comparison.

To investigate the performance of the proposed tissue-reduced virtual family models on RF-induced heating evaluation for the passive device, some representative passive device systems were implanted in the original virtual family models, tissue-reduced virtual family models, and ASTM phantom for simulation. The studied device systems are the standalone screw system, the pedicle screw system, the plate and screw system, and the stent system. They were implanted in the clinical positions in the human models and in the fixed position in the ASTM phantom as required by the ASTM standard. The simulated results of specific absorption rate averaged to 1 gram (SAR_{1g}) near the device

at 1.5 T and 3 T in the human models and ASTM phantom were extracted for comparison.

Table of Contents

ACKNOWLEDGMENTS iii

ABSTRACT iv

TABLE OF CONTENTS vi

LIST OF TABLES ix

LIST OF FIGURES xii

CHAPTER 1. INTRODUCTION: THE ASTM PHANTOM AND HUMAN MODELS FOR RF-INDUCED HEATING EVALUATION 1

1.1. INTRODUCTION 1

1.2. THE STUDY IN THE ASTM PHANTOM 1

1.3. THE STUDY IN THE HUMAN MODELS 3

1.4. COMPARISON OF THE ASTM PHANTOM AND HUMAN MODELS 3

CHAPTER 2. DEVELOPMENT OF THE TISSUE-REDUCED VIRTUAL FAMILY MODELS AT 1.5 T 10

2.1. METHOD 10

2.1.1. Original human models from Virtual Family 10

2.1.2. Gaussian mixture model and three tissue cluster methods 12

2.1.3. Electromagnetic simulation setup 19

2.2. RESULTS AND DISCUSSION: A CORRELATION ANALYSIS 20

2.3. CONCLUSIONS 28

CHAPTER 3. TISSUE-REDUCED VIRTUAL FAMILY MODELS' APPLICATION ON

RF-INDUCED HEATING EVALUATION OF PASSIVE MEDICAL IMPLANTS AT 1.5 T………………. 29

3.1. INTRODUCTION 29

3.2. METHOD 32

3.2.1. Tissue-Reduced Virtual Family Models by tissue clustering method 32

3.2.2. Passive device systems 33

3.2.3. Electromagnetic simulation setup 35

3.2.4. SAR analysis 38

3.3. RESULTS AND DISCUSSION 44

3.3.1. Peak SAR_{1g} near the device comparison 44

3.3.2. SAR_{1g} distribution near the device comparison 48

3.4. CONCLUSIONS 53

CHAPTER 4. TISSUE-REDUCED VIRTUAL FAMILY MODELS AND THEIR APPLICATION ON RF-INDUCED HEATING EVALUATION OF PASSIVE MEDICAL IMPLANTS AT 3 T 55

4.1. INTRODUCTION 55

4.2. TISSUE-REDUCED VIRTUAL FAMILY MODELS FOR 3 T MRI SYSTEM 57

4.2.1. The original human models and the tissues' parameters at 3 T 57

4.2.2. Tissue-reduced virtual family models development at 3 T 60

4.2.3. Electromagnetic simulations and correlation analysis 61

4.3. TISSUE-REDUCED VIRTUAL FAMILY MODELS' APPLICATION ON RF-INDUCED HEATING EVALUATION OF PASSIVE MEDICAL IMPLANTS AT 3 T 65

4.3.1. Passive device systems and electromagnetic simulation setup 65

4.3.2. Simulated results and discussion 66

4.4. CONCLUSIONS 69

CHAPTER 5. PROGRESS OF 3D PRINTING THE TISSUE-REDUCED HUMAN MODELS FOR EXPERIMENTAL STUDY AND FUTURE WORK 71

5.1. INTRODUCTION 71

5.2. 3D PRINTING TESTING FOR HEAD'S SKIN MODEL 72

5.3. 3D PRINTING FOR HUMAN-SHAPED SHELL 74

5.4. FUTURE WORK 80

REFERENCES 83

A. APPENDIX I: CORRELATION ANALYSIS BETWEEN THE ELECTRIC FIELD OF THE ORIGINAL AND SIMPLIFIED HUMAN MODELS AT 1.5 T 94

B. APPENDIX II: THE DETAILED TISSUES IN THE TWO CLUSTERS OF THE CHOSEN TISSUE-REDUCED VIRTUAL FAMILY MODELS AT 1.5 T 118

C. APPENDIX III: CONVERGENCE CHECK FOR MESH SIZE 124

D. APPENDIX IV: UNCERTAINTY ANALYSIS 126

E. APPENDIX V: THE SAR_{1G} IN TISSUE-REDUCED HUMAN MODELS WITH AND WITHOUT Σ-SCALING VS. THE SAR_{1G} IN ORIGINAL HUMAN MODELS 129

List of Tables

Table 1-I. The simulated results in human models. 8

Table 2-I. Three tissue cluster methods. 13

Table 2-II. The correlation coefficients between the original Duke model and the chosen tissue-reduced Duke model at 1.5 T. 25

Table 2-III. The correlation coefficients between the original Ella model and the chosen tissue-reduced Ella model at 1.5 T. 26

Table 2-IV. The correlation coefficients between the original FATS model and the chosen tissue-reduced FATS model at 1.5 T. 27

Table 2-V. Detailed parameters for the chosen tissue-reduced virtual family models at 1.5 T. 28

Table 3-I. Maximum mesh sizes for the studied passive device systems. 37

Table 4-I. The electrical conductivities and relative permittivities at 1.5 T and 3 T of tissues in the Duke model. 57

Table 4-II. Detailed parameters for the chosen tissue-reduced virtual family models at 3 T. 61

Table 4-III. The correlation coefficients between the original Duke model and the chosen tissue-reduced Duke model at 3 T. 62

Table 4-IV. The correlation coefficients between the original Ella model and the chosen tissue-reduced Ella model at 3 T. 63

Table 4-V. The correlation coefficients between the original FATS model and the chosen tissue-reduced FATS model at 3 T. 64

Table 5-I. The correlation coefficients between the electric field inside the

SKIN MODEL WITH AND WITHOUT THE 5% FILLED PLA BOX. 76

TABLE 5-II. THE CORRELATION COEFFICIENTS BETWEEN THE ELECTRIC FIELD INSIDE THE SKIN MODEL WITH AND WITHOUT THE 7% FILLED PLA BOX. 77

TABLE A-I. CORRELATION COEFFICIENTS FOR THE DUKE MODEL AT 400 MM LANDMARK.. 94

TABLE A-II. CORRELATION COEFFICIENTS FOR THE DUKE MODEL AT 600 MM LANDMARK. 97

TABLE A-III. CORRELATION COEFFICIENTS FOR THE DUKE MODEL AT 800 MM LANDMARK. 99

TABLE A-IV. CORRELATION COEFFICIENTS FOR THE ELLA MODEL AT 400 MM LANDMARK. 102

TABLE A-V. CORRELATION COEFFICIENTS FOR THE ELLA MODEL AT 600 MM LANDMARK.104

TABLE A-VI. CORRELATION COEFFICIENTS FOR THE ELLA MODEL AT 800 MM LANDMARK. 107

TABLE A-VII. CORRELATION COEFFICIENTS FOR THE FATS MODEL AT 400 MM LANDMARK. 109

TABLE A-VIII. CORRELATION COEFFICIENTS FOR THE FATS MODEL AT 600 MM LANDMARK. 112

TABLE A-IX. CORRELATION COEFFICIENTS FOR THE FATS MODEL AT 800 MM LANDMARK. 114

TABLE B-I. THE DETAILED TISSUES IN THE TWO CLUSTERS AND THEIR CORRESPONDING PARAMETERS OF THE CHOSEN TISSUE-REDUCED DUKE MODELS. 118

TABLE B-II. THE DETAILED TISSUES IN THE TWO CLUSTERS AND THEIR CORRESPONDING PARAMETERS OF THE CHOSEN TISSUE-REDUCED ELLA MODELS. 119

TABLE B-III. THE DETAILED TISSUES IN THE TWO CLUSTERS AND THEIR CORRESPONDING

PARAMETERS OF THE CHOSEN TISSUE-REDUCED FATS MODELS. 121

TABLE D-I. DATA FOR COMBINED UNCERTAINTY CALCULATION AT 1.5 T.......................... 127

TABLE D-II. DATA FOR COMBINED UNCERTAINTY CALCULATION AT 3 T. 128

TABLE E-I. RESULTS FOR THE CASES WHEN THE RELATIVE ERRORS BETWEEN THE SAR_{1G} IN THE TISSUE-REDUCED HUMAN MODELS AND THE SAR_{1G} IN THE ORIGINAL HUMAN MODELS BECOME LARGER WITH THE Σ-SCALING. 131

List of Figures

Figure 1-1. ASTM phantom with a device implanted. 2

Figure 1-2. The peak SAR_{1g} near the studied worst-case device and the SAR_{1g} distributions around the device. Top:1.5 T with peak SAR_{1g} near the device as 106 W/kg; Bottom:3 T with peak SAR_{1g} near the device as 75.2 W/kg.......... 6

Figure 1-3. The two human models for simulation: Left: the girl model; Right: the FATS model. 7

Figure 1-4. (a) The positions of the human model in coil at 1.5 T (top) and at 3 T (bottom), the implants were put at the bottom, center, and top of the coil from left to right. (b) The wire closures in the human model at 1.5 T. (c) The wire closures in the human model at 3 T. 7

Figure 2-1. Scatter plots for the tissue properties at 1.5 T. 10

Figure 2-2. Volume weight for tissues. 12

Figure 2-3. AIC and BIC. 14

Figure 2-4. The scatter plots for the three cluster methods for the Duke model… 16

Figure 2-5. The scatter plots for the three cluster methods for the Ella model... 17

Figure 2-6. The scatter plots for the three cluster methods for the FATS model… 18

Figure 2-7. Three landmark positions. 20

Figure 2-8. The body regions for electric field extraction. 20

Figure 2-9. The correlation coefficients for the Duke model in terms of the

MODULE OF ELECTRIC FIELD. 23
FIGURE 2-10. THE CORRELATION COEFFICIENTS FOR THE ELLA AND FATS MODELS. 24
FIGURE 3-1. A, THE MAIN TISSUES IN THE TWO CLUSTERS OF THE TISSUE-REDUCED DUKE MODEL IN THE SEMCAD SOFTWARE. B, THE SCATTER PLOT OF THE TWO CLUSTERS FOR THE TISSUE-REDUCED DUKE MODEL. C, THE DETAILED PARAMETERS OF THE TISSUE-REDUCED VIRTUAL FAMILY HUMAN MODELS. 33
FIGURE 3-2. A, THE IMPLANTED POSITIONS OF THE STANDALONE SCREW SYSTEM. B, THE IMPLANTED POSITIONS OF THE PEDICLE SCREW SYSTEM. C, THE IMPLANTED POSITIONS OF THE PLATE AND SCREW SYSTEM. D, THE IMPLANTED POSITIONS OF THE STENT SYSTEM.. 35
FIGURE 3-3. THE STUDIED THREE LANDMARKS IN SIMULATIONS: THE IMPLANTED PASSIVE DEVICE WAS IN THE CENTER OF THE COIL IN THE Z DIRECTION (0 MM) AND MOVED BY 100 MM ALONG THE -Z (-100 MM) AND +Z (100 MM) DIRECTIONS. 36
FIGURE 3-4. A, THE ROD AND THE PHANTOM USED FOR Σ-SCALING. B, THE SAR_{1G} AT THE TOP END OF THE ROD VERSUS THE ELECTRICAL CONDUCTIVITY OF SURROUNDING GELLED-SALINE IN THE 15 MM*15 MM*15 MM CUBIC. 43
FIGURE 3-5. RESULTS OF THE SAR_{1G} FOR ALL SIMULATIONS AT THE POSITIONS OF PEAK SAR_{1G} NEAR THE IMPLANTED PASSIVE DEVICE IN THE ORIGINAL HUMAN MODELS AT 1.5 T. THE R IS THE CORRELATION COEFFICIENT, AND THE S IS THE SLOPE OF THE FITTING STRAIGHT LINE IN THE LEGEND. 47
FIGURE 3-6. COMPARISON OF THE SAR_{1G} IN TISSUE-REDUCED HUMAN MODELS AND ASTM PHANTOM WITH OR WITHOUT E-SCALING AT 1.5 T. THE R IS THE CORRELATION COEFFICIENT, AND THE S IS THE SLOPE OF THE FITTING STRAIGHT LINE IN THE LEGEND.

.... 48

FIGURE 3-7. SAR_{1G} DISTRIBUTIONS NEAR THE DEVICE FOR THE PLATE AND SCREW SYSTEM ON FIBULA UNDER 0 MM LANDMARK POSITION IN DUKE MODEL. 49

FIGURE 3-8. THE MODULI OF TANGENTIAL INCIDENT ELECTRIC FIELD ALONG DEVICES COMPARISON. 51

FIGURE 4-1. SCATTER PLOTS FOR THE TISSUE PROPERTIES AT 3 T. 60

FIGURE 4-2. RESULTS OF THE SAR_{1G} FOR ALL SIMULATIONS AT THE POSITIONS OF PEAK SAR_{1G} NEAR THE IMPLANTED PASSIVE DEVICE IN THE ORIGINAL HUMAN MODELS AT 3T. THE R IS THE CORRELATION COEFFICIENT, AND THE S IS THE SLOPE OF THE FITTING STRAIGHT LINE IN THE LEGEND. 68

FIGURE 4-3. COMPARISON OF THE SAR_{1G} IN TISSUE-REDUCED HUMAN MODELS AND ASTM PHANTOM WITH OR WITHOUT E-SCALING AT 3 T. THE R IS THE CORRELATION COEFFICIENT, AND THE S IS THE SLOPE OF THE FITTING STRAIGHT LINE IN THE LEGEND. 69

FIGURE 5-1. A, THE HEAD'S SKIN MODEL IN THE SIM4LIFE SOFTWARE PACKAGE. B, THE HEAD'S SKIN MODEL IN A 3D PRINTER SLICER SOFTWARE (ULTIMAKER CURA 4.12.1). 73

FIGURE 5-2. THE PRINTED HEAD'S SKIN MODEL. 73

FIGURE 5-3. THE 17 SEGMENTS OF THE HUMAN-SHAPED SHELL. 74

FIGURE 5-4. THE REAL PARTS AND IMAGINARY PARTS OF *X*, *Y* AND *Z* COMPONENTS OF ELECTRIC FIELD ALONG THE Z-AXIS INSIDE THE SHELL AT 400 MM LANDMARK POSITION... 78

FIGURE 5-5. THE REAL PARTS AND IMAGINARY PARTS OF *X*, *Y* AND *Z* COMPONENTS OF ELECTRIC FIELD ALONG THE Z-AXIS INSIDE THE SHELL AT 600 MM LANDMARK

POSITION... 79

FIGURE 5-6. THE REAL PARTS AND IMAGINARY PARTS OF *X*, *Y* AND *Z* COMPONENTS OF ELECTRIC FIELD ALONG THE Z-AXIS INSIDE THE SHELL AT 800 MM LANDMARK POSITION... 80

FIGURE C-1. THE DEVICE USED FOR MESH STUDY AND RESULTS OF THE PEAK SAR_{1G} NEAR THE DEVICE. 124

FIGURE C-2. RESULTS OF THE MODULUS OF THE TANGENTIAL INCIDENT ELECTRIC FIELD IN ASTM PHANTOM. 125

FIGURE E-1. THE SAR_{1G} IN THE TISSUE-REDUCED HUMAN MODELS WITH AND WITHOUT *Σ*-SCALING VS. THE SAR_{1G} IN THE ORIGINAL HUMAN MODELS. 130

Chapter 1. INTRODUCTION: THE ASTM PHANTOM AND HUMAN MODELS FOR RF-INDUCED HEATING EVALUATION

1.1. Introduction

There are some common safety concerns for the MRI examination due to the interaction between electromagnetic field and medical device, such as displacement force, torque, RF heating, image artifact, and so on [1]. The emphasis of this study is on RF-induced heating. The medical device made of metallic materials may induce quite high heating to burn the human tissues [2], [3]. Related research about the RF-induced heating of the implanted device has been conducted on passive devices, such as the stent system [4] and the external fixation system [5], and active devices, such as the DBS [6] and the pacemaker [7] [8]. These studies reveal that the RF-induced heating could lead to a quite high temperature rise near the device, which is harmful to the human body. To assure the safety of the patients undertaking MRI examination, the RF-induced heating needs to be properly evaluated, and the medical device needs to be labeled as MR safe, MR conditional, or MR unsafe according to the ASTM standard [1], [9].

1.2. The study in the ASTM phantom

Traditionally, to evaluate the RF-induced heating for medical implants, the ASTM phantom is often used for both simulation and experiment to obtain the prediction [9], [10]. Previous research was conducted in the ASTM phantom for RF-induced heating evaluation with simulation [11] and experiments [12]. The structure of the ASTM phantom and an example of a device in the phantom are shown in Figure 1-1 [13]. The ASTM phantom has a simple shape and consists of a shell that is uniformly filled with gelled-saline. Obviously, the ASTM phantom can be easily built in the simulation and experiment. However, the device in the ASTM phantom is placed in a fixed position as required by the ASTM standard [9], [13], where the incident electric field could be different from that of the clinical position. In addition to this, the uniformly filled gelled-saline will lead to different power dissipation compared to that of the non-uniform human tissues. Thus, the evaluated RF-induced heating from the ASTM phantom is not perfectly accurate. If we want to get more accurate results of the RF-induced heating near the device, the human models are necessary.

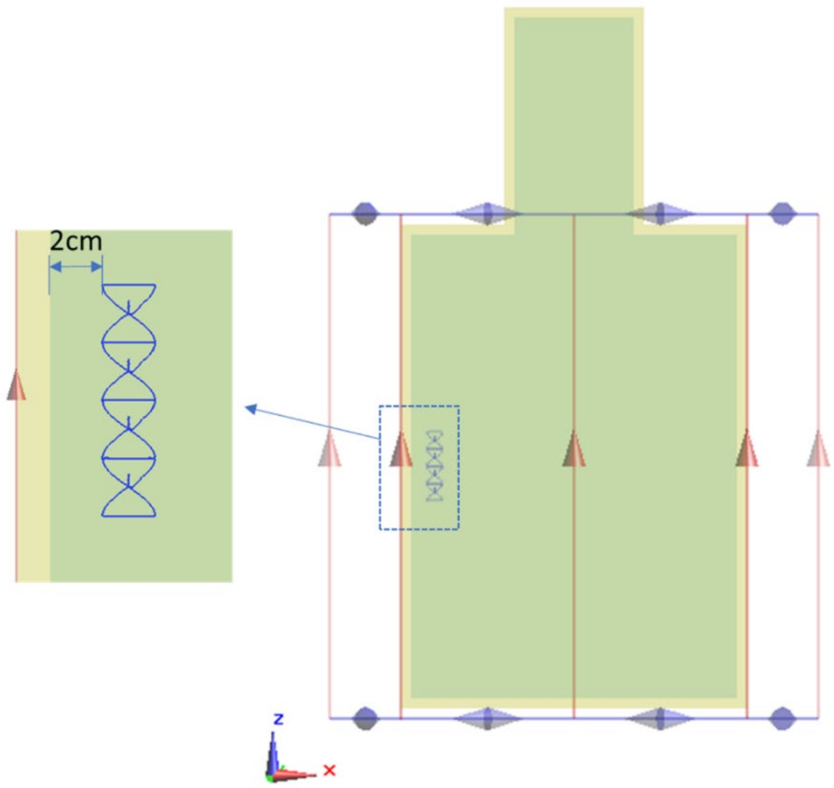

Figure 1-1. ASTM phantom with a device implanted.

1.3. The study in the human models

The 3D high-resolution realistic human models are used for accurate RF-induced heating evaluation. A commonly used series of these human models are the virtual family human models from IT'IS Foundation, Switzerland [14], [15]. The Duke, Ella, and FATS models are three representative human models from this virtual family. The duke is an adult male human model, the Ella is an adult female human model, and the FATS is an adult fat male human model. These human models consider the influence of the realistic human body's shape and the non-uniform human tissues on RF-induced heating. Research on RF-induced heating in human models is conducted mainly with numerical simulations [16], [17]. Although some experiments in human models were conducted, the used fabricated human models are greatly simplified to only keep the human shape and part of the body [18], [19].

1.4. Comparison of the ASTM phantom and human models

An earlier study has compared the simulated RF-induced heating in vitro and in vivo for a 1.5 T MRI system. This study used the plate and screws system implanted on the humerus and the femur [20]. From the results, the ASTM phantom overestimates the heating while the human models give more accurate results but are more complex for simulation setup and experiment.

Another previous research for the passive device in ASTM phantom and human models shows more details. A series of wire-based sternal closures were studied in ASTM phantom and human models [13]. Numerical simulations in

ASTM phantom were conducted using the SEMCAD (V14.8 SPEAG) software package based on the Finite-Difference Time-Domain (FD-TD) method. The RF coils operate at 64 MHz for a 1.5 T system and 128 MHz for a 3 T system. For the in vitro study, the devices were placed inside the ASTM phantom, which was symmetrically loaded in the center of the RF coil [9]. In this study, the coils at 1.5 T and 3 T were high pass RF transmit body coils constructed with eight parallel rungs, which is a tradeoff between accuracy and complexity. The radius of the coil was 315 mm, and the length of the coil was 650 mm. The standard ASTM phantom used in the study was an Acrylic container with a dielectric constant of 3.7 and an electrical conductivity of 0 S/m. The gelled-saline with a dielectric constant of 80.4 and an electrical conductivity of 0.47 S/m was used to fill the Acrylic container. The simulation boundaries enclosed the coil and phantom were all set to be absorbing boundary conditions (ABC) and the modes were chosen to be uniaxial perfectly matched layers (UPML) which can absorb incoming waves without reflection. The simulation time for each modeling was set to be 25 periods for the RF signals. After the simulations were finished, the currents, voltages, and E/H field signals were examined to guarantee the convergence of all the simulations. This modeling has been validated by comparing the strength of the electric field and temperature rises of a reference device at multiple locations inside the phantom from simulations and measurements.

The wire closures are usually made of metallic materials and were set to be PEC (perfect electric conductor) in the simulations. The devices were placed in the

ASTM phantom at the middle in the y and z direction and 2 cm away from the longest side wall as shown in Figure 1-1, according to the ASTM standard [9]. Adaptive meshing was adopted. The maximum mesh size for the sternal closures was set at 0.5 mm while the maximum mesh sizes of phantom were set at 5 mm for the gelled-saline and 10 mm for the shell. Baselines (enforced meshing reference) were generated on the bounding box of the wire to guarantee the correct distances between the two wires. And all the voxelized models were checked to avoid the meshing errors. Once simulations were finished, all the results were normalized to a whole-body averaged specific absorption rate (SAR) of 2 W/kg. As the simulation results in vitro, the peak SAR_{1g} near the studied worst-case device and the SAR_{1g} distribution around the device is shown in Figure 1-2.

The worst-case heating device at 1.5 T and 3 T determined from the in vitro simulations were placed inside the two human body models with corresponding sizes as in Figure 1-3 to assess the clinically relevant RF-induced heating [14] [15]. The sizes of the device were set as the sizes fitting to the FATS model and the girl model because they are the largest and smallest human models in the Virtual Family respectively. And the in vitro simulations shows that the worst-case device at 1.5 T fits the girl model while the worst-case device at 3 T fits the FATS model. The RF coils for 1.5 T and 3 T used in the in vivo simulations were the same as those used in the in vitro simulations. The human models were placed in three different loading positions in the RF coil as shown in Figure 1-4 (a) to present the different imaging regions. These loading positions would have the closures loaded at the bottom, the center, and the top of the coil. The simulation time was also set to be 25 periods of the RF signals. The wire-based sternal closures were placed in the clinical relevant locations in the human models as shown in Figure 1-4 (b) and (c). Similarly, the mesh sizes for the human body at 1.5 T and 3 T were set at 2 mm and the maximum mesh sizes for the sternal closures were set at 0.5 mm at 1.5 T and 1 mm at 3 T, respectively. All the results were normalized to a whole-body averaged SAR of 2 W/kg.

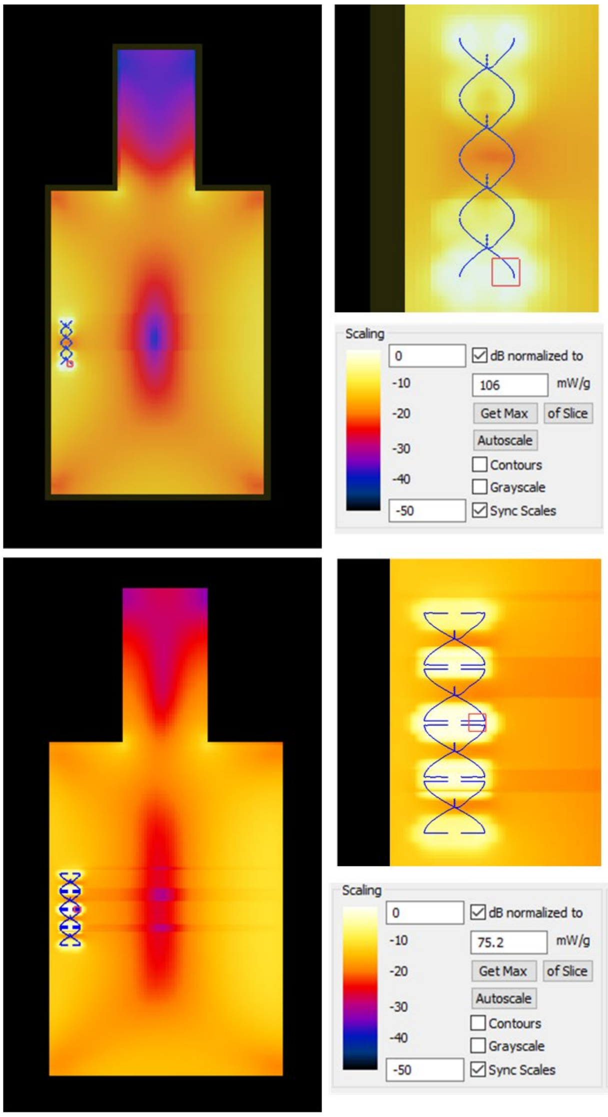

Figure 1-2. The peak SAR_{1g} near the studied worst-case device and the SAR_{1g} distributions around the device. Top:1.5 T with peak SAR_{1g} near the device as 106 W/kg; Bottom:3 T with peak SAR_{1g} near the device as 75.2 W/kg.

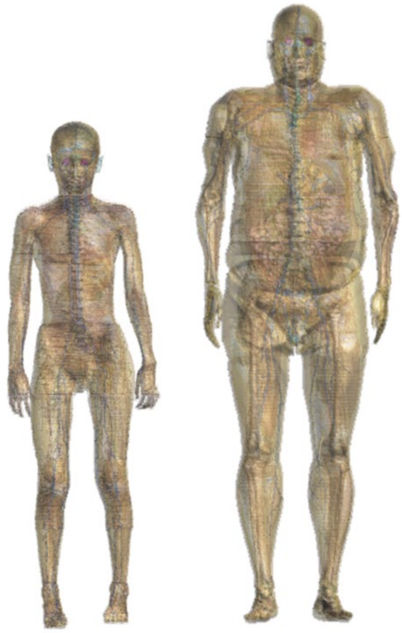

Figure 1-3. The two human models for simulation: Left: the girl model; Right: the FATS model.

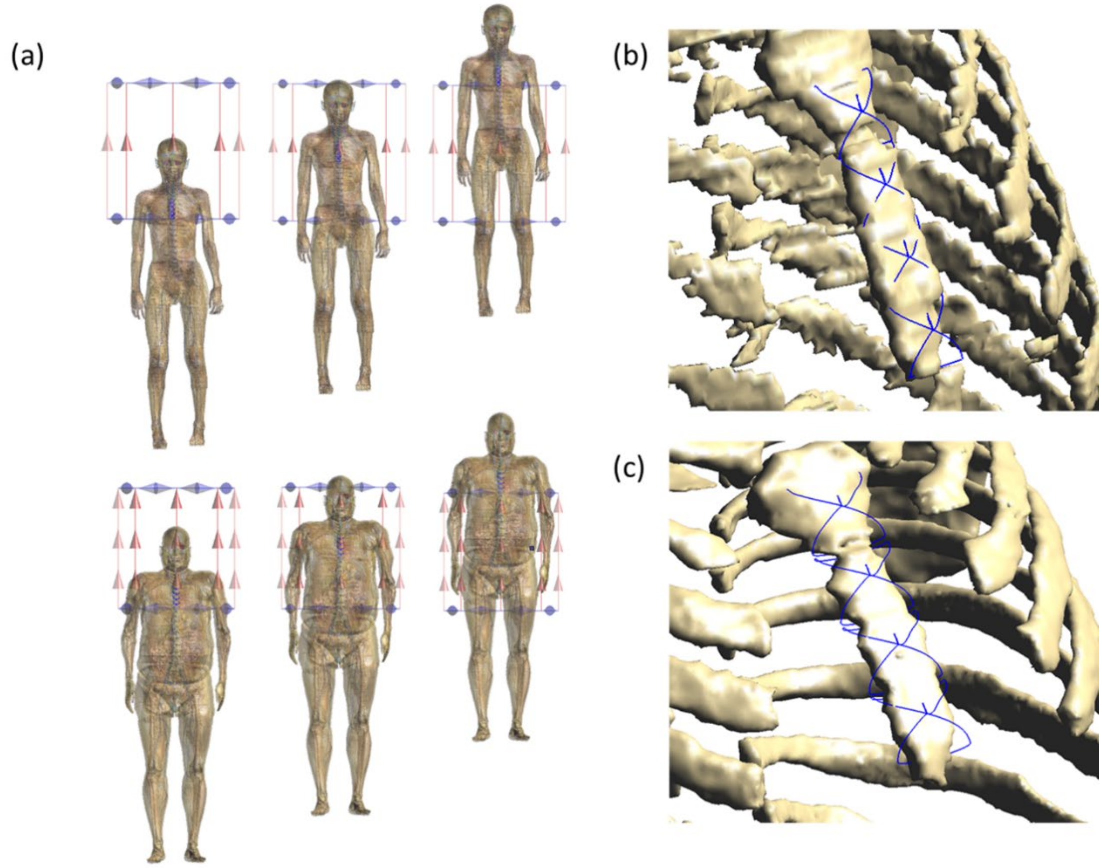

Figure 1-4. (a) The positions of the human model in coil at 1.5 T (top) and at 3 T (bottom), the implants were put at the bottom, center, and top of the coil from left to right. (b) The wire closures in the human model at 1.5 T. (c) The wire closures in the human model at 3 T.

The results of the electromagnetic simulations in human models are shown in Table 1-I.

From this study, for the same device, the simulation results in ASTM phantom and human models are quite different.

Table 1-I. The simulated results in human models.

	Whole body SAR (W/kg)	Overall peak SAR_{1g} (W/kg)	Peak SAR_{1g} near devices (W/kg)
Device in the bottom of coil at 1.5T	2	74.2	29.9
Device in the center of coil at 1.5T	2	139.2	32.1
Device in the top of coil at 1.5T	2	94.3	7.3
Device in the bottom of coil at 3T	2	84.9	29.2
Device in the center of coil at 3T	2	62.1	62.1
Device in the top of coil at 3T	2	49.0	2.3

In general, the in vitro study in the ASTM phantom is simple and convenient for both simulation and experiment. But the results from the ASTM phantom are not accurate. The human models from the Virtual family have relatively accurate details of the human tissues. They consider the geometrical shape of the realistic human body, the non-homogeneity of the human tissues, and their parameters. Thus, the in vivo simulation with these human models gives a more accurate evaluation of the RF-induced heating. However, study with the human models requires higher computational resources and these human models are difficult to fully fabricate and apply into experiments.

Thus, simplified human models need to be proposed to bridge the gaps between the in vitro and in vivo study.

In this study, the simplified human models will keep the shape of the original human models but reduce the types of the tissues by grouping similar tissues together. The human tissues are clustered, and the types of the tissues are reduced. The simplified human models are named as Tissue-reduced Virtual Family Models. Previous studies have proposed some simplified human models with 4, 8, or more types of tissues [21]–[23]. They are still complicated for the experiment to fabricate the models. And research about the simplified human models for evaluating RF-induced heating near the medical implants is still needed.

Chapter 2. DEVELOPMENT OF THE TISSUE-REDUCED VIRTUAL FAMILY MODELS AT 1.5 T

2.1. Method

2.1.1. Original human models from Virtual Family

This study focuses on the three representative human models from the virtual family (the Duke, Ella, and FATS models). According to the electrical conductivity and relative permittivity, the tissues in the original human models can be assorted as 34 types for the Duke and FATS models as in Figure 2-1 A and 36 types for Ella model as in Figure 2-1 B.

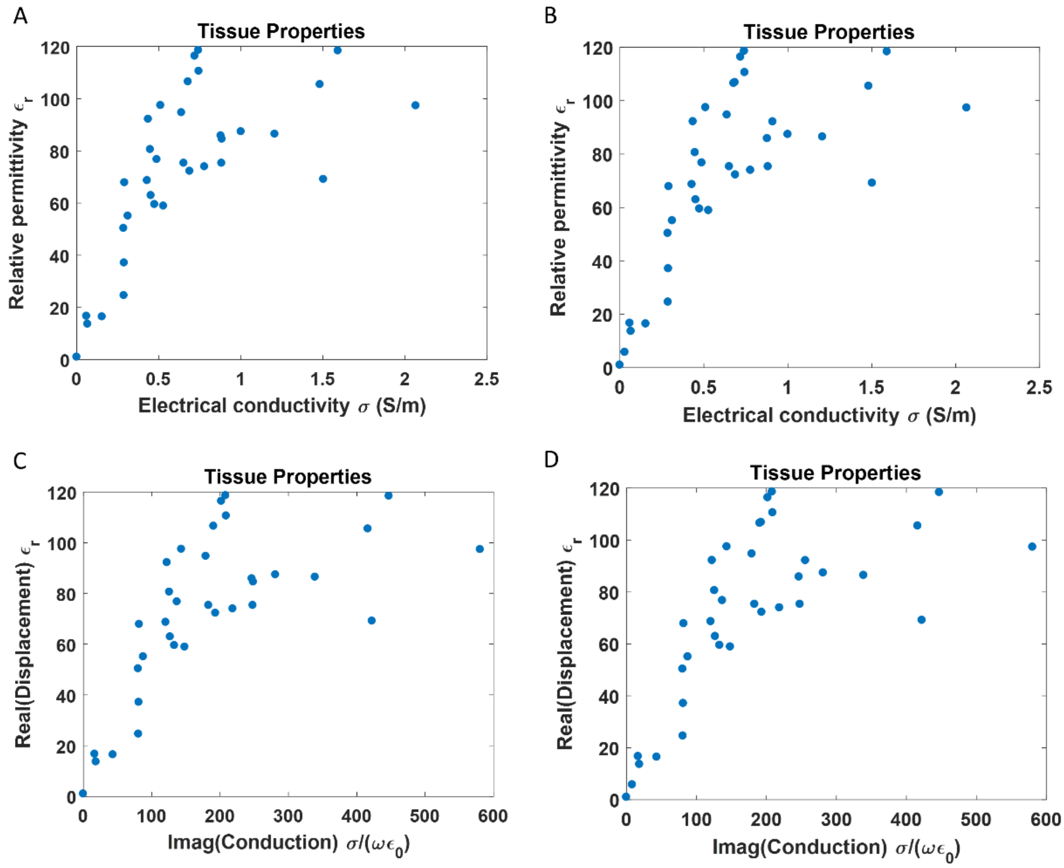

Figure 2-1. Scatter plots for the tissue properties at 1.5 T.

Instead of directly fitting the electrical conductivity and relative permittivity, the real and imaginary parts of the relative effective permittivity were chosen for fitting. From the Ampere's law, the curl of the magnetic field is equal to the sum of the source current density, the conduction current density, and the displacement current density as

$$\nabla \times \vec{H} = \vec{J} + j\omega\varepsilon\vec{E} = \vec{J_i} + \vec{J_c} + j\omega\varepsilon\vec{E}. \tag{2-1}$$

Combining the conduction and displacement parts and taking the ε_0 out, we will get the relative effective permittivity $\left(\varepsilon_r - j\frac{\sigma}{\omega\varepsilon_0}\right)$ as

$$\nabla \times \vec{H} = \vec{J_i} + j\omega\varepsilon_0\left(\varepsilon_r - j\frac{\sigma}{\omega\varepsilon_0}\right)\vec{E}. \tag{2-2}$$

Obviously, the electric field and magnetic field are related to each other via the relative effective permittivity. Thus, we will fit the real and imaginary parts of the relative effective permittivity. The scatter plots of the tissues' properties based on the relative effective permittivity are shown in Figure 2-1 C and Figure 2-1 D.

The volume percentages or the volume weights are different for different tissues in a certain human model or a certain tissue across different human models. The detailed volume weights for the tissues of the three human models are shown in Figure 2-2. For example, the fat tissue's volume weight in the FATS model is obviously higher than those in the Duke and Ella models. The volume weight of tissues may be considered for simplifying the human models.

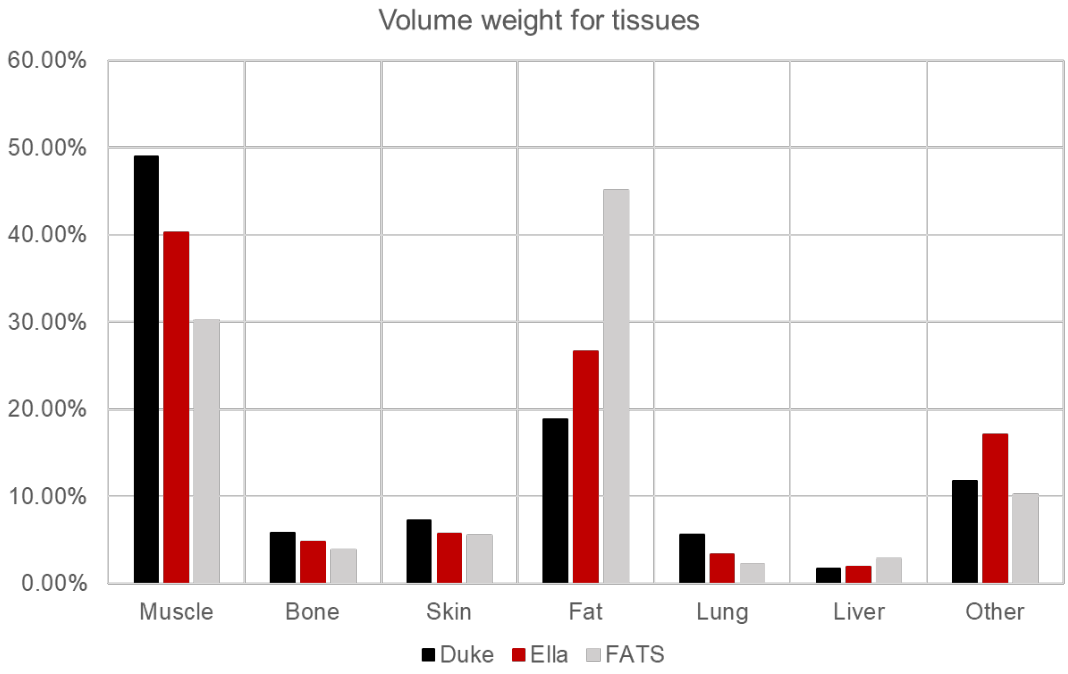

Figure 2-2. Volume weight for tissues.

2.1.2. Gaussian mixture model and three tissue cluster methods

For the previous study, the human tissues were naturally grouped according to the electrical conductivity and relative permittivity [22] or grouped based on the k-means clustering method [23]. The k-means clustering method tends to group the points with the closest distance to each other to form a cluster and is more suitable for the data points with circular form [24], [25]. As shown in Figure 2-1, the data points of the tissues' properties are not circular form. So instead of using the model based on the distance like the k-means method, the Gaussian mixture model (GMM) based on the Gaussian distribution for clustering was tried in this study. A Gaussian distribution is also called a normal distribution and can be multivariate depending on the dimensions of the data. In this study, the data of the real and imaginary parts of the relative effective permittivity is 2-dimensions. Thus, every Gaussian distribution in the GMM for this study is 2-variate and has a mean vector and a covariance matrix. Every Gaussian distribution in the GMM has its weight, and the weighted sum of the probability densities of these Gaussian distributions is a GMM [26]. The GMM assumes a certain number of Gaussian distributions, and each distribution represents a cluster. The covariance matrixes of these Gaussian distributions can be full or diagonal. The diagonal matrix means that except for the elements of the main diagonal, the other elements are 0 in this matrix. And for these Gaussian distributions in a GMM, they can have the same or different covariance matrixes. Clustering by GMM tries to put the data points belonging to the same Gaussian distribution in one cluster [24], [26]. To get the simplified human models, the data points should first be fitted with GMM to get the clusters. Then the electrical parameters need to be calculated for every cluster. According to whether considering the volume weight of every tissue during the two processes, there are three tissue cluster methods as in Table 2-I.

Table 2-I. Three tissue cluster methods.

Whether consider the volume weight	Fitting data matrix	Calculating the electrical parameters for every cluster
Cluster method 1	No	No
Cluster method 2	No	Yes
Cluster method 3	Yes	Yes

There are some detailed settings for the GMM, such as the number of clusters, the type of covariance matrix (full or diagonal) and the shared or unshared covariance matrix (whether all the covariance matrix for every Gaussian distribution in GMM is identical). To find the suitable settings, the Akaike's Information Criterion (AIC) and the Bayesian Information Criterion (BIC) were used [27]–[29]. The AIC and BIC are closely related to the likelihood, which is a measure of model fit. A higher likelihood means a better fit. But if we only concentrate on finding the maximum likelihood, we would get a model with one data point solely in one cluster [29]. That will not simplify the human models. Thus, the criteria which do not only depend on the likelihood are adopted such as the AIC and BIC. The AIC is defined as

$$\mathrm{AIC} = 2K - 2\ln\,(likelihood), \tag{2-3}$$

where K is the number of the parameters [29]. The BIC is defined as

$$\mathrm{BIC} = K\ln(N) - 2\ln\,(likelihood), \tag{2-4}$$

where K is the number of the parameters and N is the sample size of the data [29]. Thus, the lower AIC and BIC mean a better fit for the data. An example of AIC and BIC for the Duke model using cluster method 3 is shown in Figure 2-3.

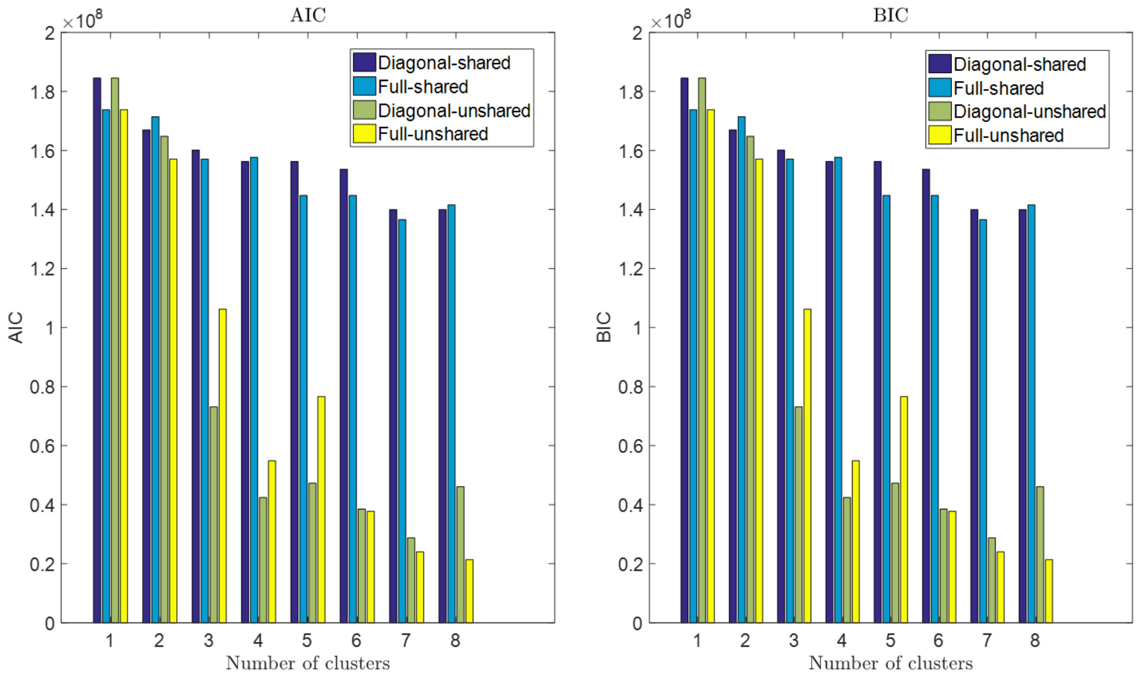

Figure 2-3. AIC and BIC.

As in this example, the full covariance matrix should be chosen for a number of clusters as two, and not all covariance matrices are identical (unshared). For cluster number, the eight clusters have the smallest AIC and BIC. In this study, to make the experiment in the human models more practical, the number of clusters as 1, 2 and 3 was focused on. And to get a reference, the number of eight was also considered for electromagnetic simulations.

For 1, 2, 3, and 8 clusters, the scatter plots for the three cluster methods and three human models are shown in Figure 2-4 to Figure 2-6.

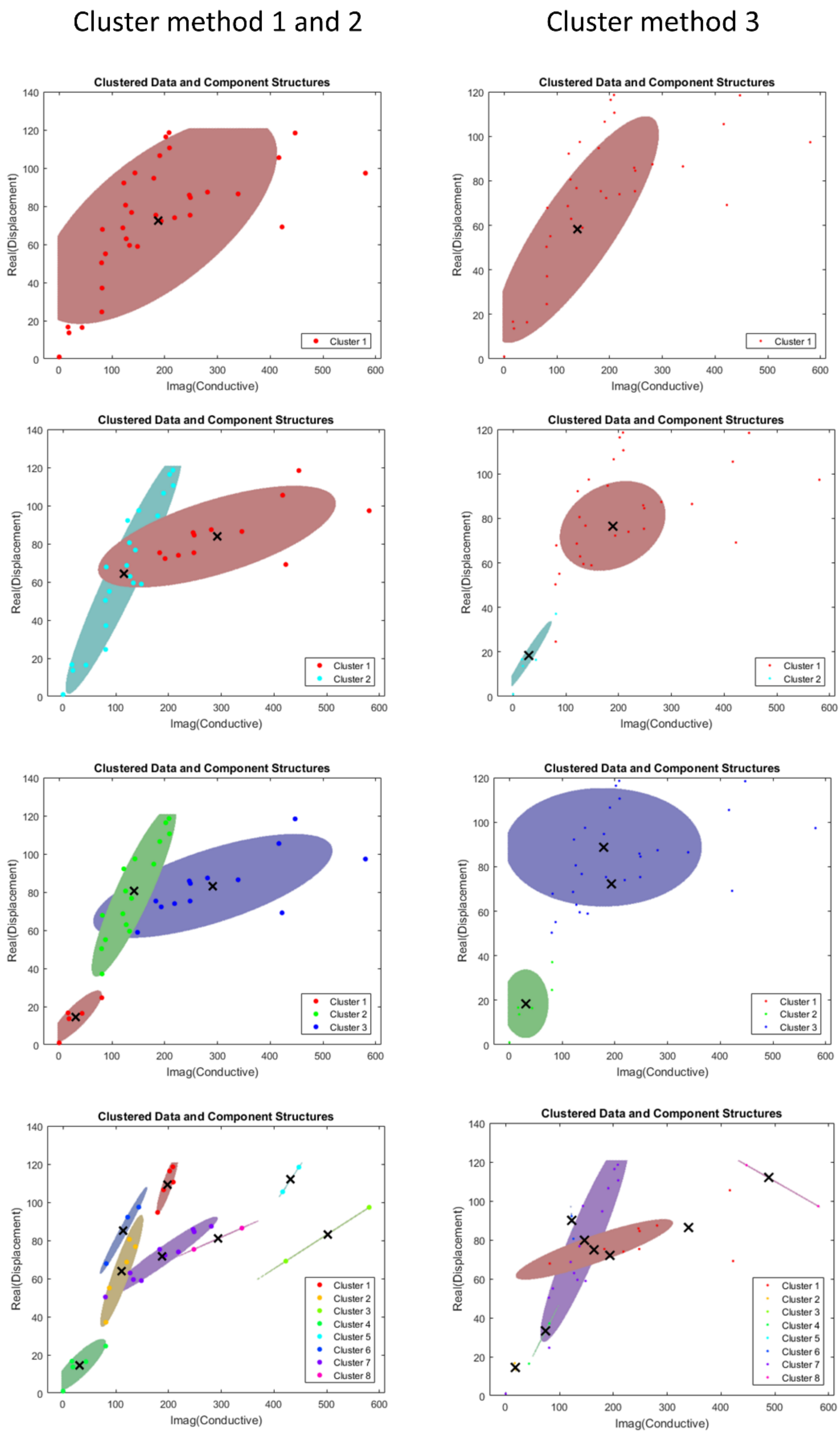

Figure 2-4. The scatter plots for the three cluster methods for the Duke model.

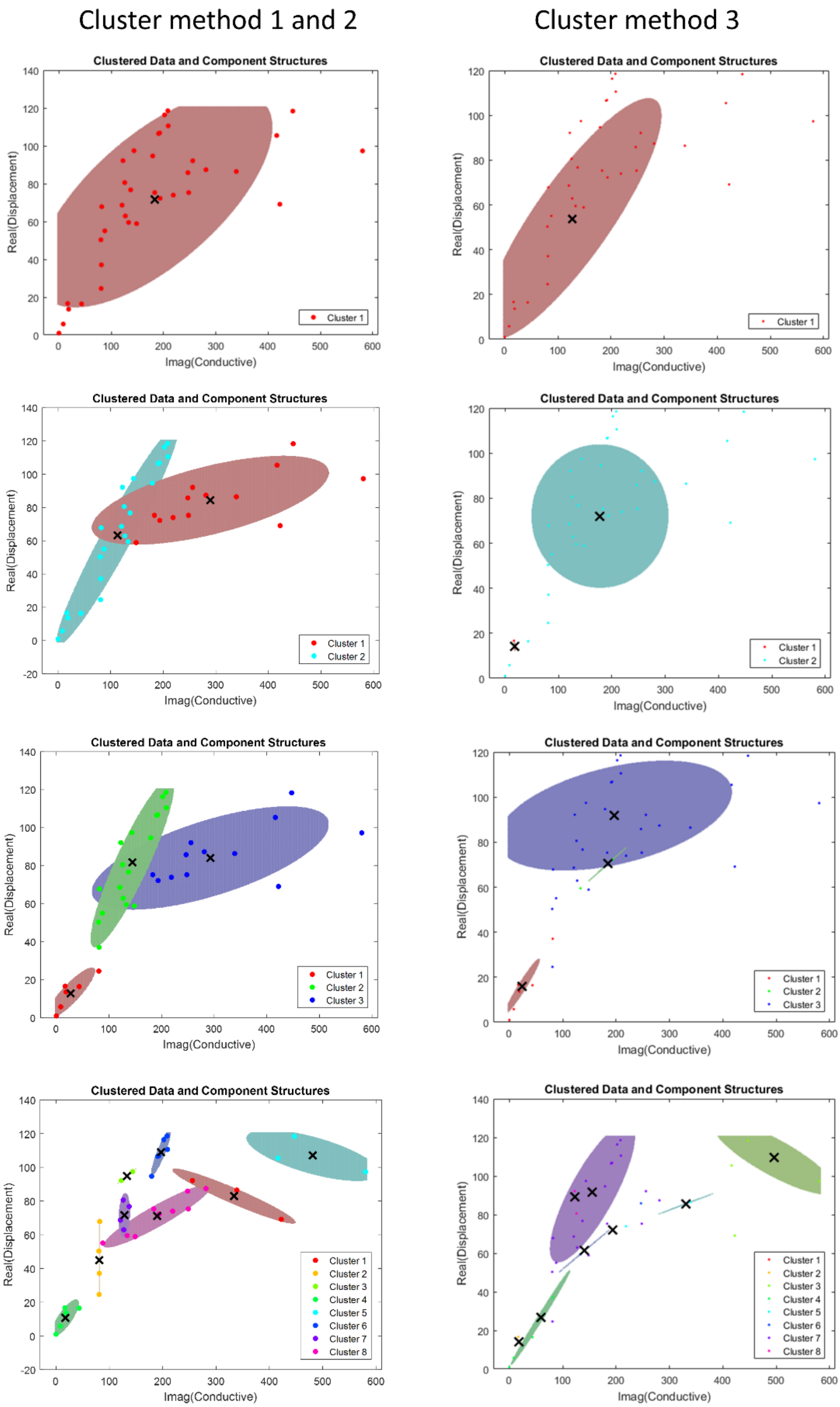

Figure 2-5. The scatter plots for the three cluster methods for the Ella model.

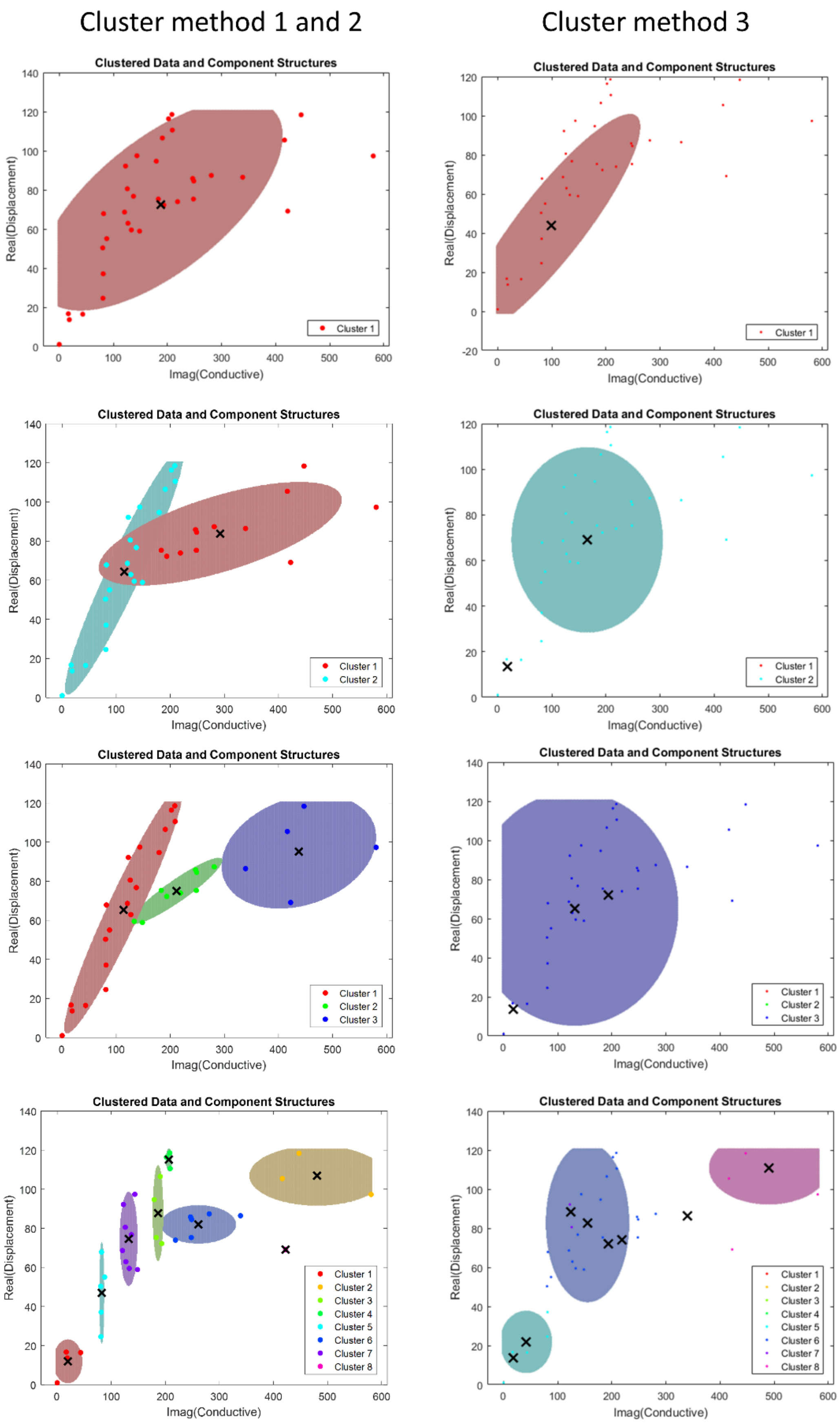

Figure 2-6. The scatter plots for the three cluster methods for the FATS model.

2.1.3. **Electromagnetic simulation setup**

The electromagnetic simulations were conducted for the three original human models (Duke, Ella, and FATS) and the simplified tissue-reduced human models for them with three cluster methods and 1, 2, 3 and 8 clusters. The SEMCAD X (V14.8 SPEAG) software was used for simulations based on the Finite-Difference Time-Domain (FDTD) method. The three representative human models were loaded under three landmark positions as shown in Figure 2-7 based on the position of the thalamus. At 1.5 T, the frequency is 64 MHz. The boundary conditions for six directions were set to be absorbing boundary conditions (ABC), which can absorb incoming waves without reflection. The simulation time was all set to be 30 periods. After the simulations were finished, the currents, voltages, and electrical/magnetic field signals were examined to guarantee the convergence of all the simulations. Adaptive meshing was adopted and the maximum mesh size for the human models is 2 mm. The results were all normalized to a whole-body SAR value of 2 W/kg. The head SAR and partial body SAR were checked to ensure that they do not exceed the limits under NORMAL OPERATING MODE according to the standard IEC 60601-2-33 [30].

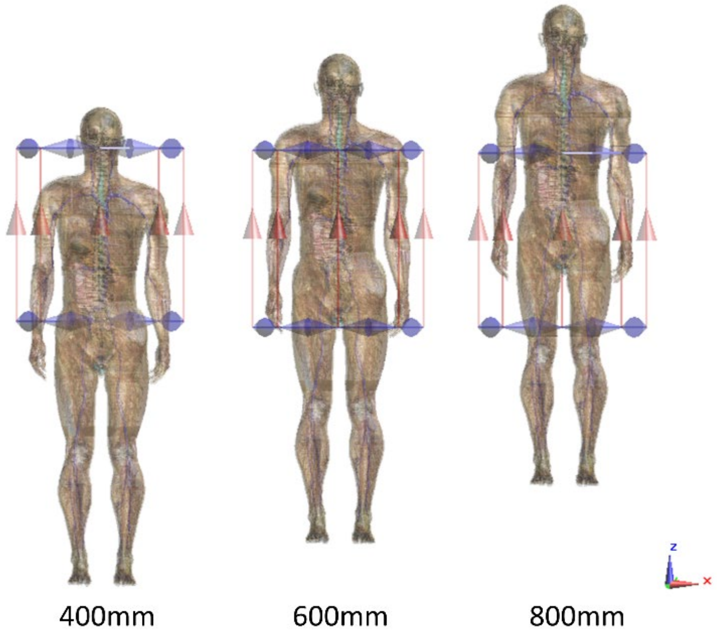

Figure 2-7. Three landmark positions.

2.2. Results and discussion: a correlation analysis

Based on the results of electromagnetic simulations, the electric field in several different body regions was extracted for both the simplified and original models. These body regions are shown in the Figure 2-8.

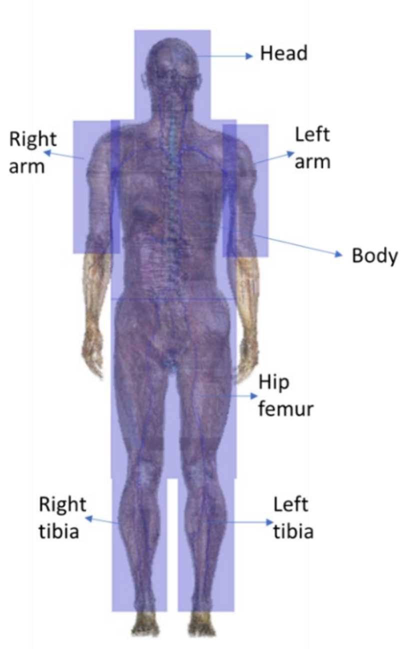

Figure 2-8. The body regions for electric field extraction.

To evaluate the performance of the tissue-reduced human models, a correlation analysis between the electric field of the original and simplified human models was conducted. The correlation coefficients of the electric field in the original and simplified human models were calculated for the analysis. The formula for calculating the correlation coefficient of variable A and variable B is [31]

$$\rho(A, B) = \frac{\text{cov}(A,B)}{\sigma_A \sigma_B}, \tag{2-5}$$

where the σ_A and σ_B are the standard deviations of the variable A and B, respectively, and cov(A,B) is the covariance of A and B. The cov(A,B) is calculated by [32]

$$\text{cov}(A, B) = \text{E}[(A - \mu_A)(B - \mu_B)], \tag{2-6}$$

where μ_A and μ_B are the means of variables A and B, respectively and E[] is the expected value (mean) of the variable inside the brackets. In this study, the variables A and B are the electric field in the original and simplified human models. The results of the correlation analysis for the Duke model in terms of the module of electric field are shown in Figure 2-9. Generally, cluster number as 1 has a poor correlation for all the three cluster methods as shown by the solid red line. For the cluster method 3, the number of clusters as 2 indicated by the solid black line already has a good correlation. In detail, the correlation coefficients for the cluster method 3 with 2 clusters are higher than 0.95 for all studied conditions.

The same correlation analysis was conducted for both the Ella and FATS models. And the same conclusion was obtained like the Duke model, that is, the cluster method 3 with 2 clusters has a good correlation and has only 2 clusters. The results of the correlation coefficients for the cluster method 3 with 2 clusters in terms of the module of electric field are shown in Figure 2-10 A and B. For all studied conditions, the correlation coefficients are higher than 0.96 for the Ella model and are higher than 0.85 for the FATS model. Thus, for the three human models, to get a balance between better correlation and fewer clusters, the cluster method 3 with 2 clusters is chosen.

For the FATS model, because the fat tissue has a volume weight as high as 45.07%, the GMM will put the fat tissue in an independent cluster. But considering that the fat and the bone have similar electrical parameters, an adjustment was conducted to the clusters and the bone was moved into the same cluster as the fat. Electromagnetic simulations were also performed for the adjusted simplified FATS model, and the correlation coefficients are shown as in Figure 2-10 C. For the adjusted FATS model, the modules of the correlation coefficients are higher than 0.92. It has an overall better electric field correlation with the original FATS model than that of the simplified FATS model with only fat in a cluster.

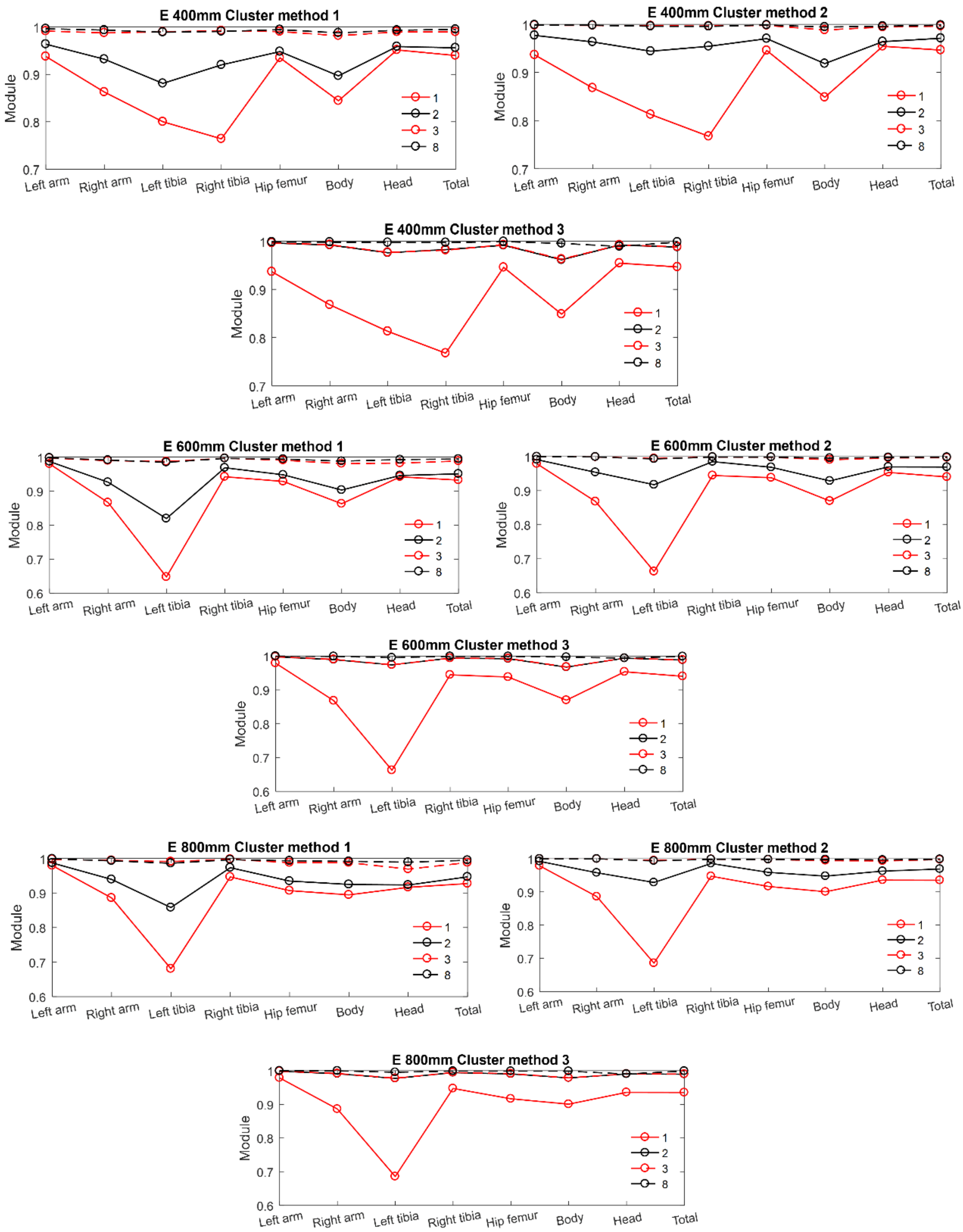

Figure 2-9. The correlation coefficients for the Duke model in terms of the module of electric field.

For more details of the correlation analysis, the correlation coefficients for the electric field along the x, y and z directions were also calculated. The results for those of the chosen cluster method with 2 clusters are attached in Table 2-II, Table

2-III and Table 2-IV. More results for the correlation analysis of electric field are attached in the Appendix I.

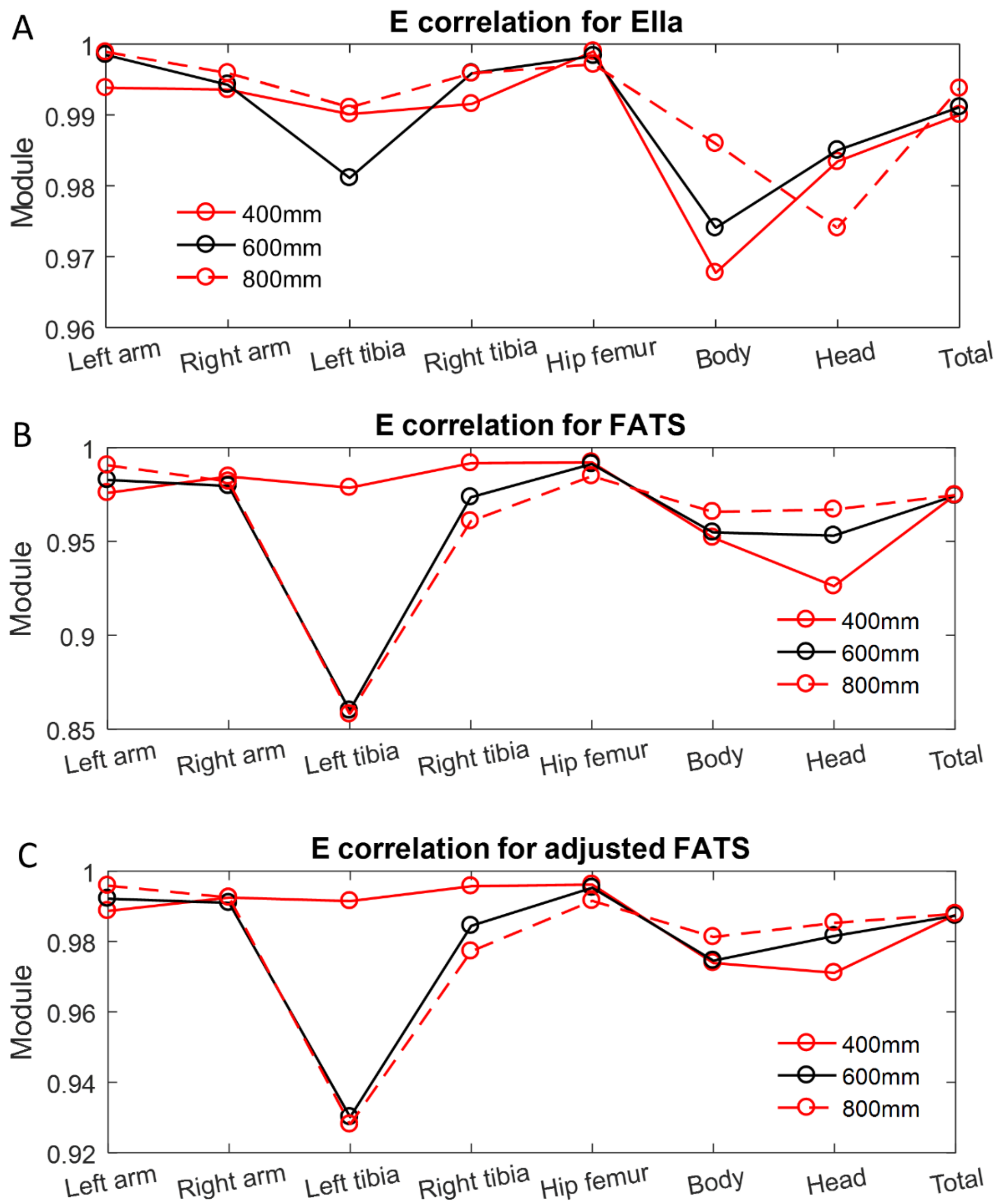

Figure 2-10. The correlation coefficients for the Ella and FATS models.

Table 2-II. The correlation coefficients between the original Duke model and the chosen tissue-reduced Duke model at 1.5 T.

Landmark positions	400mm		600mm		800mm	
Correlation coefficient	module	phase	module	phase	module	phase
R of Ex_left_arm	1.00	-0.02	1.00	0.00	1.00	0.01
R of Ey_left_arm	0.99	0.00	1.00	0.00	1.00	0.00
R of Ez_left_arm	1.00	-0.01	1.00	0.00	1.00	0.00
R of E_left_arm	1.00	0.00	1.00	0.00	1.00	0.00
R of Ex_right_arm	1.00	-0.01	0.99	0.03	0.99	0.04
R of Ey_right_arm	0.99	0.01	0.99	0.02	0.99	0.01
R of Ez_right_arm	0.99	0.01	0.99	0.01	0.99	0.01
R of E_right_arm	0.99	0.00	0.99	0.00	0.99	0.00
R of Ex_left_tibia	0.99	-0.05	0.98	-0.02	0.99	0.00
R of Ey_left_tibia	0.98	-0.02	0.98	0.05	0.98	0.05
R of Ez_left_tibia	0.96	0.10	0.97	0.14	0.97	0.14
R of E_left_tibia	0.98	0.00	0.97	0.00	0.98	0.00
R of Ex_right_tibia	0.99	0.04	1.00	0.01	1.00	0.00
R of Ey_right_tibia	0.99	0.03	1.00	0.00	1.00	0.00
R of Ez_right_tibia	0.97	0.16	0.96	0.11	0.96	0.09
R of E_right_tibia	0.98	0.00	0.99	0.00	0.99	0.00
R of Ex_hip_femur	0.99	-0.02	0.99	-0.01	0.99	0.00
R of Ey_hip_femur	0.99	0.00	0.99	0.00	0.99	-0.01
R of Ez_hip_femur	0.99	-0.05	1.00	-0.04	1.00	-0.04
R of E_hip_femur	0.99	0.00	0.99	0.00	0.99	0.00
R of Ex_body	0.98	0.01	0.97	0.04	0.97	0.04
R of Ey_body	0.97	0.01	0.97	0.01	0.97	0.01
R of Ez_body	0.99	0.00	0.99	-0.01	0.99	-0.02
R of E_body	0.96	0.00	0.97	0.00	0.98	0.00
R of Ex_head	0.99	0.00	0.99	-0.01	0.99	-0.02
R of Ey_head	0.99	0.00	0.99	0.00	0.98	0.00
R of Ez_head	0.99	-0.02	0.99	-0.01	0.98	-0.03
R of E_head	0.99	0.00	0.99	0.00	0.99	0.00
R of Ex_total	0.99	0.00	0.98	0.00	0.99	0.00
R of Ey_total	0.98	0.00	0.99	0.00	0.99	0.00
R of Ez_total	0.99	0.00	0.99	-0.01	0.99	-0.02
R of E_total	0.99	0.00	0.99	0.00	0.99	0.00

Table 2-III. The correlation coefficients between the original Ella model and the chosen tissue-reduced Ella model at 1.5 T.

Landmark positions	400mm		600mm		800mm	
Correlation coefficient	module	phase	module	phase	module	phase
R of Ex_left_arm	0.99	-0.02	1.00	-0.01	1.00	0.00
R of Ey_left_arm	0.99	-0.02	1.00	0.00	1.00	0.00
R of Ez_left_arm	0.99	-0.03	0.99	-0.02	0.99	-0.01
R of E_left_arm	0.99	0.00	1.00	0.00	1.00	0.00
R of Ex_right_arm	1.00	0.05	0.99	0.00	1.00	0.00
R of Ey_right_arm	0.99	0.01	1.00	0.01	1.00	0.01
R of Ez_right_arm	0.99	-0.01	0.99	0.00	0.99	0.00
R of E_right_arm	0.99	0.00	0.99	0.00	1.00	0.00
R of Ex_left_tibia	0.99	-0.01	0.99	0.01	0.99	0.00
R of Ey_left_tibia	0.99	0.04	0.99	0.05	0.99	0.02
R of Ez_left_tibia	0.98	0.08	0.97	0.07	0.98	0.04
R of E_left_tibia	0.99	0.00	0.98	0.00	0.99	0.00
R of Ex_right_tibia	1.00	-0.01	1.00	0.00	1.00	0.00
R of Ey_right_tibia	0.99	-0.01	1.00	0.00	1.00	0.00
R of Ez_right_tibia	0.97	0.04	0.97	0.01	0.97	0.01
R of E_right_tibia	0.99	0.00	1.00	0.00	1.00	0.00
R of Ex_hip_femur	1.00	0.00	1.00	0.00	1.00	-0.01
R of Ey_hip_femur	1.00	0.00	1.00	0.00	0.99	0.00
R of Ez_hip_femur	1.00	0.01	1.00	0.00	1.00	0.00
R of E_hip_femur	1.00	0.00	1.00	0.00	1.00	0.00
R of Ex_body	0.98	-0.03	0.97	-0.03	0.98	-0.02
R of Ey_body	0.96	-0.03	0.96	-0.01	0.97	0.00
R of Ez_body	0.99	-0.03	0.99	-0.01	0.99	0.01
R of E_body	0.97	0.00	0.97	0.00	0.99	0.00
R of Ex_head	0.98	-0.02	0.98	-0.04	0.98	-0.02
R of Ey_head	0.98	-0.01	0.97	-0.01	0.95	-0.01
R of Ez_head	0.98	-0.02	0.98	-0.04	0.95	-0.02
R of E_head	0.98	0.00	0.99	0.00	0.97	0.00
R of Ex_total	0.99	-0.01	0.99	-0.01	0.99	-0.01
R of Ey_total	0.98	-0.01	0.98	0.00	0.99	0.00
R of Ez_total	0.99	-0.03	0.99	-0.01	1.00	0.00
R of E_total	0.99	0.00	0.99	0.00	0.99	0.00

Table 2-IV. The correlation coefficients between the original FATS model and the chosen tissue-reduced FATS model at 1.5 T.

Landmark positions	400mm		600mm		800mm	
Correlation coefficient	module	phase	module	phase	module	phase
R of Ex_left_arm	0.99	-0.01	0.99	-0.01	1.00	-0.01
R of Ey_left_arm	0.98	-0.02	0.99	-0.01	0.99	0.00
R of Ez_left_arm	0.99	-0.01	0.99	-0.01	0.99	-0.02
R of E_left_arm	0.99	0.00	0.99	0.00	1.00	0.00
R of Ex_right_arm	0.99	0.02	0.99	0.01	0.99	-0.01
R of Ey_right_arm	0.99	-0.01	0.99	0.00	0.99	0.00
R of Ez_right_arm	0.99	-0.02	0.99	-0.02	0.99	-0.03
R of E_right_arm	0.99	0.00	0.99	0.00	0.99	0.00
R of Ex_left_tibia	0.99	0.00	0.96	0.05	0.96	0.05
R of Ey_left_tibia	0.99	0.01	0.95	0.07	0.95	0.07
R of Ez_left_tibia	0.96	0.07	0.92	0.08	0.92	0.06
R of E_left_tibia	0.99	0.00	0.93	0.00	0.93	0.00
R of Ex_right_tibia	1.00	-0.01	0.99	-0.01	0.99	0.00
R of Ey_right_tibia	0.99	-0.01	0.99	0.00	0.99	0.01
R of Ez_right_tibia	0.98	0.01	0.93	0.04	0.93	0.04
R of E_right_tibia	1.00	0.00	0.98	0.00	0.98	0.00
R of Ex_hip_femur	1.00	-0.03	1.00	-0.02	0.99	-0.01
R of Ey_hip_femur	0.99	-0.01	0.99	-0.01	0.98	-0.01
R of Ez_hip_femur	0.99	-0.02	1.00	-0.01	1.00	-0.01
R of E_hip_femur	1.00	0.00	1.00	0.00	0.99	0.00
R of Ex_body	0.98	-0.02	0.98	-0.02	0.98	-0.02
R of Ey_body	0.97	-0.02	0.97	-0.02	0.97	-0.01
R of Ez_body	0.99	-0.01	0.99	-0.01	0.99	-0.02
R of E_body	0.97	0.00	0.97	0.00	0.98	0.00
R of Ex_head	0.97	-0.01	0.97	-0.02	0.98	-0.01
R of Ey_head	0.97	0.00	0.98	0.00	0.98	0.00
R of Ez_head	0.98	-0.01	0.99	-0.01	0.98	0.01
R of E_head	0.97	0.00	0.98	0.00	0.99	0.00
R of Ex_total	0.99	-0.02	0.99	-0.02	0.99	-0.02
R of Ey_total	0.98	-0.01	0.98	-0.01	0.98	0.00
R of Ez_total	0.99	-0.01	0.99	-0.01	0.99	-0.01
R of E_total	0.99	0.00	0.99	0.00	0.99	0.00

2.3. **Conclusions**

Based on the electric field correlation analysis, the chosen tissue-reduced virtual family models mainly use the cluster method 3 with 2 clusters, so we named them as Volume-Weighing Tissue-Cluster models with 2 clusters (VWCk2). The details of the electrical conductivities and relative permittivities are as in Table 2-V. For cluster 1, the main tissues are the bone and fat with smaller values of electrical conductivity and relative permittivity. For cluster 2, the main tissues are the muscle and skin with larger values of electrical conductivity and relative permittivity. The detailed tissues in the two clusters are attached in the Appendix II.

Table 2-V. Detailed parameters for the chosen tissue-reduced virtual family models at 1.5 T.

	Cluster 1		Cluster 2	
	Bone, fat, …		Muscle, skin, …	
	ε_r	σ (S/m)	ε_r	σ (S/m)
Duke	18.38	0.11	76.58	0.67
Ella	14.11	0.07	72.03	0.63
FATS	13.88	0.07	72.97	0.63

Chapter 3. Tissue-reduced Virtual Family Models' application on RF-induced heating evaluation of passive medical implants at 1.5 T

3.1. Introduction

There are some common safety concerns for the MRI examination. One of which is the RF-induced heating coming from the interaction between the medical implanted device and the electromagnetic field [33]. The heating can be quite high if the device is made of metallic materials. Related research about the RF-induced heating of the implanted device has been conducted about the passive devices, such as the stent system [4], [34], the wire-based sternal closure [13], and the active devices such as the DBS [35], the pacemaker [36]. These studies reveal that the RF-induced heating could lead to a quite high temperature rise near the device and burn the human tissue. To assure the safety of the patients undertaking the MRI examination, the RF-induced heating should be properly evaluated, and the medical device needs to be labeled per the ASTM standard [1], [9].

To evaluate the RF-induced heating for medical implants, the ASTM phantom is often used for both simulation and experiment to yield a fast prediction of the RF-induced heating [9]. Several previous research was conducted in the ASTM phantom for RF-induced heating evaluation with simulation [10], [11] and experiments [12]. But if the more accurate results of the RF-induced heating are needed, the high-resolution anatomically realistic human models such as the virtual family human models [14], [15] should be used to take the human geometrical shape, properties of the human tissues into account. Research on the RF-induced heating in human models is conducted mainly with numerical simulations [16], [17]. Although some experiments in human models were conducted but the fabricated human models are greatly simplified to only keep the human shape and part of the body [18], [19]. The virtual family human models have relatively accurate details of the human tissues, but they require high computational resources and are difficult to be fully fabricated and applied to experiments. Thus, the human models need to be simplified to make the fabrication more feasible for experiments but should still be able to evaluate the RF-induced heating relatively accurately, that is, more accurate than that of the ASTM phantom at least. There are some previous studies about the simplified human models for MRI safety study and SAR investigation [21]–[23]. However, the study about simplified human models' application on RF-induced heating evaluation of medical device is still necessary. In our previous study, the Volume-Weighing Tissue-Cluster Models with 2 clusters (VWCk2) based on the Gaussian mixture method were proposed for evaluating the RF-induced heating of some active devices (AIMDs) [37]. The correlation coefficients between the incident electric field inside the original human models and the simplified human models are higher than 0.96 for the studied three human models (the Duke model, Ella model, and FATS model). The correlation coefficients of RF-induced heating are higher than 0.997 with absolute error less than 1 °C [37] for all studied AIMDs. Thus, the proposed VWCk2 models have a good performance on evaluating the RF-induced heating of the studied AIMDs and have only two types of tissues. It is relatively practical for the experimental study in the future. However, for the VWCk2 models, the performance on the RF-induced heating evaluation for passive device system is unknown and needs to be investigated.

The method to evaluate the RF-induced heating of passive device is quite different from that of the active device. For passive device, the spatial averaged specific absorption rate (SAR) is used to quantify the heating [38]. The incident electric field near the implanted device determines the input energy while the surrounding human tissues' properties especially the electrical conductivities will influence the power dissipation and distribution [39]. Both will influence the values of SAR near the device. Considering the high correlation of electric field between the original and simplified human models (the VWCk2 models), the VWCk2 models will have a quite similar distribution of the incident electric field. However, a scaling needs to be conducted to consider the influence of the surrounding tissues' electrical conductivities, which will be explained in detail in the Method part.

In this paper, four common representative passive device systems are investigated using simulations: the standalone screw system, the pedicle screw system, the plate and screw system and the stent system. Every type of passive device was implanted in the clinical positions of the original and simplified human models (the Duke, Ella and FATS models). And the human models were loaded in the 1.5 T G32 birdcage coil at three landmark positions. To make a comparison between the simplified human models and the ASTM phantom, the studied passive device was also placed into the ASTM phantom and a scaling using the incident tangential electric field was also conducted for the results of the ASTM phantom.

3.2. Method

3.2.1. Tissue-Reduced Virtual Family Models by tissue clustering method

The three representative human models from the virtual family are used as the original models for simplification. They are the Duke model (adult male), the Ella model (adult female) and the FATS model (adult fat male) [14], [15]. According to our previous study, the tissue clustering method based on the Gaussian Mixture Method (GMM) is a suitable method to determine the simplified human models for the electromagnetic simulations [37]. In this study, the GMM was implemented by the function of MATLAB to fit the Gaussian mixture distribution to the data of real part and imaginary part of the complex relative effective permittivity. The Akaike Information Criterion and Bayesian Information Criterion were used to find the most suitable GMM model. And the simplified human models (VWCk2 human models) considering the volume weighting of every type of tissue have a great performance on the electric field correlation and evaluation for the RF-induced heating of AIMDs [37]. The tissue-reduce virtual family models (the VWCk2 models) have only two types of human tissues so they simplify the simulation setup significantly and make the experimental study in human models more practically in the future. The detailed tissue clusters (the

Duke model is used as an example) and their relative permittivities (ε_r), electrical conductivities (σ) and mass densities (ρ) are shown in Figure 3-1. Figure 3-1 A shows the main tissues in the two clusters of the tissue-reduced Duke model in the SEMCAD software, Figure 3-1 B shows the scatter plot of the two clusters for the tissue-reduced Duke model, and Figure 3-1 C shows the detailed parameters of the tissue-reduced Duke, Ella, and FATS human models.

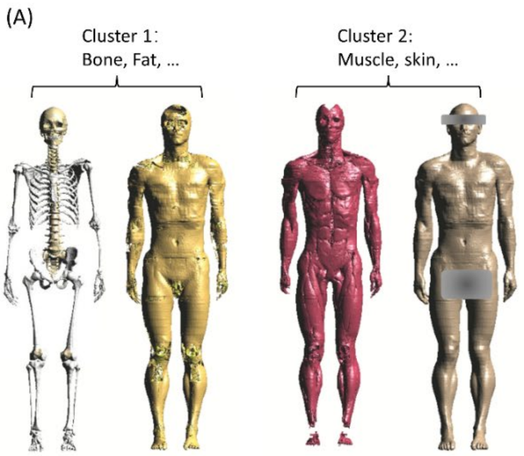

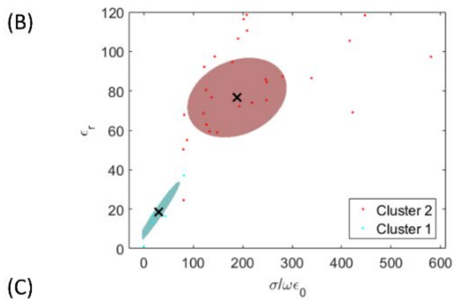

(C)

	Cluster 1			Cluster 2		
	Bone, fat, …			Muscle, skin, …		
	ε_r	σ (S/m)	ρ (kg/m³)	ε_r	σ (S/m)	ρ (kg/m³)
Duke	18.38	0.11	1000.6	76.58	0.67	1090.5
Ella	14.11	0.07	1064.6	72.03	0.63	1082.4
FATS	13.88	0.07	989.3	72.97	0.63	1062.0

Figure 3-1. A, The main tissues in the two clusters of the tissue-reduced Duke model in the SEMCAD software. B, The scatter plot of the two clusters for the tissue-reduced Duke model. C, The detailed parameters of the tissue-reduced virtual family human models.

3.2.2. **Passive device systems**

To investigate if the tissue-reduced virtual family models can accurately evaluate the RF-induced heating of the passive device, four types of common passive systems were studied: the standalone screw system, the pedicle screw system, the plate and screw system and the stent system. The standalone screw system is generally the simplest passive implanted system and is always used for the fixation of the bone to treat the fracture. The screws can be implanted in many regions inside the human body with different sizes [40]–[43]. In this study, the screws were placed around the ankle and the pelvic in the original and tissue-reduced human models as shown in the Figure 3-2 A. The pedicle screw system was implanted near the lower back and the neck in this study as shown in Figure 3-2 B. Another common passive device system is the plate and screw system used for fracture treatment. In this study, the plate and screw system was implanted near the fibula [44]–[46], the rib [47] and the cervical vertebrate C4 [48], [49] as shown in Figure 3-2 C. And the stent system is placed in the three positions of the human models: the iliac artery, the thoracic aorta, and the carotid artery [50], [51]. The detailed implanted positions of the stent system are shown in Figure 3-2 D. For all studied passive device systems, the device's models were simplified and implanted around the clinical positions inside the human models. The detailed sizes of the device are adaptative to different human models (the Duke, Ella, and FATS models). But for the same human models with original tissues or simplified tissues, the sizes of the device are identical.

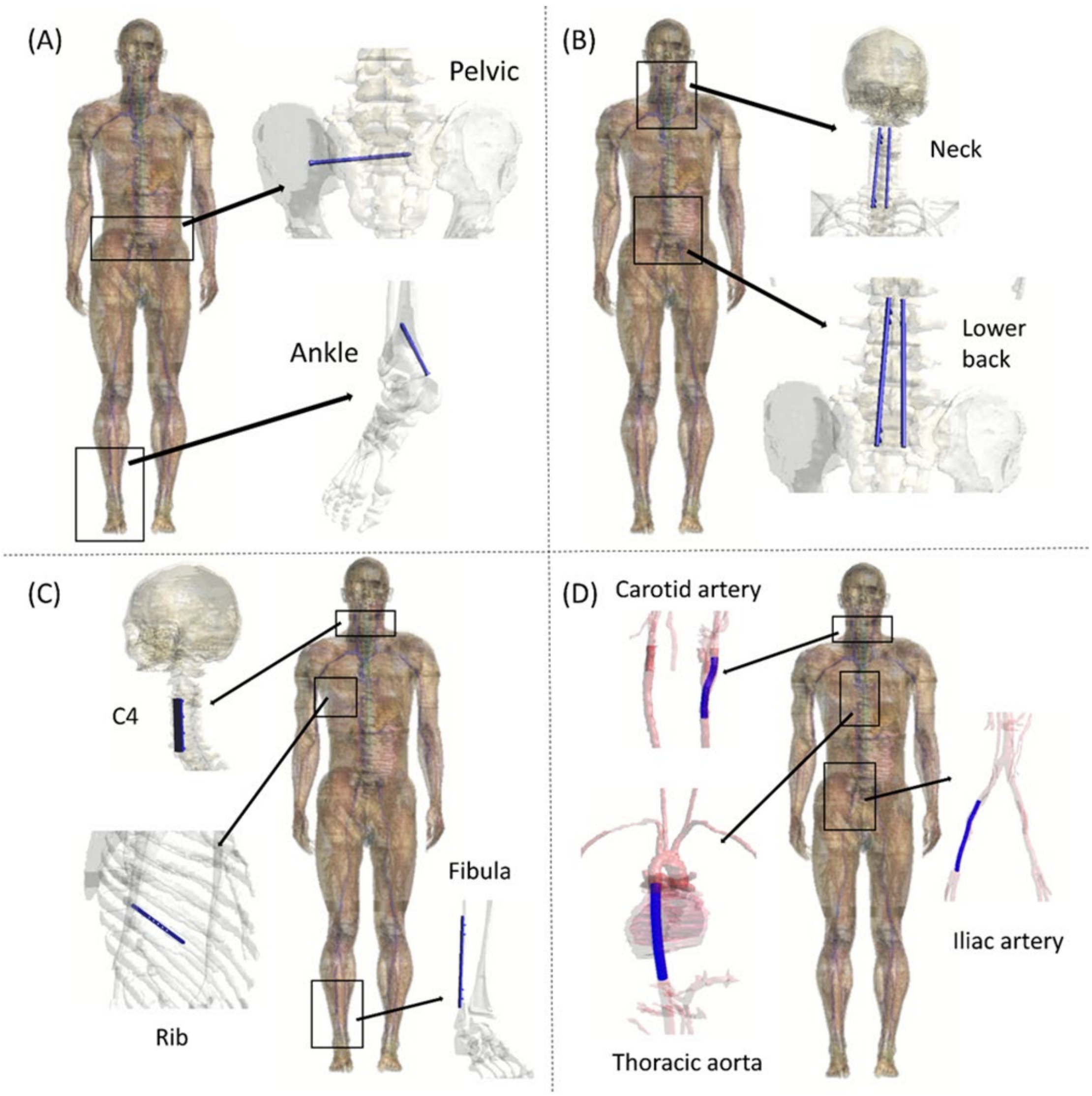

Figure 3-2. A, The implanted positions of the standalone screw system. B, The implanted positions of the pedicle screw system. C, The implanted positions of the plate and screw system. D, The implanted positions of the stent system.

3.2.3. **Electromagnetic simulation setup**

The G32 birdcage coil was used for simulations in this study to model the practical RF coil [52]. The sizes of the G32 coil are: 650 mm in length and 700 mm in diameter for FATS model, 650 mm in length and 630 mm in diameter for Duke and Ella models. To better model the practical MRI equipment, a metal shield with 1500 mm length was used to confine the electromagnetic field inside the coil.

The original and tissue-reduced human models were loaded in the G32 coil at three landmark positions for more comprehensive investigation as shown in Figure 3-3. The implanted passive device was in the center of the coil in the z direction and moved with the human models by 100 mm along the -z and +z directions, respectively. Similarly, for the in vitro simulation, the device was placed in the ASTM phantom at the middle in the y and z directions and 2 cm away from the longest side wall as required in the ASTM standard [9]. Then the ASTM phantom was also placed at three landmark positions to make the device at the 0 mm, 100 mm, and -100 mm along the z direction. The standard ASTM phantom is an Acrylic container with a relative dielectric constant of 3.7 and an electric conductivity of 0 S/m. The Acrylic container is filled with gelled-saline. The relative dielectric constant and conductivity of the gelled-saline are 80.38 and 0.47 S/m, respectively. For both in vivo and in vitro, the passive devices were all set as perfect electric conductor (PEC).

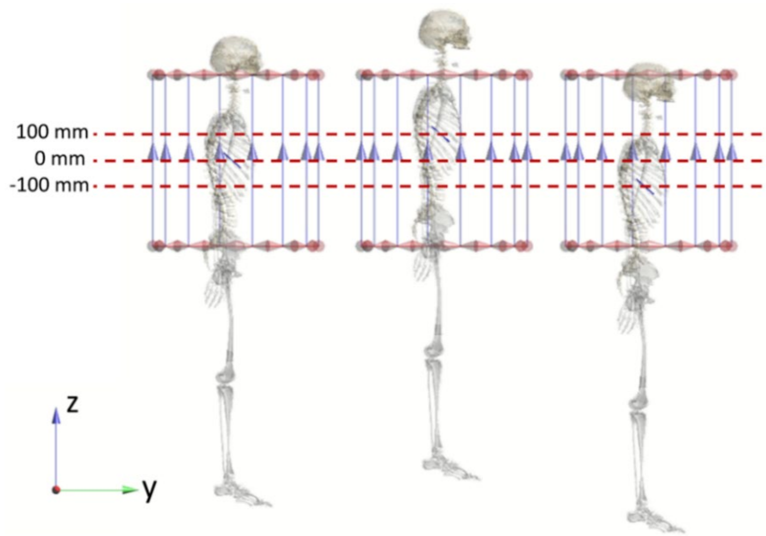

Figure 3-3. The studied three landmarks in simulations: the implanted passive device was in the center of the coil in the z direction (0 mm) and moved by 100 mm along the -z (-100 mm) and +z (100 mm) directions.

The electromagnetic simulations were conducted using the SEMCAD X (V14.8 SPEAG) software. For the simulated MRI system at 1.5 T, the operating frequency is 64 MHz. The boundary conditions for six directions were set to be absorbing boundary conditions (ABC). The simulation time was all set to be 30 periods. After the simulations were finished, the currents, voltages, and E/H field signals of the sensors versus time were checked to confirm that the simulations were converged. Adaptive meshing was adopted. The maximum mesh sizes were 2 mm for the human models, 5 mm for gelled-saline and 10 mm for shell of the phantom. The maximum mesh sizes for the studied passive device systems are shown in Table 3-I. All the results in the ASTM phantom were normalized to a whole-body average SAR of 2 W/kg. Considering that the head and the leg of the human models could be placed around the center of the coil, the head SAR limit and the partial body SAR limit should be checked. Thus, all the results in human models were normalized to the NORMAL OPERATING MODE [30]. The mesh size of the human models was checked for convergence using extrapolation for peak SAR_{1g} near the device and the incident electric field as in Appendix III.

Table 3-I. Maximum mesh sizes for the studied passive device systems.

		Duke	**Ella**	**FATS**
Screw system	Ankle	0.7 mm	0.7 mm	0.7 mm
	Pelvic	0.7 mm	0.7 mm	0.7 mm
Pedicle screw system	Neck	1 mm	1 mm	1 mm
	Lower back	1 mm	1 mm	1 mm

Table 3-I. Maximum mesh sizes for the studied passive device systems. (continued)

Plate and screw system	**C4**	**1 mm for plate, 0.7 mm for screws**	**1 mm for plate, 0.7 mm for screws**	**1 mm for plate, 0.7 mm for screws**
	Fibula	1 mm for plate, 0.7 mm for screws	1 mm for plate, 0.7 mm for screws	1 mm for plate, 0.7 mm for screws
	Rib	0.8 mm for plate, 0.7 mm for screws	0.8 mm for plate, 0.7 mm for screws	0.8 mm for plate, 0.7 mm for screws
Stent system	Carotid artery	0.5 mm	0.5 mm	0.5 mm
	Iliac artery	0.5 mm	0.5 mm	0.5 mm
	Thoracic aorta	0.5 mm	0.5 mm	0.5 mm

3.2.4. **SAR analysis**

To quantify the RF-induced heating, the spatial averaged specific absorption rate over one gram (SAR_{1g}) was proposed as a standard [38] as

$$\text{SAR} = \frac{\sigma|E|^2}{\rho}\ (W/kg), \tag{3-1}$$

where σ is the conductivity of the tissue, ρ is the mass density and E is the root mean square of electric field strength. The SAR averaged to one gram is SAR_{1g}. An uncertainty analysis was conducted for the peak SAR_{1g} near the device as in Appendix IV.

The SAR_{1g} used to quantify the RF-induced heating near the device is the absorbed power averaged to a volume with 1 gram mass. The absorbed power ($\sigma|E|^2$ in (3-1)) is greatly related to the incident electric field and electrical conductivities of the surrounding tissues. The most important difference affecting the peak SAR_{1g} near the device between the ASTM phantom and original human models are the geometrical shape and non-homogeneity of the tissues.

For the geometrical shape: the ASTM phantom has a simple geometrical shape, which means the implanted position of the device cannot be the same as the clinical position in the human models. That directly leads to the different incident electric fields near the device. It influences the absorbed power near the device.

For the non-homogeneity of the tissues: the ASTM phantom is filled with uniform gelled-saline. And the original human models have non-uniform tissues with different parameters. That means the tissues near the implanted device in the ASTM phantom and human models have different parameters. The most important parameter influencing the SAR_{1g} is the electrical conductivity because it will influence the electric field distribution and is directly related to the absorbed power. The electrical conductivities of tissues near the device will influence the power deposition and dissipation around the device.

Thus, because the geometrical shapes of the ASTM phantom and human models are different and the tissues in the human models are non-homogenous, the incident electric field and electrical conductivities of the tissues near the device are different in the human models and ASTM phantom. That means different absorbed power and different RF-induced heating. To calibrate the influence of the incident electric field and electrical conductivities of tissues near the device on the SAR_{1g}, two scaling methods were proposed. For the ASTM phantom, the scaling should be conducted to consider the incident electric field and electrical conductivities of tissues near the device. For the tissue-reduced human model, the scaling should be conducted to consider the electrical conductivities of tissues near the device since the incident electric field inside the tissue-reduced human models is highly correlated to that inside the original human models.

For the simulation in ASTM phantom, a scaling method was applied using the incident electric field and was named as E-scaling. The averaged values of the incident electric field along the tangential direction of the device were extracted in the ATSM phantom and original human models. The detailed formula for the E-scaling value of SAR_{1g} is illustrated as

$$SAR_{1g\_scaling} = SAR_{1g\_phantom} \times \frac{(|Averaged\ incident\ E_{original\ human\ models}|)^2}{(|Averaged\ incident\ E_{ASTM\ phantom}|)^2}, \quad (3\text{-}2)$$

where the $SAR_{1g\_scaling}$ is the scaled result of the SAR_{1g}, the $SAR_{1g\_phantom}$ is the simulated value of SAR_{1g} in the ASTM phantom, the $Averaged\ incident\ E_{original\ human\ models}$ and $Averaged\ incident\ E_{ASTM\ phantom}$ are the averaged values of the tangential incident electric field along the device in the original human models and the ASTM phantom, respectively. The ASTM phantom has one main drawback. That is, its shape is too simple and the device in the phantom is not implanted in the clinical position. Thus, the incident electric field will be different from that in the real human body. The E-scaling method is an improvement for the ATSM phantom to calibrate the influence of the incident electric field.

For the simulations in the phantom and tissue-reduced human models, another scaling for considering the electrical conductivities of the surrounding tissues was proposed and was named as σ-scaling. Although the tissue-reduced virtual family models have a great correlation for incident electric field with the original models, the RF-induced heating is also significantly related to the electrical properties of the surrounding tissues [37], [39]. For the implanted passive device, the incident electric field will determine the input power, while the electrical conductivities of the surrounding tissues will influence the power deposition and dissipation [39]. Both the incident electric field and surrounding tissues' electrical conductivities will affect the absorbed power around the implanted passive device. The tissues' electrical conductivities range from 0 (the internal air, the pharynx, and so on) to 2.07 S/m (cerebrospinal fluid) for the original human models and range from 0.07 S/m to 0.67 S/m for the simplified human models. Thus, around the same location, the ratio of averaged electrical conductivity in the original models to that in the tissue-reduced models can be as large as around three times. To calibrate the influence of the electrical conductivities of surrounding tissues on SAR_{1g}, a series of simulations in the ASTM phantom were conducted for a standard rod made from titanium [9]. The rod has a length of 10 cm and a diameter of 1/8 inches. The electrical conductivity of the gelled-saline near one end of the rod in a 15 mm×15 mm×15 mm cubic was changed from 0 to 1.80 S/m. The hotspot located at this end (the top end of the rod in Figure 3-4 A) when the electrical conductivity of the gelled-saline was all set to 0.47 S/m. The rod and the phantom are shown in Figure 3-4 A. The peak SAR_{1g} at this end versus the electrical conductivity of surrounding gelled-saline is shown in Figure 3-4 B. The curve in Figure 3-4 B shows a simple relationship between the electrical conductivity of tissue and

SAR_{1g}. Then for the original human models, the tissue-reduced human models, and the ASTM phantom, the averaged electrical conductivities in a 10 mm×10 mm×10 mm cubic near the hotspots (positions of peak SAR_{1g} around the device) in the original human models were extracted. The formula for the σ-scaling is

$$SAR_{1g\_scaling} = SAR_{1g\_simulated} \times \frac{SAR_{Figure\ 3-4B\ averaged\ \sigma\ of\ original\ human\ models}}{SAR_{Figure\ 3-4B\ averaged\ \sigma\ of\ tissue-reduced\ human\ models\ or\ ASTM\ phantom}}, \quad (3\text{-}3)$$

where the $SAR_{1g\_}scaling$ is the scaled value of SAR_{1g} for the simplified human models or ASTM phantom, the $SAR_{1g\_simulated}$ is the simulated value of SAR_{1g} for the simplified human models or the ASTM phantom. The $SAR_{Figure\ 3-4B\ averaged\ \sigma\ of\ original\ human\ models}$ is the value of SAR_{1g} in the Figure 3-4 B corresponding to the extracted averaged electrical conductivity of the surrounding tissues near the hotspot in the original human models. The $SAR_{Figure\ 3-4B\ averaged\ \sigma\ of\ tissue-reduced\ human\ models\ or\ ASTM\ phantom}$ is the value of SAR_{1g} in the Figure 3-4 B corresponding to the extracted averaged electrical conductivity of the surrounding tissues in the simplified human models or ASTM phantom. To show the σ-scaling can make the peak SAR_{1g} near the device in the tissue-reduced human models match better with that in the original human models, the results with and without the σ-scaling in tissue-reduced human models are attached in the Appendix V.

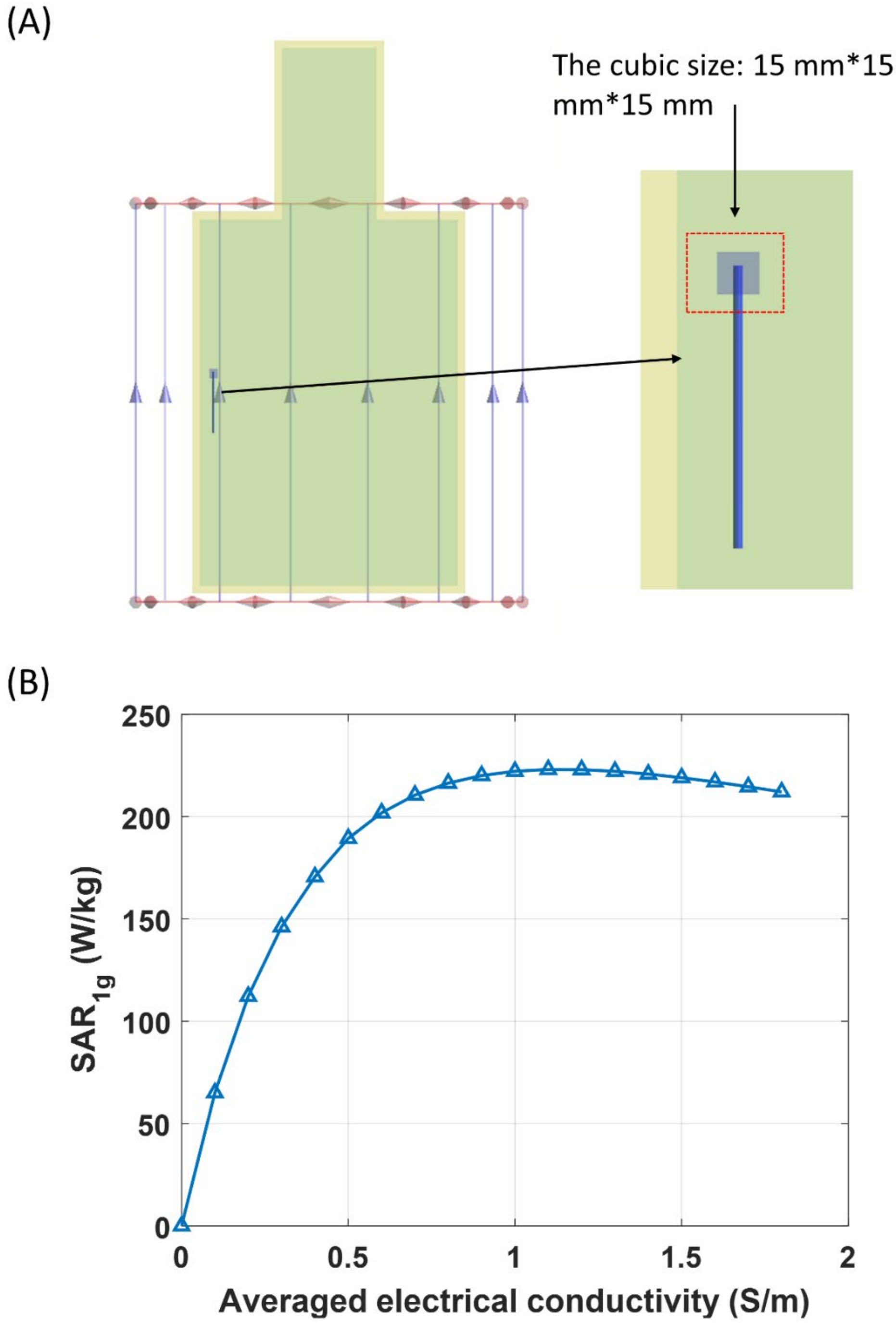

Figure 3-4. A, The rod and the phantom used for σ-scaling. B, The SAR_{1g} at the top end of the rod versus the electrical conductivity of surrounding gelled-saline in the 15 mm*15 mm*15 mm cubic.

3.3. Results and discussion

3.3.1. Peak SAR_{1g} near the device comparison

The values of peak SAR_{1g} near the implanted passive device in the original human models were extracted. And the values of SAR_{1g} near the same locations as in the original human models of the simplified human models and the ASTM phantom were also extracted for comparison. The extracted values of SAR_{1g} in the ASTM phantom were scaled using the incident electric field (the E-scaling) for a more comprehensive comparison as explained in the Method part. In this study, the influence of surrounding tissues' electrical conductivities on the SAR_{1g} was considered and another scaling (the σ-scaling) to the results of the simplified human models and the ASTM phantom was conducted as illustrated in the Method part. The results are shown in Figure 3-5. As shown in Figure 3-5, compared to the results of the ASTM phantom with or without E-scaling, the values of SAR_{1g} of the tissue-reduced virtual family models have the best correlation with those of the original human models. In detail, the correlation coefficient between the SAR_{1g} of the original human models and the SAR_{1g} of the tissue-reduced human models is as high as 0.99. And the correlation coefficients between the SAR_{1g} of the original human models and the SAR_{1g} of the ASTM phantom are 0.65 and 0.94 without and with E-scaling respectively. The least-square fit polynomial coefficients of the first degree were calculated for the data represented by the black circles, red squares, and blue triangles, respectively. The polynomial coefficients with the highest power are the slopes of the fitting straight lines and are shown in Figure 3-5 as the s of the legend. The slopes are 0.97 for the tissue-reduced virtual family, 0.58 for the ASTM phantom, and 2.34 for the ASTM phantom with E-scaling. From the correlation coefficients and the slopes, the tissue-reduced human models can evaluate the peak SAR_{1g} near the studied passive device more accurately than that of the ASTM phantom even with the E-scaling to calibrate the incident electric field along the device inside the phantom.

Generally, the SAR_{1g} evaluated in the ASTM phantom without E-scaling is conservative except some special cases like the device implanted in the fibula region or the neck region. Compared to the SAR_{1g} in the original human models, the relative errors of the SAR_{1g} in the ASTM phantom without E-scaling can be lower than -10%. The most extreme outlier in the lower right corner in Figure 3-5 is the plate and screw system implanted in the fibula region of the FATS model at 100 mm landmark position. That outlier has a relative error as -37.15%, which is the lowest relative error among the results in the ASTM phantom without E-scaling. Other cases that the ASTM phantom without E-scaling is obviously not conservative (with a relative error lower than -10%) are the pedicle screw system implanted in the neck region of the Duke model at 0 mm and -100 mm landmark positions, the plate and screw system implanted in the fibula region of the Ella model at 100 mm landmark position, the pedicle screw system implanted in the neck region of the Ella model at 0 mm landmark position, the plate and screw system implanted in the fibula region of the FAST model at 0 mm landmark position, and the plate and screw system implanted in the fibula region of the Duke model at 100 mm landmark position. These results show that the ASTM phantom is mainly not conservative for the plate and screw system implanted in the fibula region and the pedicle screw system implanted in the neck region. For these cases, the main trunk of the body is not inside the coil, which leads to very high input power for normalization to the Normal Operating Mode. And that leads to stronger incident electric field near the device in the original human models than that in the ASTM phantom. It will result in higher SAR_{1g} in the original human model than that in the ASTM phantom without the E-scaling. When the device is a standalone screw implanted in the pelvic region, the ASTM phantom is overly conservative. The value of SAR_{1g} in ASTM phantom can be 2402.57% higher than that in original Ella model with the standalone screw implanted in the pelvic region at 0 mm landmark position. For the tissue-reduced human models, they are not aimed at getting conservative results but aimed at getting more closer SAR_{1g} evaluation to that in original human models. From the Figure 3-5, the tissue-reduced human models are not conservative for many cases, but the evaluated SAR_{1g} values in the tissue-reduced human models have a high correlation with those in the original human models.

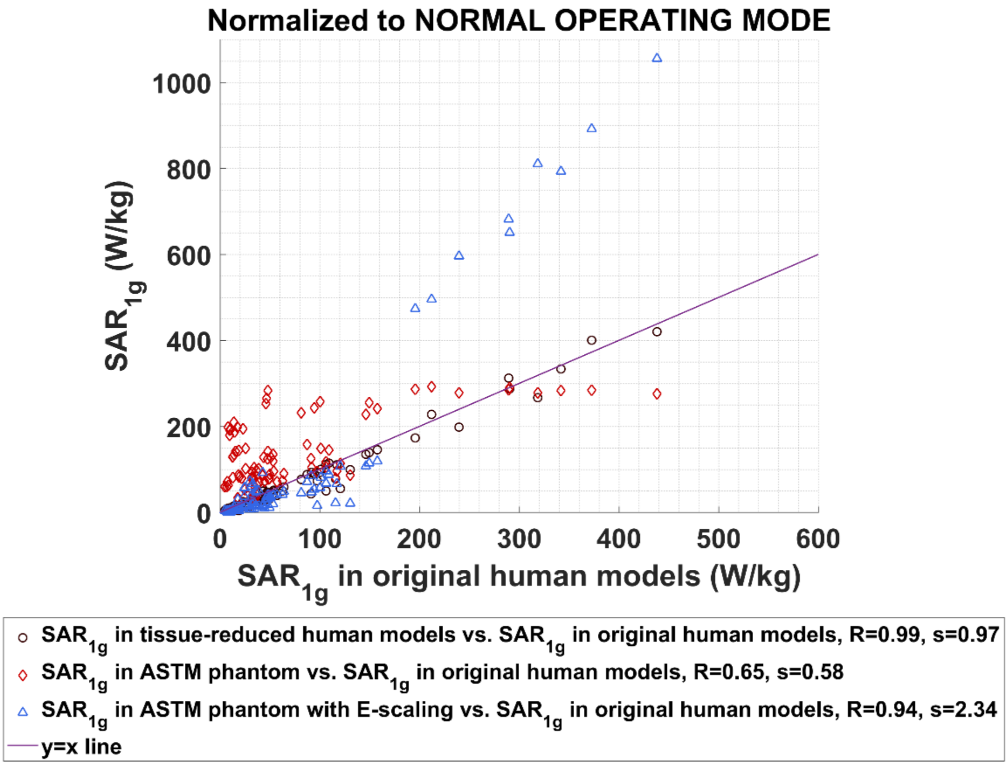

Figure 3-5. Results of the SAR_{1g} for all simulations at the positions of peak SAR_{1g} near the implanted passive device in the original human models at 1.5 T. The R is the correlation coefficient, and the s is the slope of the fitting straight line in the legend.

For a more comprehensive investigation, SAR_{1g} in the tissue-reduced human models were compared to those in ASTM phantom with and without E-scaling. The comparison is shown in Figure 3-6. From this figure, the ASTM phantom without the E-scaling has more conservative results of the SAR_{1g} than those of the tissue-reduced human models for most cases except that the device implanted in the fibula region. With the E-scaling, the results of the ASTM phantom become less or more conservative depending on the implanted positions of the device. Because the implanted positions of the device will directly influence the incident electric field near the device, the evaluated SAR_{1g} with E-scaling will be influenced.

To consider the uncertainty coming from the loading position, grid resolution and tissues' properties, an uncertainty analysis was conducted as in Appendix IV [53]-[56]. The combined uncertainty was calculated as 4.12% at 1.5 T.

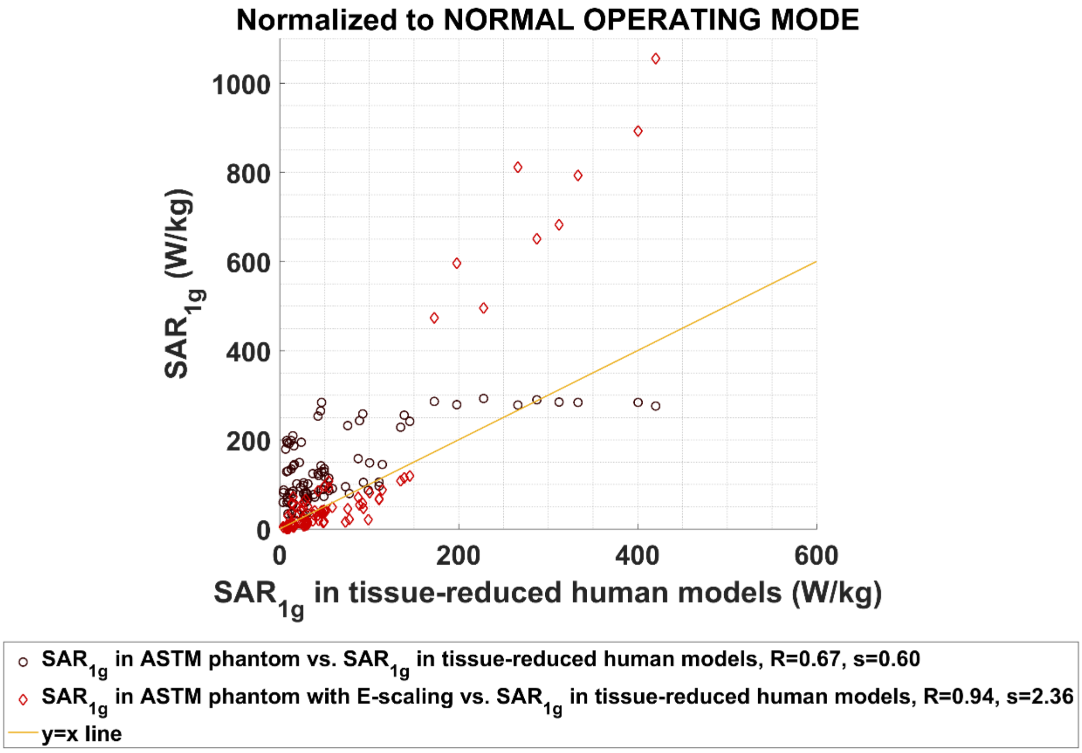

Figure 3-6. Comparison of the SAR_{1g} in tissue-reduced human models and ASTM phantom with or without E-scaling at 1.5 T. The R is the correlation coefficient, and the s is the slope of the fitting straight line in the legend.

3.3.2. SAR_{1g} distribution near the device comparison

Besides the peak SAR_{1g} near the implanted passive device, the SAR_{1g} distribution near the device was also used for comparison. As shown in Figure 3-7, the plate and screw system on the fibula at 0 mm landmark position was used as an example. Obviously, the tissue-reduced human models have quite similar SAR_{1g} distributions near the implanted passive device compared to those of the original human models. While the SAR_{1g} distributions near the device in the

ASTM phantom are significantly different from those in the original human models.

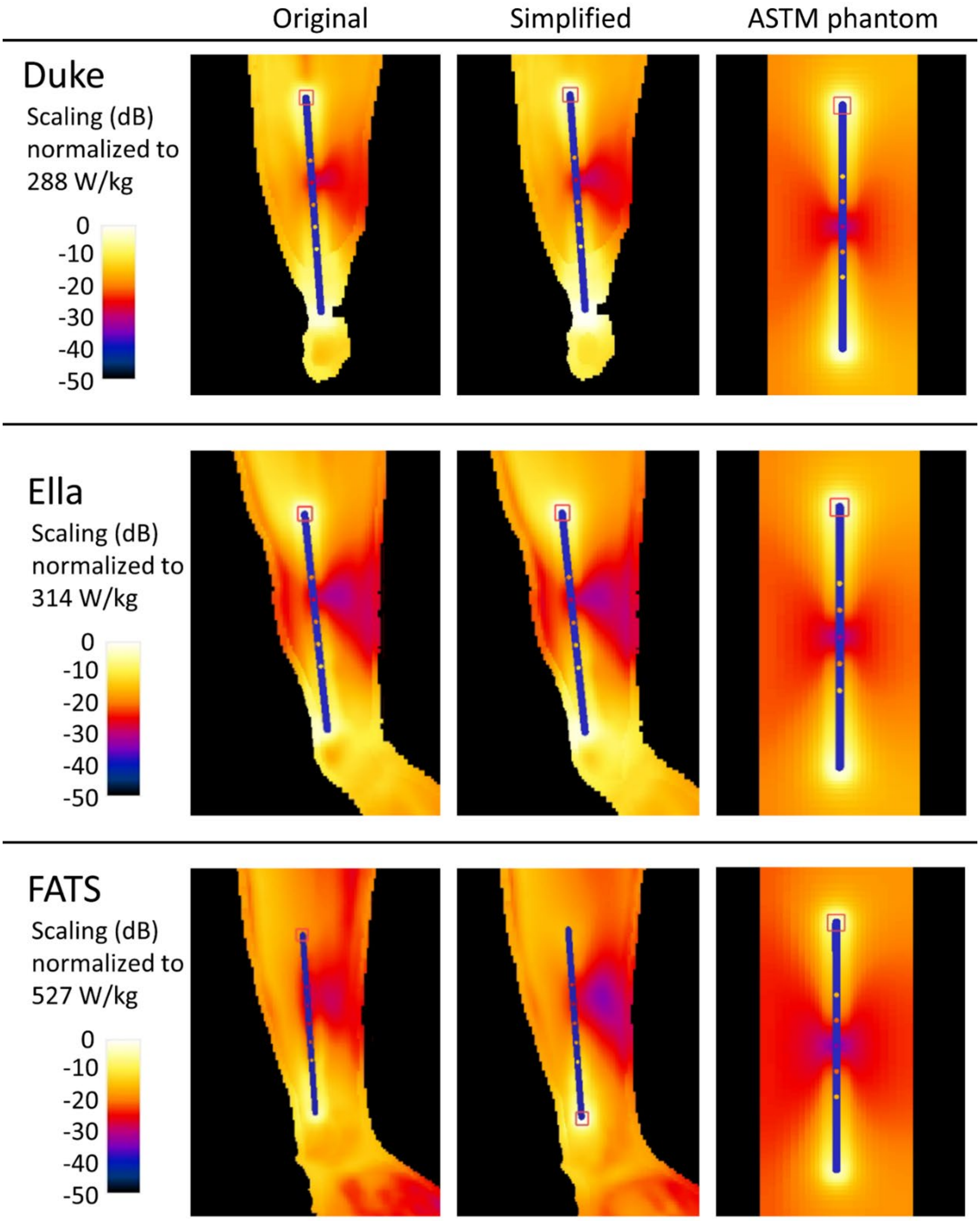

Figure 3-7. SAR_{1g} distributions near the device for the plate and screw system on fibula under 0 mm landmark position in Duke model.

One main reason could be that the passive devices in the original or tissue-reduced human models were placed in identical clinical positions and the devices in the ASTM phantom were placed in a fixed position required by ASTM standard [9]. Thus, the incident electric field will be quite different for the human models (original or tissue-reduced) and the ASTM phantom. And for the original and simplified human models, they have a high correlation in terms of the incident electric field. So, the input power from the RF coil is quite similar for the original and simplified human models. Another main reason for the different SAR_{1g} distribution in the original human models and the ASTM phantom can be that the gelled-saline in the ASTM phantom is uniform. Thus, the method using the ASTM phantom to evaluate the SAR_{1g} will not account the influence of the non-homogeneity of the human tissues on the SAR_{1g}. The parameters of the tissues near the device are pretty different in ASTM phantom and human models. And the most important parameter to the SAR_{1g} is the electrical conductivity which will influence the electric field distribution and is directly related to the absorbed power ($\sigma|E|^2$). Although the tissue-reduced human models simplify the human tissues to two types, it still partly considers the non-homogeneity of the human tissues and should have better performance on the SAR_{1g} evaluation than that of the uniformly filled ASTM phantom.

The moduli of tangential incident electric field along devices implanted in three representative regions were extracted and plotted in Figure 3-8. The three representative devices are the plate and screw system implanted near the fibula, the standalone screw system implanted near the pelvic and the stent system implanted in the carotid artery near the neck. These devices were implanted in the tibia, trunk, and neck regions in the human models, respectively. From Figure 3-8, the tangential incident electric field near the devices in the original human models and tissue-reduced human models has a high correlation. While the tangential incident electric field near the devices in the ASTM phantom is obviously different from that in the original and tissue-reduced human models.

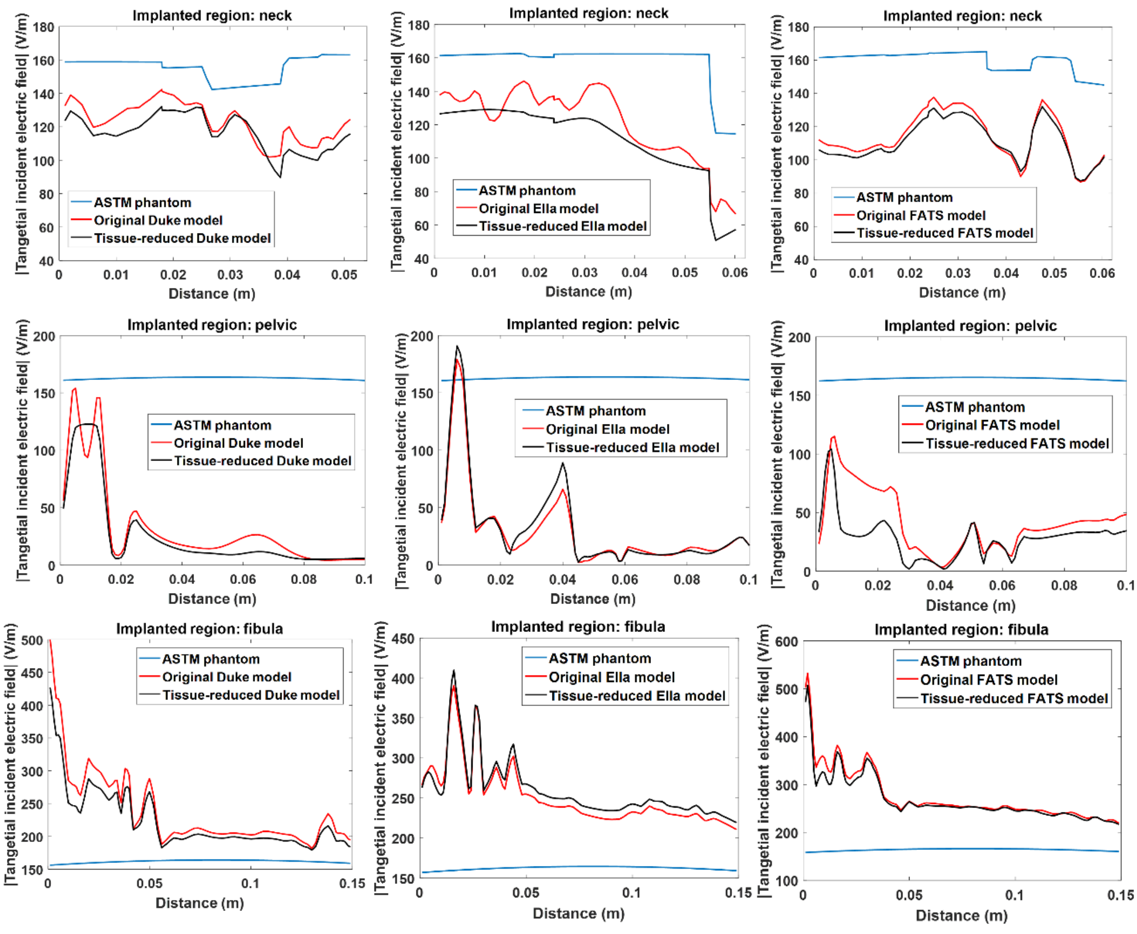

Figure 3-8. The moduli of tangential incident electric field along devices comparison.

In this study, the tissue-reduced virtual family models using the Gaussian Mixture Method were investigated for evaluating the peak SAR_{1g} near the passive device. As in our previous study, the VWCk2 human models only have two types of tissues and have a great correlation with the original human models in terms of the electric field. The VWCk2 human models also perform well in evaluating the RF-induced heating for the AIMDs. For the passive device, the SAR is used for quantifying the RF-induced heating coming from the implanted device. From the simulated results of the peak SAR_{1g} neat the device as in Figure 3-5 and the SAR_{1g} distribution near the device as in Figure 3-7, the tissue-reduced human models can evaluate the SAR_{1g} near the studied passive device more accurately than the ASTM phantom. The tissue-reduced virtual family models have more accurate predictions for the peak SAR_{1g} near the device than those of the ASTM phantom. They also have significantly fewer types of tissues (2 types) compared to those in the original human models (34 types for Duke and FATS, 36 types for Ella). Thus, the tissue-reduced human models can bridge the gap between the original human models and the ASTM phantom to get a balance between accuracy and complexity. That will make the experimental study in the human models more feasible and yield a more accurate evaluation for the peak SAR_{1g} near the device than that of the experiment inside the ASTM phantom.

Compared to the ASTM phantom with a simple geometrical shape and uniformly filled gelled-saline, the tissue-reduced virtual family models keep the geometrical shape of the human body and partly considers the non-homogeneity of the human tissues. That makes the tissue-reduced human models have more similar incident electric field and surrounding tissues' properties around the device compared to those in the original human models than those in the ASTM phantom. The incident electric field and surrounding tissues' properties near the implanted passive device are the two key factors to influence the RF-induced heating near the device. The incident electric field determines the input power while the surrounding tissues' properties especially the electrical conductivity influence the power dissipation and distribution. Totally, compared to the ASTM phantom, the proposed tissue-reduced virtual family models (VWCk2 models) have a better performance on accurately evaluating the peak SAR_{1g} near the device .

3.4. **Conclusions**

For the studied four passive device systems, compared to the ASTM phantom, the proposed VWCk2 models have:

a. higher correlation in terms of the peak SAR_{1g} near the device with that of the original human models.

b. more similar SAR_{1g} distribution near the device with that of the original human models.

To balance complexity and accuracy for evaluating the RF-induced heating and make the experimental study in human models more practical, it is necessary to propose the simplified human models. The simplified human models should have fewer types of tissues compared to the original human models and have enough accurate results for heating evaluation. The VWCk2 human models using the Gaussian Mixture Method based on the real and imaginary parts of the relative effective permittivities of the tissues were proposed as a tissue-reduced version of the virtual family human models. This study tried to investigate the possible application of the tissue-reduced human models on the RF-induced heating evaluation for the passive device. Electromagnetic simulations were conducted for the original human models, the tissue-reduced human models, and the ASTM phantom with four common and representative passive device systems implanted. The results of SAR_{1g} were used to access the performance of the tissue-reduced human models on evaluating the RF-induced heating.

A σ-scaling was conducted for the results of peak SAR_{1g} near the device to take the surrounding tissues' electrical conductivities into consideration. From the results of the peak SAR_{1g} near the device, the correlation coefficient is as high as 0.99 between the SAR_{1g} of the original human models and the tissue-reduced human models and are 0.65 and 0.94 between the SAR_{1g} of the original human models and the ASTM phantom without and with E-scaling respectively. Compared to the ASTM phantom, the SAR_{1g} distribution near the implanted device of the simplified human models matches better that of the original human models. In conclusion, the proposed tissue-reduced virtual family models are prior to the ASTM phantom to evaluate the peak SAR_{1g} near the device accurately because the tissue-reduced human models keep the geometrical shape of the human body and partly consider the non-homogeneity of the human tissues. The tissue-reduced human models are also greatly simpler than the original human models. It makes the fabrication of the human models for experimental study in the future more feasible and practical.

Chapter 4. TISSUE-REDUCED VIRTUAL FAMILY MODELS AND THEIR APPLICATION ON RF-INDUCED HEATING EVALUATION OF PASSIVE MEDICAL IMPLANTS AT 3 T

4.1. Introduction

To make the experimental study more practical, the tissue-reduced virtual family models were proposed for RF-induced heating evaluation at 1.5 T. In previous study, the peak SAR_{1g} near the device of some representative passive device systems was evaluated inside the original virtual family models, tissue-reduced virtual family models and ASTM phantom. The simulated results were compared to each other for investigating the performance of the tissue-reduced virtual family models on evaluating the peak SAR_{1g} near the passive devices and making the experimental study more practical for the 1.5 T MRI system. The Volume-Weighing Tissue-Cluster models with 2 clusters (VWCk2) developed based on the Gaussian mixture model (GMM) were adopted as the tissue-reduced virtual family models at 1.5 T. Numerical electromagnetic simulations based on finite-difference time-domain (FDTD) method were conducted in the G32 birdcage coil at 1.5 T. Four representative passive device systems, the standalone screw system, the pedicle screw system, the plate and screw system and the stent system, were implanted in the original virtual family models, tissue-reduced virtual family models and ASTM phantom at three landmark positions for comprehensively study.

From the results at 1.5 T, compared to the values of peak SAR_{1g} near the device in the original human models, the values of SAR_{1g} at the same position around the device in the tissue-reduced virtual family models have a great correlation coefficient as high as 0.99. While the correlation coefficients between the peak SAR_{1g} near the device in the original human models and the SAR_{1g} around the same positions near the device in the ASTM phantom are 0.65 for results without E-scaling and 0.94 for results with E-scaling. For the studied four passive device systems, the tissue-reduced virtual family models have a more accurate evaluation of the peak SAR_{1g} near the device than that of the ASTM phantom. And compared to the ASTM phantom, the tissue-reduced virtual family models have a more similar SAR_{1g} distribution around the device and incident electric field distribution along the device to those of the original human models. The proposed tissue-reduced virtual family models at 1.5 T have only two types of tissues. It shows that developing the tissue-reduced virtual family models for the experimental study is feasible and practical at 1.5 T.

The common MRI systems can operate at 64 MHz (1.5 T) and 128 MHz (3 T). Thus, for more comprehensively investigation of the tissue-reduced virtual family models, the Volume-Weighing Tissue-Cluster models with 2 clusters (VWCk2) were also developed based on the Gaussian mixture model (GMM) at 3 T. After that, EM simulation will be conducted in a G32 coil and a correlation analysis for the electric field between the original human models and tissue-reduced virtual family models will also be conducted. The same passive device systems as those at

1.5 T were also implanted in the original virtual family models, tissue-reduced virtual family models and ASTM phantom at three landmark positions for the 3 T system. That aims to investigate the performance of the tissue-reduced virtual family models on RF-induced heating evaluation for passive device at 3 T. The results will show us the feasibility of using tissue-reduced models for the RF-induced heating testing of implantable medical devices at 3 T.

4.2. Tissue-reduced virtual family models for 3 T MRI system

4.2.1. The original human models and the tissues' parameters at 3 T

The operating frequency at 3 T is 128 MHz. The frequency will influence the electrical conductivities and relative permittivities of the human tissues. The comparison of the electrical conductivities and relative permittivities at 1.5 T and 3 T is shown in Table 4-I with the Duke model as an example [57].

Table 4-I. The electrical conductivities and relative permittivities at 1.5 T and 3 T of tissues in the Duke model.

Tissues in Duke model	Electrical conductivity in S/m at 1.5 T	Electrical conductivity in S/m at 3 T	Relative permittivity at 1.5 T	Relative permittivity at 3 T
Adrenal_gland	0.78	0.80	73.95	66.78
Air_internal	0.00	0.00	1.00	1.00
Artery	1.21	1.25	86.44	73.16
Bladder	0.29	0.30	24.59	21.86
Blood_vessel	1.21	1.25	86.44	73.16
Bone	0.06	0.07	16.68	14.72
Brain_grey_matter	0.51	0.59	97.43	73.52
Brain_white_matter	0.29	0.34	67.84	52.53
Bronchi	0.53	0.56	58.89	50.57
Bronchi_lumen	0.00	0.00	1.00	1.00
Cartilage	0.45	0.49	62.91	52.92
Cerebellum	0.72	0.83	116.35	79.74
Cerebrospinal_fluid	2.07	2.14	97.31	84.04
Commissura_anterior	0.29	0.34	67.84	52.53

Table 4-I. The electrical conductivities and relative permittivities at 1.5 T and 3 T of tissues in the Duke model. (continued)

Commissura_posterior	0.29	0.34	67.84	52.53
Connective_tissue	0.47	0.50	59.49	51.86
Cornea	1.00	1.06	87.38	71.46
Diaphragm	0.69	0.72	72.23	63.49
Ear_cartilage	0.45	0.49	62.91	52.92
Ear_skin	0.44	0.52	92.17	65.44
Epididymis	0.88	0.93	84.53	72.13
Esophagus	0.88	0.91	85.82	74.90
Esophagus_lumen	0.00	0.00	1.00	1.00
Eye_lens	0.29	0.31	50.34	42.79
Eye_Sclera	0.88	0.92	75.30	65.00
Eye_vitreous_humor	1.50	1.51	69.13	69.06
Fat	0.07	0.07	13.64	12.37
Gallbladder	1.48	1.58	105.44	88.90
Heart_lumen	1.21	1.25	86.44	73.16
Heart_muscle	0.68	0.77	106.51	84.26
Hippocampus	0.51	0.59	97.43	73.52
Hypophysis	0.78	0.80	73.95	66.78
Hypothalamus	0.78	0.80	73.95	66.78
Intervertebral_disc	0.45	0.49	62.91	52.92
Kidney_cortex	0.74	0.85	118.56	89.62
Kidney_medulla	0.74	0.85	118.56	89.62
Large_intestine	0.64	0.71	94.66	76.57
Large_intestine_lumen	0.69	0.72	72.23	63.49
Larynx	0.45	0.49	62.91	52.92
Liver	0.45	0.51	80.56	64.25
Lung	0.29	0.32	37.10	29.47
Mandible	0.06	0.07	16.68	14.72
Marrow_red	0.15	0.16	16.44	13.54
Medulla_oblongata	0.72	0.83	116.35	79.74
Meniscus	0.45	0.49	62.91	52.92
Midbrain	0.72	0.83	116.35	79.74
Mucosa	0.49	0.54	76.72	61.59
Muscle	0.69	0.72	72.23	63.49
Nerve	0.31	0.35	55.06	44.07
Pancreas	0.78	0.80	73.95	66.78
Patella	0.06	0.07	16.68	14.72
Penis	0.43	0.48	68.64	55.99
Pharynx	0.00	0.00	1.00	1.00
Pinealbody	0.78	0.80	73.95	66.78

Table 4-I. The electrical conductivities and relative permittivities at 1.5 T and 3 T of tissues in the Duke model. (continued)

Pons	0.72	0.83	116.35	79.74
Prostate	0.88	0.93	84.53	72.13
SAT	0.07	0.07	13.64	12.37
Skin	0.44	0.52	92.17	65.44
Skull	0.06	0.07	16.68	14.72
Small_intestine	1.59	1.69	118.36	87.97
Small_intestine_lumen	0.69	0.72	72.23	63.49
Spinal_cord	0.31	0.35	55.06	44.07
Spleen	0.74	0.84	110.56	82.89
Stomach	0.88	0.91	85.82	74.90
Stomach_lumen	0.69	0.72	72.23	63.49
Teeth	0.06	0.07	16.68	14.72
Tendon_Ligament	0.47	0.50	59.49	51.86
Testis	0.88	0.93	84.53	72.13
Thalamus	0.51	0.59	97.43	73.52
Thymus	0.78	0.80	73.95	66.78
Thyroid_gland	0.78	0.80	73.95	66.78
Tongue	0.65	0.69	75.30	65.00
Trachea	0.53	0.56	58.89	50.57
Trachea_lumen	0.00	0.00	1.00	1.00
Ureter_Urethra	0.43	0.48	68.64	55.99
Vein	1.21	1.25	86.44	73.16
Vertebrae	0.06	0.07	16.68	14.72

Moreover, the real and imaginary parts of the relative effective permittivity $\left(\varepsilon_r - j\frac{\sigma}{\omega\varepsilon_0}\right)$ were chosen for fitting since the electric field and magnetic field are related to each other via the relative effective permittivity. The frequency will influence the imaginary parts $(j\frac{\sigma}{\omega\varepsilon_0})$, which will also influence the fitting of the data.

The scatter plots for the tissues' properties based on the electrical conductivities and relative permittivities are shown in Figure 4-1 A for the Duke and FATS models and in Figure 4-1 B for the Ella model. And the scatter plots for the tissues' properties based on the real and imaginary parts of the relative effective permittivity are shown in Figure 4-1 C for the Duke and FATS models and in Figure 4-1 D for the Ella model. Compared to Figure 2-1, the tissues' scatter plots at 3 T are slightly different from those at 1.5 T. Those could affect the results of clustering and the electrical parameters of every cluster. However, the volume weights of all tissues are identical for the human models at 1.5 T and 3 T.

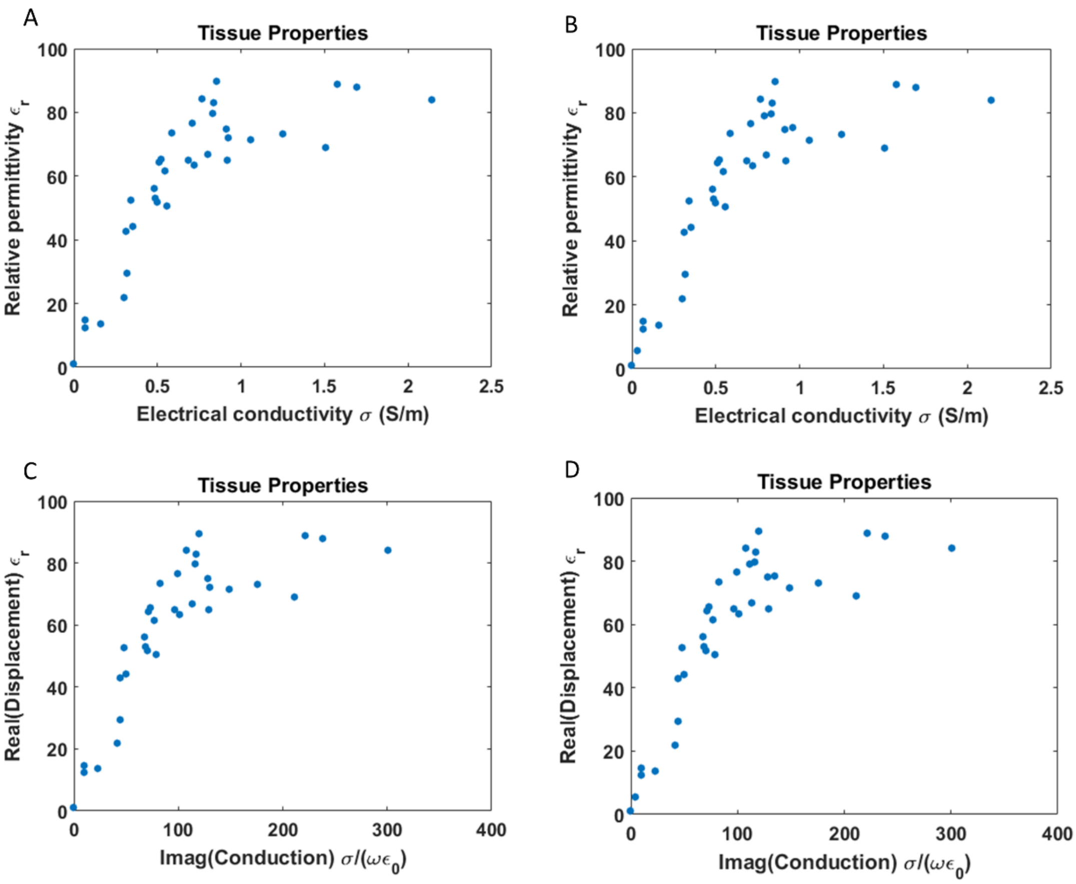

Figure 4-1. Scatter plots for the tissue properties at 3 T.

4.2.2. Tissue-reduced virtual family models development at 3 T

Based on the research at 1.5 T, the chosen tissue-reduced virtual family models have only two types of tissue to make the experimental study feasible in the future. And their electric field is highly correlated to that in the original models. Thus, the chosen tissue-reduced virtual family models are a great choice to balance the accuracy and complexity for RF-induced heating evaluation. At 3 T, to make the experimental study feasible and yield a high correlation for the electric field, the same cluster method as for 1.5 T (cluster method 3) with 2 clusters was adopted for the 3 T MRI system. The details of the clusters are shown in Table 4-II. Electromagnetic simulations were also conducted to investigate the correlation of electric field. Similar to the clusters at 1.5 T, the main tissues in cluster 1 are the bone and fat with smaller values of electrical conductivity and relative permittivity. And the main tissues in cluster 2 are the muscle and skin with larger values of electrical conductivity and relative permittivity.

Table 4-II. Detailed parameters for the chosen tissue-reduced virtual family models at 3 T.

	Cluster 1			Cluster 2		
	Bone, fat, …			Muscle, skin, …		
	ε_r	σ (S/m)	ρ (kg/m^3)	ε_r	σ (S/m)	ρ (kg/m^3)
Duke	15.87	0.12	1001.00	64.74	0.72	1090.80
Ella	14.04	0.09	992.90	64.03	0.71	1126.00
FATS	12.60	0.07	991.01	63.03	0.69	1063.50

4.2.3. **Electromagnetic simulations and correlation analysis**

The electromagnetic simulations were conducted for the three original human models (the original Duke, Ella, and FATS models) and the three tissue-reduced human models (the tissue-reduced Duke, Ella, and FATS models) at 3 T. The SEMCAD X (V14.8 SPEAG) software was also used for simulations at 3 T. The Duke, Ella and FATS models were also loaded under three landmark positions as shown in Figure 2-7. At 3 T, the frequency was set to 128 MHz. The boundary conditions for six directions, simulation time and maximum mesh size for the human models were all set the same as those at 1.5 T. All the results in human models were normalized to the NORMAL OPERATING MODE [30].

The same correlation analysis between the electric field in the original and tissue-reduced human models as at 1.5 T was conducted at 3 T. The electric field in several different body regions was extracted as shown in Figure 2-8. The correlation coefficients for the electric field along the *x*, *y* and *z* direction and the module of the electric field are shown in Table 4-III for the Duke model, Table 4-IV for the Ella model and Table 4-V for the FATS model.

From the results of the correlation coefficients, the modules for all calculated correlation coefficients are not lower than 0.96. The phase for all calculated correlation coefficients is between -0.04 rad to 0.1 rad. Thus, the proposed tissue-reduced virtual family models at 3 T have a great electric field correlation with the original human models. And they show the possible application of the tissue-reduced virtual family models on RF-induced heating evaluation at 3 T.

Table 4-III. The correlation coefficients between the original Duke model and the chosen tissue-reduced Duke model at 3 T.

Landmark positions	400mm		600mm		800mm	
Correlation coefficient	module	phase	module	phase	module	phase
R of Ex_left_arm	1.00	-0.02	1.00	0.02	1.00	0.02
R of Ey_left_arm	0.99	-0.01	1.00	0.01	1.00	0.01
R of Ez_left_arm	1.00	-0.03	1.00	0.00	1.00	0.00
R of E_left_arm	1.00	0.00	1.00	0.00	1.00	0.00
R of Ex_right_arm	1.00	-0.04	0.99	0.02	0.99	0.03
R of Ey_right_arm	1.00	-0.02	0.99	0.02	0.99	0.02
R of Ez_right_arm	1.00	-0.02	1.00	0.01	1.00	0.01
R of E_right_arm	0.99	0.00	0.99	0.00	0.99	0.00
R of Ex_left_tibia	0.99	0.02	0.99	0.00	0.99	0.00
R of Ey_left_tibia	0.99	0.02	0.99	0.00	0.99	0.01
R of Ez_left_tibia	0.98	0.07	0.98	0.03	0.98	0.05

Table 4-III. The correlation coefficients between the original Duke model and the chosen tissue-reduced Duke model at 3 T. (continued)

R of E_left_tibia	0.99	0.00	0.99	0.00	0.99	0.00
R of Ex_right_tibia	0.99	0.04	0.99	0.00	0.99	0.01
R of Ey_right_tibia	0.99	0.09	0.99	0.05	1.00	0.01
R of Ez_right_tibia	0.99	0.10	0.99	0.05	0.98	0.01
R of E_right_tibia	0.99	0.00	0.99	0.00	0.99	0.00
R of Ex_hip_femur	0.99	-0.01	0.99	-0.02	0.99	-0.01
R of Ey_hip_femur	0.99	0.00	0.99	-0.01	0.99	-0.02
R of Ez_hip_femur	0.99	-0.04	1.00	-0.04	1.00	-0.04
R of E_hip_femur	0.99	0.00	0.99	0.00	0.99	0.00
R of Ex_body	0.98	-0.02	0.96	0.03	0.97	0.03
R of Ey_body	0.97	-0.01	0.96	0.01	0.97	0.01
R of Ez_body	0.99	-0.01	0.99	-0.02	0.99	-0.02
R of E_body	0.96	0.00	0.97	0.00	0.98	0.00
R of Ex_head	0.99	-0.02	0.98	-0.03	0.97	0.02
R of Ey_head	0.98	0.00	0.98	0.00	0.98	0.00
R of Ez_head	0.99	-0.04	0.98	0.00	0.98	0.03
R of E_head	0.99	0.00	0.99	0.00	0.98	0.00
R of Ex_total	0.98	-0.02	0.98	0.00	0.98	0.00
R of Ey_total	0.98	-0.01	0.98	0.00	0.98	0.00
R of Ez_total	0.99	-0.01	0.99	-0.02	1.00	-0.02
R of E_total	0.99	0.00	0.99	0.00	0.99	0.00

Table 4-IV. The correlation coefficients between the original Ella model and the chosen tissue-reduced Ella model at 3 T.

Landmark positions	400mm		600mm		800mm	
Correlation coefficient	module	phase	module	phase	module	phase
R of Ex_left_arm	1.00	0.00	1.00	0.03	1.00	0.02
R of Ey_left_arm	1.00	-0.01	1.00	0.02	1.00	0.01
R of Ez_left_arm	1.00	-0.01	1.00	0.00	1.00	0.02
R of E_left_arm	1.00	0.00	1.00	0.00	1.00	0.00
R of Ex_right_arm	1.00	-0.01	1.00	0.03	1.00	0.02
R of Ey_right_arm	1.00	-0.01	0.99	0.02	1.00	0.01
R of Ez_right_arm	1.00	-0.02	1.00	0.01	1.00	0.01
R of E_right_arm	1.00	0.00	1.00	0.00	1.00	0.00
R of Ex_left_tibia	1.00	0.01	1.00	0.00	1.00	0.00
R of Ey_left_tibia	1.00	0.02	0.99	0.01	0.99	0.02
R of Ez_left_tibia	0.99	0.02	0.99	-0.01	0.99	-0.02
R of E_left_tibia	1.00	0.00	1.00	0.00	1.00	0.00
R of Ex_right_tibia	0.99	0.04	1.00	0.04	0.99	-0.01
R of Ey_right_tibia	0.99	0.07	1.00	0.03	1.00	0.00

Table 4-IV. The correlation coefficients between the original Ella model and the chosen tissue-reduced Ella model at 3 T. (continued)

R of Ez_right_tibia	0.99	0.03	0.99	0.02	0.99	-0.03
R of E_right_tibia	0.99	0.00	1.00	0.00	1.00	0.00
R of Ex_hip_femur	0.99	-0.01	0.99	-0.02	0.99	-0.02
R of Ey_hip_femur	0.99	0.00	0.99	-0.01	0.99	-0.02
R of Ez_hip_femur	1.00	-0.04	1.00	-0.04	1.00	-0.03
R of E_hip_femur	1.00	0.00	1.00	0.00	1.00	0.00
R of Ex_body	0.99	-0.02	0.98	0.03	0.98	0.02
R of Ey_body	0.98	-0.02	0.97	0.01	0.98	0.00
R of Ez_body	0.99	-0.02	1.00	-0.02	1.00	-0.02
R of E_body	0.98	0.00	0.99	0.00	0.99	0.00
R of Ex_head	0.99	-0.03	0.97	-0.02	0.97	0.00
R of Ey_head	0.98	0.00	0.98	0.00	0.98	0.00
R of Ez_head	0.99	-0.04	0.97	0.00	0.98	0.03
R of E_head	0.99	0.00	0.98	0.00	0.98	0.00
R of Ex_total	0.99	-0.02	0.99	0.00	0.99	0.00
R of Ey_total	0.99	-0.01	0.99	0.00	0.99	0.00
R of Ez_total	1.00	-0.02	1.00	-0.02	1.00	-0.02
R of E_total	0.99	0.00	0.99	0.00	1.00	0.00

Table 4-V. The correlation coefficients between the original FATS model and the chosen tissue-reduced FATS model at 3 T.

Landmark positions	400mm		600mm		800mm	
Correlation coefficient	module	phase	module	phase	module	phase
R of Ex_left_arm	1.00	0.00	1.00	0.00	1.00	0.01
R of Ey_left_arm	1.00	-0.01	1.00	0.00	1.00	0.00
R of Ez_left_arm	1.00	0.00	1.00	-0.01	1.00	0.00
R of E_left_arm	1.00	0.00	1.00	0.00	1.00	0.00
R of Ex_right_arm	1.00	0.01	1.00	0.00	1.00	0.00
R of Ey_right_arm	1.00	0.00	1.00	-0.01	1.00	0.00
R of Ez_right_arm	1.00	0.00	1.00	-0.01	1.00	0.00
R of E_right_arm	1.00	0.00	1.00	0.00	1.00	0.00
R of Ex_left_tibia	0.99	0.02	1.00	0.00	1.00	0.01
R of Ey_left_tibia	0.99	0.03	1.00	0.01	0.99	0.02
R of Ez_left_tibia	0.99	0.03	0.99	0.02	0.99	0.02
R of E_left_tibia	1.00	0.00	1.00	0.00	1.00	0.00
R of Ex_right_tibia	1.00	0.03	1.00	0.02	0.98	-0.01
R of Ey_right_tibia	0.99	0.03	0.99	0.04	0.99	-0.01
R of Ez_right_tibia	0.99	0.02	0.99	0.02	0.99	0.02
R of E_right_tibia	0.99	0.00	1.00	0.00	0.99	0.00

Table 4-V. The correlation coefficients between the original FATS model and the chosen tissue-reduced FATS model at 3 T. (continued)

R of Ex_hip_femur	1.00	-0.01	1.00	-0.02	1.00	-0.02
R of Ey_hip_femur	1.00	-0.01	1.00	-0.01	1.00	-0.01
R of Ez_hip_femur	1.00	-0.01	1.00	-0.02	1.00	-0.02
R of E_hip_femur	1.00	0.00	1.00	0.00	1.00	0.00
R of Ex_body	0.99	0.00	0.99	-0.02	0.99	-0.01
R of Ey_body	0.99	0.00	0.99	-0.02	0.99	-0.01
R of Ez_body	0.99	-0.01	1.00	-0.02	1.00	-0.02
R of E_body	0.98	0.00	0.99	0.00	0.99	0.00
R of Ex_head	0.97	0.02	0.96	0.08	0.97	0.02
R of Ey_head	0.97	0.02	0.97	0.02	0.98	-0.01
R of Ez_head	0.99	0.01	0.99	0.02	0.99	-0.02
R of E_head	0.98	0.00	0.97	0.00	0.98	0.00
R of Ex_total	0.99	0.00	0.99	-0.02	0.99	-0.02
R of Ey_total	0.99	0.00	0.99	-0.01	0.99	-0.01
R of Ez_total	0.99	0.00	1.00	-0.02	1.00	-0.01
R of E_total	0.99	0.00	0.99	0.00	1.00	0.00

4.3. Tissue-reduced Virtual Family Models' application on RF-induced heating evaluation of passive medical implants at 3 T

4.3.1. Passive device systems and electromagnetic simulation setup

To study the performance of the tissue-reduced virtual family models on the RF-induced heating evaluation of passive device, four representative passive systems which are the same the systems as those used at 1.5 T were implanted in the original human models, tissue-reduced virtual family models and ASTM phantom. These passive device systems are the standalone screw system, the pedicle screw system, the plate and screw system and the stent system. They were implanted at the same positions as those at 1.5 T as shown in Figure 3-2. All the device was set as PEC in the simulations.

Electromagnetic simulations were conducted with SEMCAD X (V14.8 SPEAG) software. The G32 coil was used to model the RF coil with a diameter of 700 mm and a length of 490 mm. The metal shield for this coil has a length of 850 mm. The landmark positions for the human models and ASTM phantom, the materials for ASTM phantom and the positions of the device in ASTM phantom were all set to be the same as those at 1.5 T. The boundary conditions for six directions, the simulation time and the maximum mesh sizes for the human models, ASTM phantom and the passive device systems were all identical to those at 1.5 T. The frequency at 3 T was set to 128 MHz. All the results in ASTM phantom were normalized to a whole-body average SAR of 2 W/kg. And all the results in human models were also normalized to the NORMAL OPERATING MODE.

4.3.2. **Simulated results and discussion**

An E-scaling method was also applied for the ASTM phantom using the incident electric field like 1.5 T. The results of peak SAR_{1g} near the implanted passive device in the original human models and SAR_{1g} near the same locations around the device in the simplified human models and ASTM phantom were extracted for comparison as shown in Figure 4-2. And a σ-scaling using a standard rod made from titanium was also conducted for the values of SAR_{1g} to calibrate the influence of the surrounding tissues' electrical conductivities. The correlation coefficient between the SAR_{1g} of the original human models and the SAR_{1g} of the tissue-reduced human models is as high as 0.98. And the correlation coefficients between the SAR_{1g} of the original human models and the SAR_{1g} of the ASTM phantom are 0.33 without E-scaling and 0.93 with E-scaling. The slopes for the fitting straight line are 1.03 for tissue-reduced virtual family, 0.25 for ASTM phantom without E-scaling and 0.83 for the ASTM phantom with E-scaling. Thus, the peak SAR_{1g} near the device from the tissue-reduced virtual family models is highly correlated to that obtained from the original human body models. While the correlation between the SAR_{1g} from the original human models and the ASTM phantom is relatively lower.

Similar to the results at 1.5 T, the ASTM phantom is conservative in most studied cases. Some exceptions occur, like the outliers in the lower right corner in Figure 4-2. In those cases, the values of SAR_{1g} in original human models are significantly higher than those in the ASTM phantom, which means the ASTM phantom is not conservative. These outliers are the conditions that the device was implanted in the fibula region and the main trunk of the body is outside the coil. That leads to a very high input power for normalization, which leads to a very high incident electric field and very high SAR. When the device is a standalone screw implanted in the pelvic region, the ASTM phantom is also overly conservative like the conditions at 1.5 T. The values of SAR_{1g} in ASTM phantom can be 990.3% higher than those in original human models. From the Figure 4-2, conservative results are not guaranteed for the tissue-reduced human models in many cases, but the tissue-reduced human models yield a highly correlated evaluated SAR_{1g} to that of the original human models.

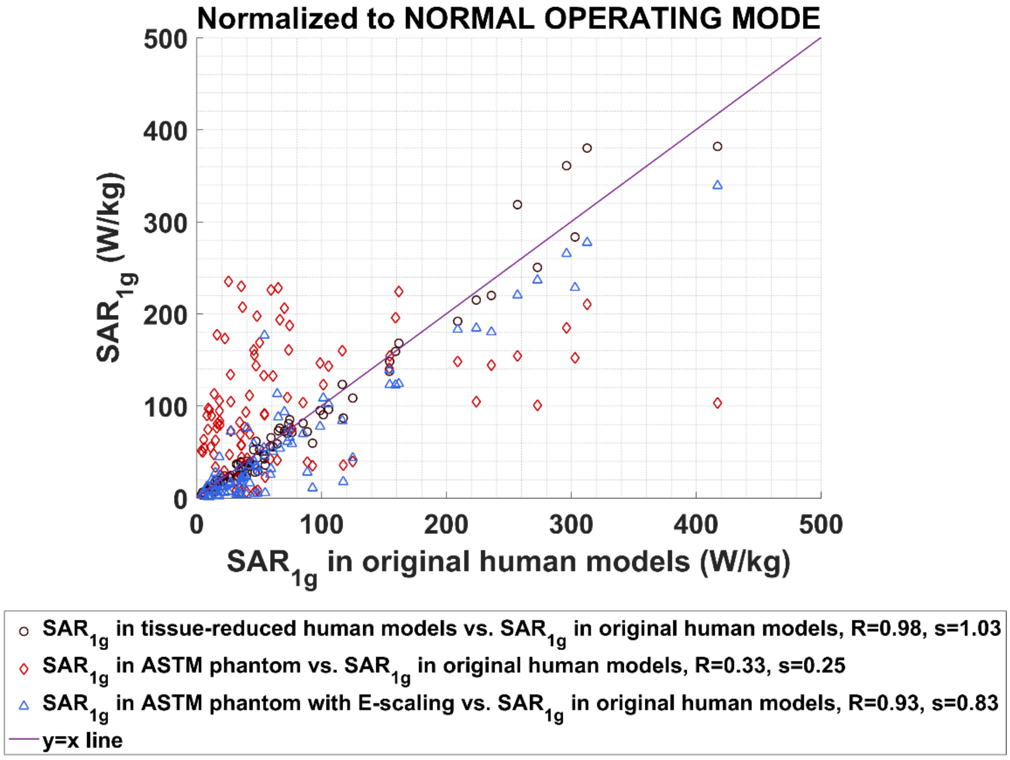

Figure 4-2. Results of the SAR_{1g} for all simulations at the positions of peak SAR_{1g} near the implanted passive device in the original human models at 3T. The R is the correlation coefficient, and the s is the slope of the fitting straight line in the legend.

The comparison of SAR_{1g} in the tissue-reduced human models and in the ASTM phantom with or without E-scaling is shown in Figure 4-3. From this figure, the results are similar to those at 1.5 T. The SAR_{1g} evaluated in ASTM phantom without the E-scaling is more conservative than those in the tissue-reduced human models, excluding the conditions when the device was implanted in the fibula region. The E-scaling may make the SAR_{1g} evaluated in the ASTM phantom less or more conservative depending on the implanted positions of the device.

An uncertainty analysis was also conducted at 3 T as in Appendix IV. The combined uncertainty considering the loading position, grid resolution and tissues' properties was calculated as 4.86% at 3 T.

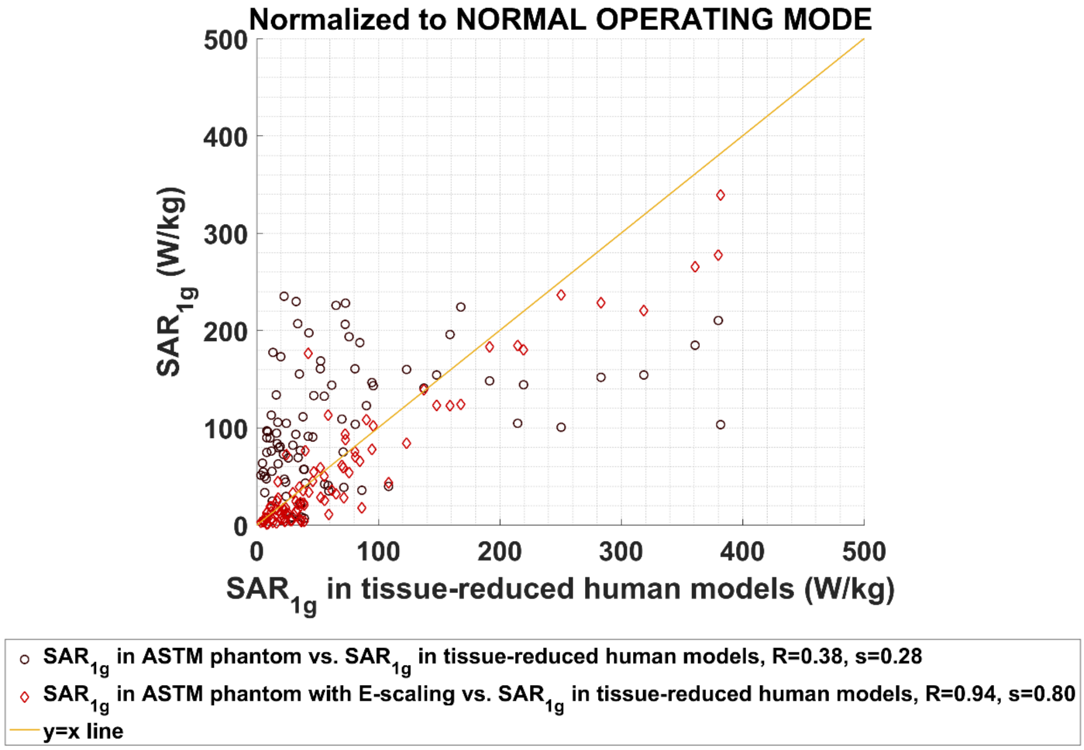

Figure 4-3. Comparison of the SAR_{1g} in tissue-reduced human models and ASTM phantom with or without E-scaling at 3 T. The R is the correlation coefficient, and the s is the slope of the fitting straight line in the legend.

4.4. Conclusions

The Volume-Weighing Tissue-Cluster models with 2 clusters (VWCk2) developed based on the GMM can also be applied at 3 T. These tissue-reduced virtual family models have similar performance at 3 T compared to that at 1.5 T. In detail, the correlation between the electric field in the original human models and the tissue-reduced virtual family models is extremely high (for all calculated correlation coefficients, the modules $\geq$ 0.96 and -0.04 rad $\leq$ the phase $\leq$ 0.1 rad).

And the correlation between SAR_{1g} near the device evaluated in the original human models and tissue-reduced human models is higher than the correlation between that evaluated in the original human models and ASTM phantom. That means the tissue-reduced virtual family models have better performance on accurately predicting the peak SAR_{1g} near the device than that of the ASTM phantom at 3 T. Thus, these results demonstrate the feasibility of using tissue-reduced models for the RF-induced heating testing of implantable medical devices at 1.5 T and 3 T.

Chapter 5. PROGRESS OF 3D PRINTING THE TISSUE-REDUCED HUMAN MODELS FOR EXPERIMENTAL STUDY AND FUTURE WORK

5.1. Introduction

The proposed tissue-reduced human models need to be fabricated to test the RF-induced heating near the device in human models. To achieve that, the 3D printing technique was chosen. Like the ASTM phantom, we first need to print a human-shaped shell. The shell will be used to contain the gelled-saline and other materials. Based on the tissues in each cluster and their parameters (electrical conductivity, relative permittivity and density) of the proposed tissue-reduced human models, the cluster 1 (the main tissues are bone and fat) are planned to be 3D printed. While the cluster 2 (the main tissues are the muscle and skin) will be represented by the gelled-saline. The material's parameters for the 3D printing can be chosen to be as close as possible to those of the cluster 1. And the formulation of the gelled-saline can also be adjusted to make the electrical conductivity and other parameters as close as possible to those of the cluster 2.

This chapter introduces the progress of 3D printing the tissue-reduced human models. The main progress is focused on printing the human-shaped shell for the Duke model. The skin of the Duke human model was used as the model of the human-shaped shell. The main difficulties for printing the human-shaped shell are the limit of the printing size and the strength of the material. In detail, the printing size of the 3D printer is limited (400 mm * 400 mm * 400 mm for the used 3D printer) and the whole human skin is too large to be printed as a whole object. And to be filled with gelled-saline in the future, the strength of the material also needs to be taken into consideration. The skin is very thin (with the thickness around millimeters of magnitude) which leads to the human-shaped shell may be easy to break up with gelled-saline filled. To solve these problems, the human-shaped shell was segmented into several parts to satisfy the size limit of the 3D printer. And a box was added to the skin model to offer extra support for the model to prevent the possible split.

To test the 3D printer, the head's skin was first printed to investigate the function of the printer and the strength of the material. After that, every section of the segmented human-shaped shell with the box was printed. In the future, the tissues inside the shell will be fabricated using 3D printing or gelled-saline.

5.2. 3D printing testing for head’s skin model

To test if the 3D printer can successfully print the human-shaped shell, the head’s skin of the Duke model was printed for reference. The printed head’s skin model was also filled with gelled-saline for accessing the strength of material. The head’s skin model with .stl format was gotten using the Sim4life software package as shown in Figure 5-1A. The head’s skin model in a 3D printer slicer software (Ultimaker Cura 4.12.1) is also shown in Figure 5-1B. The material of the filaments for 3D printing is PLA (Polylactic acid). The printed head’s skin model is shown in Figure 5-2.

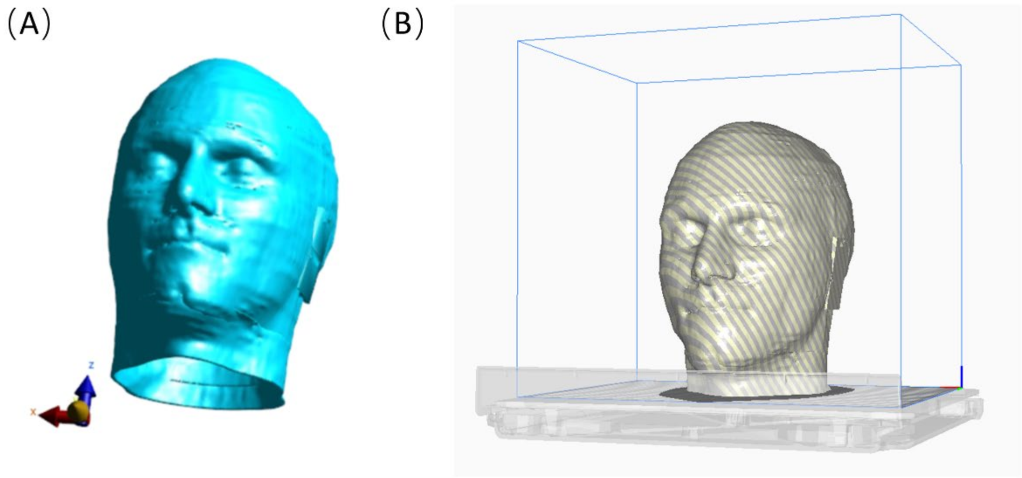

Figure 5-1. A, the head's skin model in the Sim4life software package. B, the head's skin model in a 3D printer slicer software (Ultimaker Cura 4.12.1).

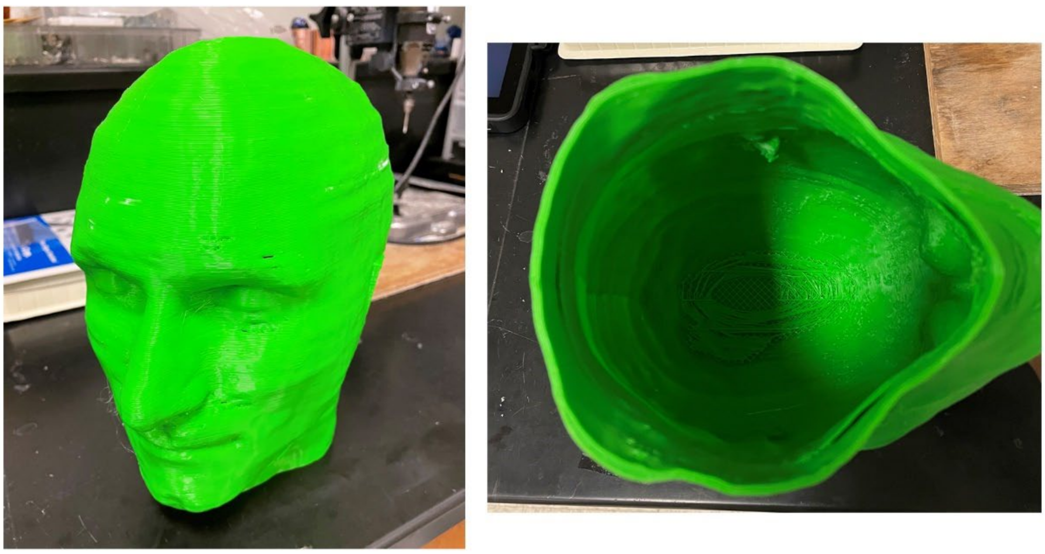

Figure 5-2. The printed head's skin model.

The head's skin model was filled with gelled-saline (the used gelled-saline is the same as that used in ASTM phantom). Although no obvious deformation was observed, a box was added to the whole body's skin model to offer additional support. And another benefit of adding the box is that it will offer a flat surface on the back, making the placement of the human-shaped shell more convenient and stable.

5.3. 3D printing for human-shaped shell

The whole human-shaped shell was segmented into 17 parts to fit the size of the 3D printer. The segments will be stuck together to form a whole human-shaped shell. The details of the segments are shown in Figure 5-3. The segment 7 and segment 8 are two removable pieces which offer a hole to fill the gelled-saline into the shell. A box was added to every segment to offer additional support as shown in Figure 5-3.

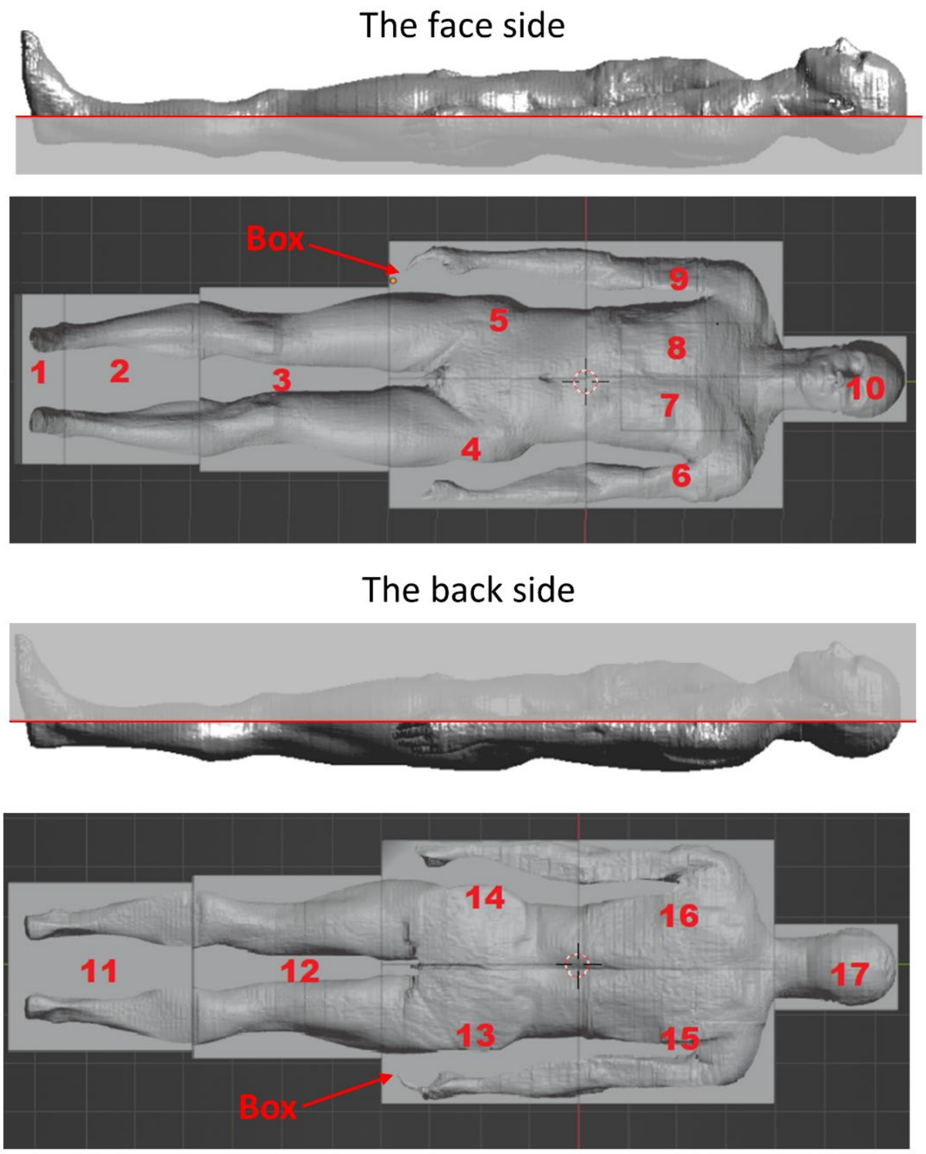

Figure 5-3. The 17 segments of the human-shaped shell.

The boxes consist of air and 5%-7% filled PLA. Considering the PLA has a relative permittivity around 2.72 [58], [59] and density around 1240 kg/m^3 [60], the averaged relative permittivity of the box is from 1.0860 (5% filled) to 1.1204 (7% filled) and the averaged density of the box is from 62.0 kg/m^3 (5% filled) to 86.8 kg/m^3 (7% filled). The electrical conductivities of the air and the PLA are ~ 0 S/m so the box has an electrical conductivity of 0 S/m. To investigate if the added box will influence the electric field distribution inside the shell, electromagnetic simulation was conducted using the SEMCAD software packages. The human skin model with and without a PLA filled box was placed in the G32 coil at three landmark positions as shown in Figure 2-7. The simulation setups were all the same as those in the part 2.1.3. To keep the mesh of the skin model with and without a PLA filled box identical, the skin model without the PLA filled box was simulated as a skin model with an air-filled box. The air-filled box has the same size and positions as the PLA filled box. The correlation coefficients between the electric field inside the skin model with and without PLA filled box were calculated for several body regions as in Figure 2-8. The correlation coefficients for the electric field along the x, y, z direction and the module of the electric field are shown in Table 5-I for the 5% filled PLA box and Table 5-II for the 7% filled PLA box. The real parts and imaginary parts of x, y and z components of the electric field along the z-axis inside the shell at three landmark positions were also extracted for comparison as shown in Figure 5-4, Figure 5-5 and Figure 5-6. From the results of the correlation coefficients and electric field distributions, adding the box will not influence the electric field inside the human-shaped shell. Thus, using the box to offer extra support is a feasible method.

Table 5-I. The correlation coefficients between the electric field inside the skin model with and without the 5% filled PLA box.

Landmark positions	400mm		600mm		800mm	
Correlation coefficient	module	phase	module	phase	module	phase
R of Ex_left_arm	1.00	0.00	1.00	-0.01	1.00	-0.01
R of Ey_left_arm	1.00	0.00	1.00	0.00	1.00	-0.01
R of Ez_left_arm	1.00	-0.01	1.00	-0.02	1.00	-0.02
R of E_left_arm	1.00	0.00	1.00	0.00	1.00	0.00
R of Ex_right_arm	1.00	-0.01	1.00	-0.02	1.00	-0.02
R of Ey_right_arm	1.00	0.00	1.00	0.00	1.00	0.00
R of Ez_right_arm	1.00	-0.01	1.00	-0.02	1.00	-0.02
R of E_right_arm	1.00	0.00	1.00	0.00	1.00	0.00
R of Ex_left_tibia	1.00	-0.03	1.00	-0.05	1.00	-0.06
R of Ey_left_tibia	1.00	-0.05	1.00	-0.06	1.00	-0.06
R of Ez_left_tibia	1.00	-0.05	1.00	-0.03	1.00	-0.04
R of E_left_tibia	1.00	0.00	1.00	0.00	1.00	0.00
R of Ex_right_tibia	1.00	-0.04	1.00	-0.02	1.00	-0.02
R of Ey_right_tibia	1.00	-0.05	1.00	-0.03	1.00	-0.01
R of Ez_right_tibia	1.00	-0.05	1.00	-0.02	1.00	-0.01
R of E_right_tibia	1.00	0.00	1.00	0.00	1.00	0.00
R of Ex_hip_femur	1.00	0.00	1.00	0.00	1.00	-0.01
R of Ey_hip_femur	1.00	0.00	1.00	0.00	1.00	0.00
R of Ez_hip_femur	1.00	-0.01	1.00	0.00	1.00	-0.01
R of E_hip_femur	1.00	0.00	1.00	0.00	1.00	0.00
R of Ex_body	1.00	0.00	1.00	-0.01	1.00	-0.01
R of Ey_body	1.00	0.00	1.00	0.00	1.00	0.00
R of Ez_body	1.00	0.00	1.00	-0.01	1.00	-0.01
R of E_body	1.00	0.00	1.00	0.00	1.00	0.00
R of Ex_head	0.98	0.00	0.99	-0.01	0.98	-0.03
R of Ey_head	0.98	0.01	1.00	0.00	0.99	-0.02
R of Ez_head	1.00	0.00	1.00	-0.01	1.00	-0.01
R of E_head	1.00	0.00	0.99	0.00	1.00	0.00
R of Ex_total	1.00	0.00	1.00	0.00	1.00	-0.01
R of Ey_total	1.00	0.00	1.00	0.00	1.00	0.00
R of Ez_total	1.00	-0.01	1.00	-0.01	1.00	-0.01
R of E_total	1.00	0.00	1.00	0.00	1.00	0.00

Table 5-II. The correlation coefficients between the electric field inside the skin model with and without the 7% filled PLA box.

Landmark positions	400mm		600mm		800mm	
Correlation coefficient	module	phase	module	phase	module	phase
R of Ex_left_arm	1.00	-0.01	1.00	-0.01	1.00	-0.02
R of Ey_left_arm	1.00	-0.01	1.00	-0.01	1.00	-0.01
R of Ez_left_arm	1.00	-0.02	1.00	-0.03	1.00	-0.03
R of E_left_arm	1.00	0.00	1.00	0.00	1.00	0.00
R of Ex_right_arm	1.00	-0.01	1.00	-0.02	1.00	-0.03
R of Ey_right_arm	1.00	0.00	1.00	0.00	1.00	0.00
R of Ez_right_arm	1.00	-0.02	1.00	-0.03	1.00	-0.03
R of E_right_arm	1.00	0.00	1.00	0.00	1.00	0.00
R of Ex_left_tibia	1.00	-0.05	1.00	-0.07	1.00	-0.08
R of Ey_left_tibia	1.00	-0.06	1.00	-0.08	1.00	-0.08
R of Ez_left_tibia	1.00	-0.07	1.00	-0.04	1.00	-0.05
R of E_left_tibia	1.00	0.00	1.00	0.00	1.00	0.00
R of Ex_right_tibia	1.00	-0.06	1.00	-0.02	1.00	-0.02
R of Ey_right_tibia	1.00	-0.06	1.00	-0.04	1.00	-0.02
R of Ez_right_tibia	1.00	-0.07	1.00	-0.02	1.00	-0.02
R of E_right_tibia	1.00	0.00	1.00	0.00	1.00	0.00
R of Ex_hip_femur	1.00	0.00	1.00	0.00	1.00	-0.01
R of Ey_hip_femur	1.00	0.00	1.00	0.00	1.00	0.00
R of Ez_hip_femur	1.00	-0.02	1.00	0.00	1.00	-0.01
R of E_hip_femur	1.00	0.00	1.00	0.00	1.00	0.00
R of Ex_body	1.00	0.00	1.00	-0.01	1.00	-0.02
R of Ey_body	1.00	0.00	1.00	0.00	1.00	0.00
R of Ez_body	1.00	-0.01	1.00	-0.01	1.00	-0.01
R of E_body	1.00	0.00	1.00	0.00	1.00	0.00
R of Ex_head	0.98	0.00	0.99	-0.01	0.98	-0.04
R of Ey_head	0.98	0.01	1.00	0.00	0.99	-0.03
R of Ez_head	1.00	0.00	1.00	-0.01	1.00	-0.02
R of E_head	1.00	0.00	0.99	0.00	1.00	0.00
R of Ex_total	1.00	0.00	1.00	-0.01	1.00	-0.01
R of Ey_total	1.00	0.00	1.00	0.00	1.00	0.00
R of Ez_total	1.00	-0.01	1.00	-0.01	1.00	-0.01
R of E_total	1.00	0.00	1.00	0.00	1.00	0.00

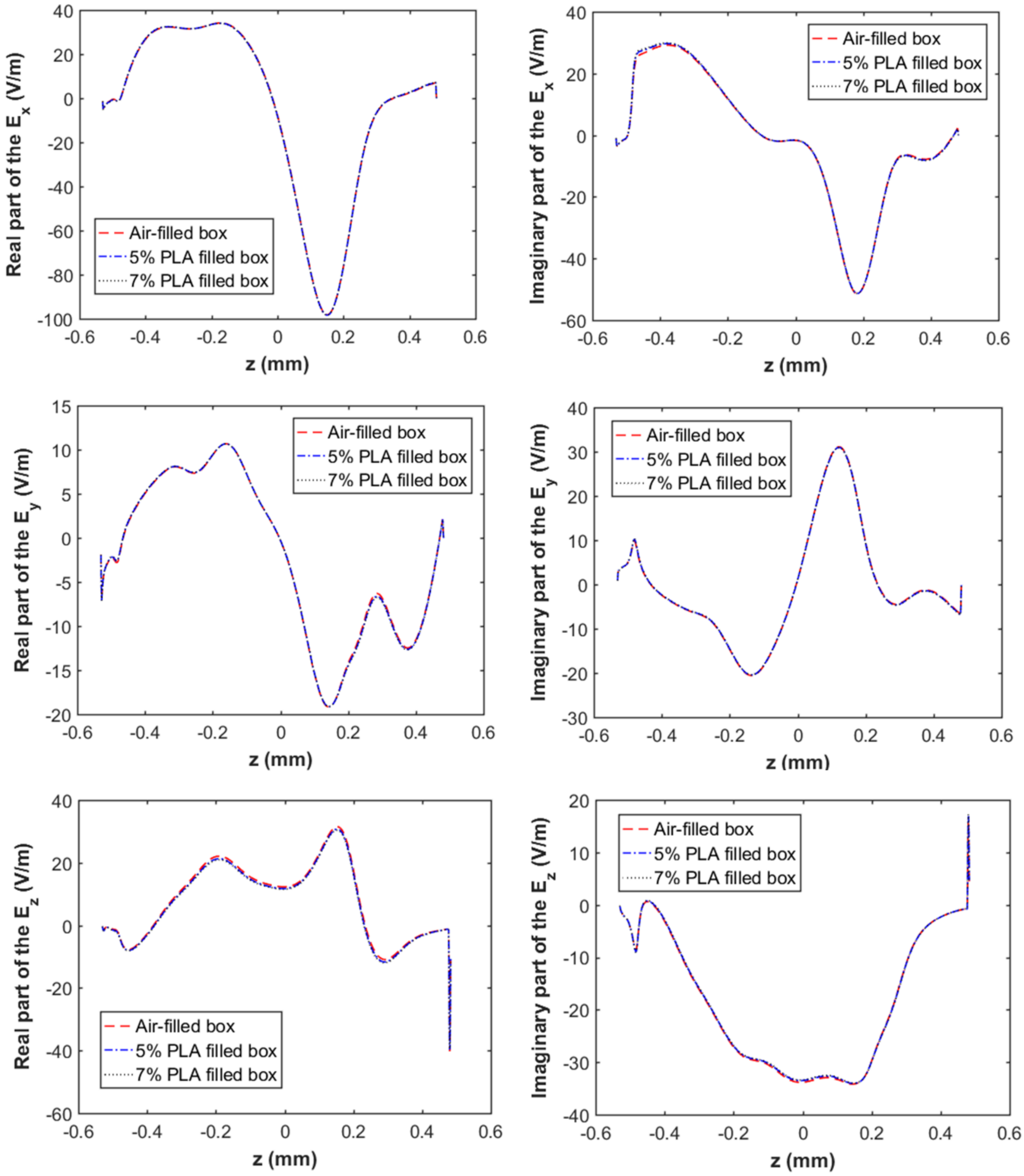

Figure 5-4. The real parts and imaginary parts of *x*, *y* and *z* components of electric field along the z-axis inside the shell at 400 mm landmark position.

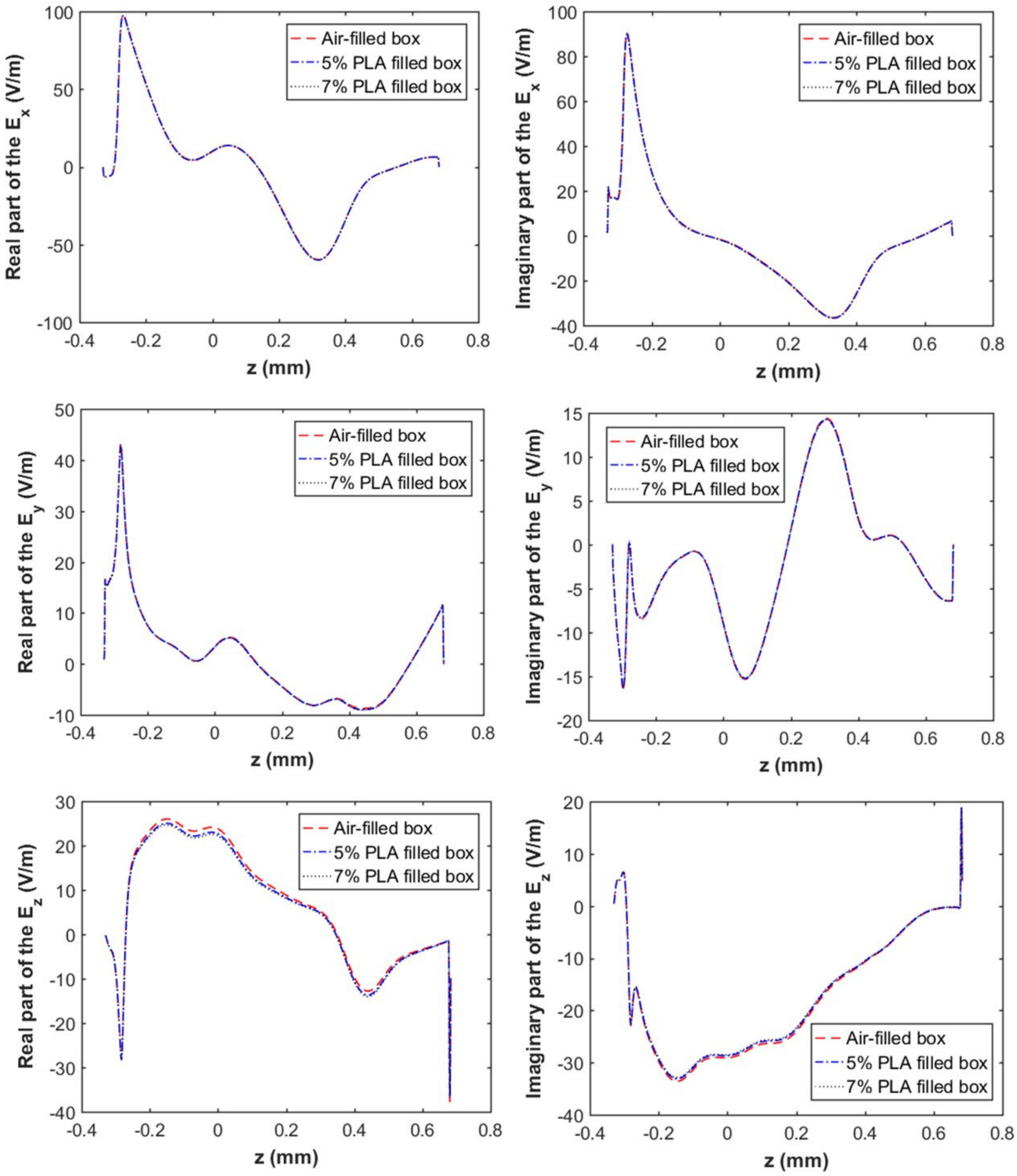

Figure 5-5. The real parts and imaginary parts of *x*, *y* and *z* components of electric field along the z-axis inside the shell at 600 mm landmark position.

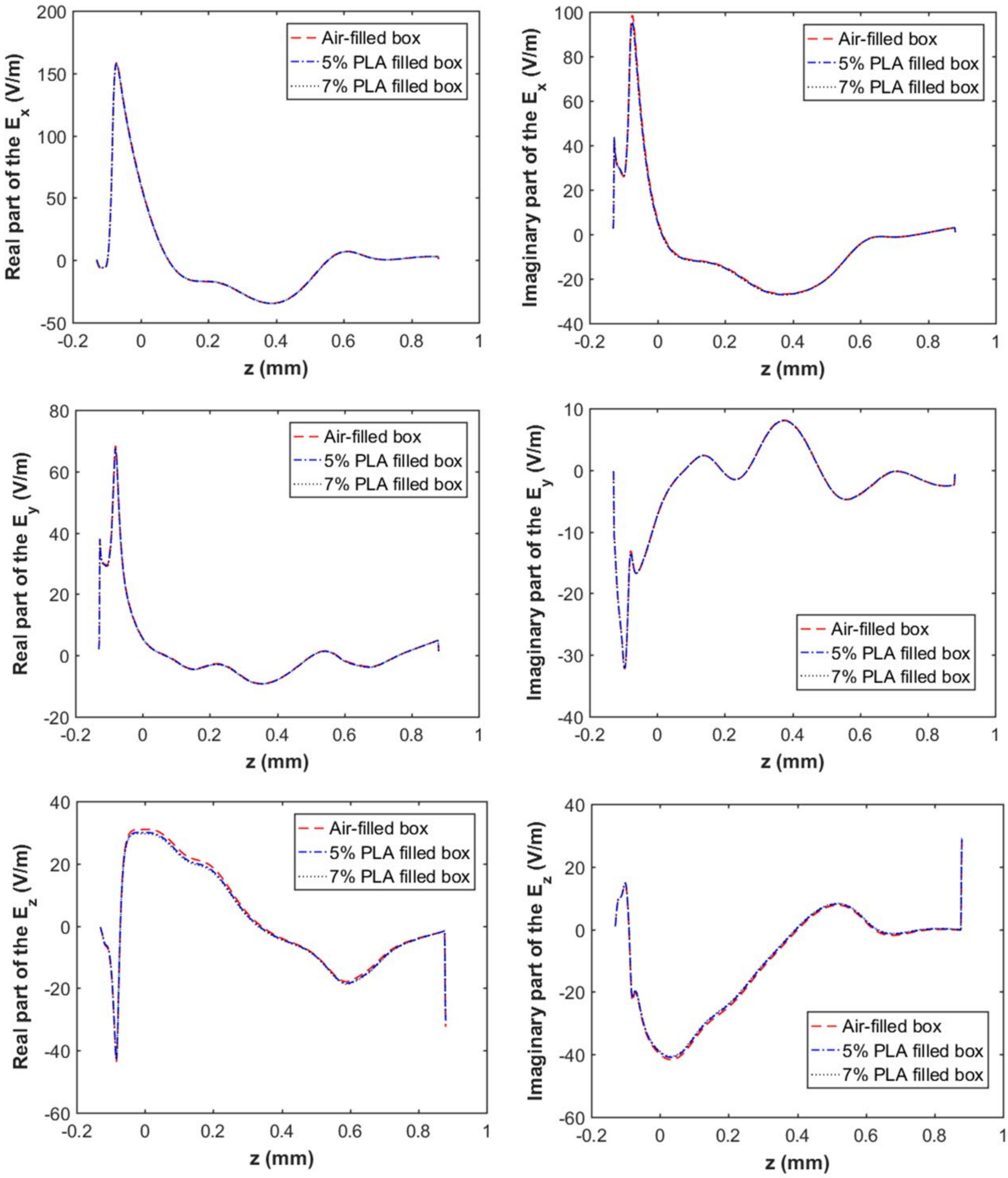

Figure 5-6. The real parts and imaginary parts of *x*, *y* and *z* components of electric field along the z-axis inside the shell at 800 mm landmark position.

5.4. **Future work**

With the 3D printed human-shaped shell for the Duke model, the following steps are to fabricate the tissues inside the shell. Based on the proposed tissue-reduced Duke model, the main tissues in cluster 1 are the bone and fat with electrical conductivity of 0.11 S/m and relative permittivity of 18.38 at 1.5 T. The

3D printing technology could be used to fabricate the tissues in cluster 1. For cluster 2, the main tissues are muscle and skin with electrical conductivity of 0.67 S/m and relative permittivity of 76.58 at 1.5 T. The gelled-saline similar to that used in ASTM phantom but with adjusted formulation could be used to model the tissues in cluster 2. It is easy to adjust the electrical conductivities of the 3D printing materials and gelled-saline by changing the amount of added conductive materials. For the 3D printing materials like PLA and acrylonitrile butadiene styrene (ABS), the electrical conductivity of the PLA can be adjusted from 10^{-12} S/m to 6.27 S/m by changing the filler's concentration, and the materials of filler can be carbon or graphene [61], [62]. The electrical conductivity of the ABS can be adjusted from 0 S/m to around 1 S/m with different percentages of doped carbon fiber [63]. For the gelled-saline, the electrical conductivity can be changed by adjusting the concentration of the NaCl [9], [64]. The electrical conductivity of the gelled-saline used in the ASTM phantom is 0.47 S/m and can be adjusted to as high as 3.2 S/m [9], [64]. However, the adjustment of the relative permittivity is more difficult. In the future, we could try other 3D printing materials to get the possible closest relative permittivity to what we need. Some common 3D printing materials are PLA ($\varepsilon_r \sim 2.72$ S/m), ABS ($\varepsilon_r \sim 2.6$ S/m) and polyethylene terephthalate (PET) ($\varepsilon_r \sim 2.87$ S/m) [65]. Some composite materials like the ABS doped with ferroelectric barium titanate ($BaTiO_3$) micro-particles can have a higher relative permittivity of ~ 11 [66]. The relative permittivity of the gelled-saline in the ASTM phantom could be difficult to adjust, and more electromagnetic simulations would be necessary to investigate influence of the relative permittivity on the incident electric field.

The fabrication of the other two tissue-reduced human models (Ella and FATS) is similar to that of the tissue-reduced Duke model. With the tissue-reduced virtual family human models fabricated, the experimental study inside them can be conducted to test the RF-induced heating near the device. Moreover, the results from the simulation in human models can be validated using the experiments inside the tissue-reduced human models.

REFERENCES

[1] Woods, Terry O. "Standards for medical devices in MRI: present and future." *Journal of Magnetic Resonance Imaging: An Official Journal of the International Society for Magnetic Resonance in Medicine* 26.5 (2007): 1186–1189.

[2] Shellock, Frank G. "Radiofrequency energy-induced heating during MR procedures: a review." *Journal of Magnetic Resonance Imaging* 12.1 (2000): 30–36.

[3] Dempsey, Mary F., and Barrie Condon. "Thermal injuries associated with MRI." *Clinical Radiology* 56.6 (2001): 457–465.

[4] Lukas Winter, Eva Oberacker, Celal Özerdem, Yiyi Ji, Florian von Knobelsdorff-Brenkenhoff, Gerd Weidemann, Bernd Ittermann, Frank Seifert, Thoralf Niendorf. "On the RF heating of coronary stents at 7.0 Tesla MRI." *Magnetic Resonance in Medicine* 74.4 (2015): 999–1010.

[5] Meiqi Xia, Jianfeng Zheng, Rui Yang, Shuo Song, Jian Xu, Qi Liu, Wolfgang Kainz, Stuart A. Long, Ji Chen. "Effects of patient orientations, landmark positions, and device positions on the MRI RF-induced heating for modular external fixation devices." *Magnetic Resonance in Medicine* 85.3 (2021): 1669–1680.

[6] Baker, K. B., Tkach, J. A., Phillips, M. D., Rezai, A. R. "Variability in RF-induced heating of a deep brain stimulation implant across MR systems." *Journal*

of Magnetic Resonance Imaging: An Official Journal of the International Society for Magnetic Resonance in Medicine 24.6 (2006): 1236–1242.

[7] Langman, D. A., Goldberg, I. B., Finn, J. P., Ennis, D. B. "Pacemaker lead tip heating in abandoned and pacemaker-attached leads at 1.5 Tesla MRI." *Journal of Magnetic Resonance Imaging* 33.2 (2011): 426–431.

[8] Roger Luechinger, Volkert A. Zeijlemaker, Erik Morre Pedersen, Peter Mortensen, Erling Falk, Firat Duru, Reto Candinas, Peter Boesiger. "In vivo heating of pacemaker leads during magnetic resonance imaging." *European Heart Journal* 26.4 (2005): 376–383.

[9] ASTM F2182-19e2. Standard test method for measurement of radio frequency induced heating on or near passive implants during magnetic resonance imaging. 2019.

[10] Ran Guo, Jianfeng Zheng, Yu Wang, Qi Zeng, Qingyan Wang, Rui Yang, Wolfgang Kainz, Ji Chen. "Computational and experimental investigation of RF-induced heating for multiple orthopedic implants." *Magnetic Resonance in Medicine* 82.5 (2019): 1848–1858.

[11] Lan, Q., Zheng, J., Chen, J., Zhang, M. "Prediction of MRI RF-induced heating for passive implantable medical devices using convolutional neural network." *2020 IEEE International Symposium on Electromagnetic Compatibility & Signal/Power Integrity (EMCSI)*. IEEE, 2020.

[12] Mattei, E., Calcagnini, G., Censi, F., Triventi, M., Bartolini, P. "Role of the lead structure in MRI-induced heating: In vitro measurements on 30 commercial

pacemaker/defibrillator leads." *Magnetic Resonance in Medicine* 67.4 (2012): 925–935.

[13] Zheng, J., Xia, M., Kainz, W., Chen, J. "Wire-based sternal closure: MRI-related heating at 1.5 T/64 MHz and 3 T/128 MHz based on simulation and experimental phantom study." *Magnetic Resonance in Medicine* 83.3 (2020): 1055–1065.

[14] Andreas Christ, Wolfgang Kainz, Eckhart G Hahn, Katharina Honegger, Marcel Zefferer, Esra Neufeld, Wolfgang Rascher, Rolf Janka, Werner Bautz, Ji Chen, Berthold Kiefer, Peter Schmitt, Hans-Peter Hollenbach, Jianxiang Shen, Michael Oberle, Dominik Szczerba, Anthony Kam, Joshua W Guag and Niels Kuster. "The Virtual Family—development of surface-based anatomical models of two adults and two children for dosimetric simulations." *Physics in Medicine & Biology* 55.2 (2009): N23.

[15] Marie-Christine Gosselin, Esra Neufeld, Heidi Moser, Eveline Huber, Silvia Farcito, Livia Gerber, Maria Jedensjö, Isabel Hilber, Fabienne Di Gennaro, Bryn Lloyd, Emilio Cherubini, Dominik Szczerba, Wolfgang Kainz and Niels Kuster. "Development of a new generation of high-resolution anatomical models for medical device evaluation: the Virtual Population 3.0." *Physics in Medicine & Biology* 59.18 (2014): 5287.

[16] Cabot, Eugenia, Earl Zastrow, and Niels Kuster. "Safety assessment of AIMDs under MRI exposure: Tier3 vs. Tier4 evaluation of local RF-induced heating." *2014 International Symposium on Electromagnetic Compatibility, Tokyo*. IEEE, 2014.

[17] Yang, X., Zheng, J., Wang, Y., Long, S. A., Kainz, W., Chen, J. "Body-loop related MRI radiofrequency-induced heating hazards: Observations, characterizations, and recommendations." *Magnetic Resonance in Medicine* 87.1 (2022): 337–348.

[18] Eugenio Mattei, Michele Triventi, Giovanni Calcagnini, Federica Censi, Wolfgang Kainz, Gonzalo Mendoza, Howard I Bassen and Pietro Bartolini. "Complexity of MRI induced heating on metallic leads: experimental measurements of 374 configurations." *Biomedical Engineering Online* 7.1 (2008): 1–16.

[19] Kangarlu, Allahyar, Frank G. Shellock, and Donald W. Chakeres. "8.0-Tesla human MR system: Temperature changes associated with radiofrequency-induced heating of a head phantom." *Journal of Magnetic Resonance Imaging* 17.2 (2003): 220–226.

[20] Guo, R., Zheng, J., Chen, J., Kainz, W. "RF-induced heating comparison between in-vivo and in-phantom for 1.5 T MRI." *2016 IEEE International Symposium on Electromagnetic Compatibility (EMC)*. IEEE, 2016.

[21] de Buck, M. H., Jezzard, P., Jeong, H., Hess, A. T. "An investigation into the minimum number of tissue groups required for 7T in-silico parallel transmit electromagnetic safety simulations in the human head." *Magnetic Resonance in Medicine* 85.2 (2021): 1114–1122.

[22] Milshteyn, E., Guryev, G., Torrado-Carvajal, A., Adalsteinsson, E., White, J. K., Wald, L. L., Guerin, B. "Individualized SAR calculations using computer vision-

based MR segmentation and a fast electromagnetic solver." *Magnetic Resonance in Medicine* 85.1 (2021): 429–443.

[23] Fujimoto, K., Angelone, L. M., Rajan, S. S., Iacono, M. I. "Simplifying the numerical human model with k-means clustering method." Brain and Human Body Modeling *2020* (2021): 261.

[24] Patel, Eva, and Dharmender Singh Kushwaha. "Clustering cloud workloads: K-means vs gaussian mixture model." *Procedia Computer Science* 171 (2020): 158–167.

[25] Morissette, Laurence, and Sylvain Chartier. "The k-means clustering technique: General considerations and implementation in Mathematica." *Tutorials in Quantitative Methods for Psychology* 9.1 (2013): 15–24.

[26] Reynolds, Douglas A. "Gaussian mixture models." *Encyclopedia of Biometrics* 741.659–663 (2009).

[27] Schwarz, Gideon. "Estimating the dimension of a model." *The Annals of Statistics* (1978): 461–464.

[28] Akaike, Hirotugu. "A new look at the statistical model identification." *IEEE Transactions on Automatic Control* 19.6 (1974): 716–723.

[29] Kodinariya, Trupti M., and Prashant R. Makwana. "Review on determining number of Cluster in K-Means Clustering." *International Journal* 1.6 (2013): 90–95.

[30] International Electrotechnical Commission. "IEC 60601-2-33 Medical electrical equipment-Part 2-33: Particular requirements for the basic safety and essential

performance of magnetic resonance equipment for medical diagnosis." *Int Electrotech Comm* (2015): 1–121.

[31] Weisstein, Eric W. "Statistical correlation". *mathworld.wolfram.com*.

[32] Weisstein, Eric W. "Covariance". *mathworld.wolfram.com*.

[33] Dempsey, Mary F., Barrie Condon, and Donald M. Hadley. "MRI safety review." *Seminars in Ultrasound, CT and MRI*. Vol. 23. No. 5. WB Saunders, 2002.

[34] Li, D., Ji, X., Zheng, J., Pan, C., Chen, J., Kainz, W. "A novel design of implantable esophageal stent to reduce the MRI RF-induced heating." *IEEE Transactions on Electromagnetic Compatibility* 59.3 (2016): 805–812.

[35] Laleh Golestanirad, John Kirsch, Giorgio Bonmassar, Sean Downs, Behzad Elahi, Alastair Martin, Maria-Ida Iacono, Leonardo M. Angelone, Boris Keil, Lawrence L. Wald, Julie Pilitsis. "RF-induced heating in tissue near bilateral DBS implants during MRI at 1.5 T and 3T: The role of surgical lead management." *Neuroimage* 184 (2019): 566–576.

[36] Mattei, E., Calcagnini, G., Censi, F., Triventi, M., Bartolini, P. "Numerical model for estimating RF-induced heating on a pacemaker implant during MRI: experimental validation." *IEEE Transactions on Biomedical Engineering* 57.8 (2010): 2045–2052.

[37] Guo, R., Zheng, J., Xia, M., Jiang, G., Shrivastava, D., Kainz, W., Chen, J. "Evaluation of the RF-induced lead-tip heating of AIMDs using a Volume-Weighed Tissue-Cluster Model for 1.5 T MRI." *2021 43rd Annual*

International Conference of the IEEE Engineering in Medicine & Biology Society (EMBC). IEEE, 2021.

[38] Adair, Eleanor R., and Ronald C. Petersen. "Biological effects of radiofrequency/microwave radiation." *IEEE Transactions on Microwave Theory and Techniques* 50.3 (2002): 953–962.

[39] S. M. Park, J. A. Nyenhuis, C. D. Smith, E. J. Lim, K. S. Foster, K. B. Baker, G. Hrdlicka, A. R. Rezai, P. Ruggieri, A. Sharan, F. G. Shellock, P. H. Stypulkowski, and J. Tkach. "Gelled versus nongelled phantom material for measurement of MRI-induced temperature increases with bioimplants." *IEEE Transactions on Magnetics* 39.5 (2003): 3367–3371.

[40] Bell, David Paul, and Merng Koon Wong. "Syndesmotic screw fixation in Weber C ankle injuries–should the screw be removed before weight bearing?" *Injury* 37.9 (2006): 891–898.

[41] Alonso-Vázquez, A., Lauge-Pedersen, H., Lidgren, L., Taylor, M. "Initial stability of ankle arthrodesis with three-screw fixation. A finite element analysis." *Clinical Biomechanics* 19.7 (2004): 751–759.

[42] Cai, L., Zhang, Y., Chen, C., Lou, Y., Guo, X., Wang, J. "3D printing-based minimally invasive cannulated screw treatment of unstable pelvic fracture." *Journal of Orthopaedic Surgery and Research* 13.1 (2018): 1–7.

[43] ITS.

https://www.its-implant.com/cfiles/dfiles/product_docs/CAS_us.pdf.

February 2018.

[44] Stryker.

http://az621074.vo.msecnd.net/syk-mobile-content-cdn/global-content-system/SYKGCSDOC-2-41897/KSJqkHEzVs1kcVUv5amq7PG1Wbtsjw/VAXST6.pdf. December 2017.

[45] Stryker.

https://az621074.vo.msecnd.net/syk-mobile-content-cdn/global-content-system/SYKGCSDOC-2-42578/lUx2Mo1RWat5IUkZc1CmL9SkGvyd0w/AxSOS-ST-30.pdf. October 2015.

[46] Stryker.

https://www.strykermeded.com/media/2342/variax-2-dist-fib-and-third-tub-plate-optech.pdf. July 2015.

[47] Sales, J. R., Ellis, T. J., Gillard, J., Liu, Q., Chen, J. C., Ham, B., Mayberry, J. C. "Biomechanical testing of a novel, minimally invasive rib fracture plating system." *Journal of Trauma and Acute Care Surgery* 64.5 (2008): 1270–1274.

[48] Depuy Synthes.

http://synthes.vo.llnwd.net/o16/LLNWMB8/US%20Mobile/Synthes%20North%20America/Product%20Support%20Materials/Technique%20Guides/103407661%20Rev%20B.pdf. May 2021.

[49] Orthofix.

https://www.orthofix.com/wp-content/uploads/2019/01/HM-2001.1-Hallmark-OpTech-Update-Rev-AA-US_FNL.pdf. May 2020.

[50] Fujimoto, K., Angelone, L. M., Lucano, E., Rajan, S. S., Iacono, M. I. "Radio-frequency safety assessment of stents in blood vessels during magnetic resonance imaging." *Frontiers in Physiology* (2018): 1439.

[51] Vitek, J. J., Roubin, G. S., Al-Mubarek, N., New, G., Iyer, S. S. "Carotid artery stenting: technical considerations." *American Journal of Neuroradiology* 21.9 (2000): 1736–1743.

[52] Elena Lucano, Micaela Liberti, Gonzalo G. Mendoza, Tom Lloyd, Maria Ida Iacono, Francesca Apollonio, Steve Wedan, Wolfgang Kainz, and Leonardo M. Angelone. "Assessing the electromagnetic fields generated by a radiofrequency MRI body coil at 64 MHz: Defeaturing versus accuracy." *IEEE Transactions on Biomedical Engineering* 63.8 (2015): 1591–1601.

[53] Neufeld, E., Kühn, S., Szekely, G., Kuster, N. "Measurement, simulation and uncertainty assessment of implant heating during MRI." *Physics in Medicine & Biology* 54.13 (2009): 4151.

[54] Jcgm, J. C. G. M. "Evaluation of measurement data—Guide to the expression of uncertainty in measurement." *Int. Organ. Stand. Geneva ISBN* 50 (2008): 134.

[55] Gabriel, Sami, R. W. Lau, and Camelia Gabriel. "The dielectric properties of biological tissues: II. Measurements in the frequency range 10 Hz to 20 GHz." *Physics in Medicine & Biology* 41.11 (1996): 2251.

[56] IT'IS.
https://itis.swiss/virtual-population/tissue-properties/database/density/

[57] International Organization for Standardization. "ISO/TS 10974: Assessment of the safety of magnetic resonance imaging for patients with an active implantable medical device." (2016).

[58] Dichtl, Claudius, Pit Sippel, and Stephan Krohns. "Dielectric properties of 3D printed polylactic acid." *Advances in Materials Science and Engineering* 2017 (2017).

[59] Zhang, S., Arya, R. K., Pandey, S., Vardaxoglou, Y., Whittow, W., Mittra, R. "3D-printed planar graded index lenses." *IET Microwaves, Antennas & Propagation* 10.13 (2016): 1411–1419.

[60] Yang, S. L., Wu, Z. H., Yang, W., Yang, M. B. "Thermal and mechanical properties of chemical crosslinked polylactide (PLA)." *Polymer Testing* 27.8 (2008): 957–963.

[61] Patrizia Lambertia, Giovanni Spinellia, Polina P. Kuzhirb, Liberata Guadagnoc, Carlo Naddeoc, Vittorio Romanoc, Rumania Kotsilkovad, Polya Angelovad, Vlado Georgiev. "Evaluation of thermal and electrical conductivity of carbon-based PLA nanocomposites for 3D printing." *AIP Conference Proceedings*. Vol. 1981. No. 1. AIP Publishing LLC, 2018.

[62] Tirado-Garcia, I., Garcia-Gonzalez, D., Garzon-Hernandez, S., Rusinek, A., Robles, G., Martinez-Tarifa, J. M., Arias, A. "Conductive 3D printed PLA composites: On the interplay of mechanical, electrical and thermal behaviours." *Composite Structures* 265 (2021): 113744.

[63] Shreyas Shah, MD Nahin Islam Shiblee, Julkarnyne M. Habibur Rahman, Samiul Basher, Sajjad Husain Mir, Masaru Kawakami, Hidemitsu Furukawa, Ajit Khosla1. "3D printing of electrically conductive hybrid organic–inorganic composite materials." *Microsystem Technologies* 24.10 (2018): 4341–4345.

[64] Langman, D. A., Goldberg, I. B., Judy, J., Paul Finn, J., Ennis, D. B. "The dependence of radiofrequency induced pacemaker lead tip heating on the electrical conductivity of the medium at the lead tip." *Magnetic Resonance in Medicine* 68.2 (2012): 606–613.

[65] Zechmeister, Jaroslav, and Jaroslav Lacik. "Complex relative permittivity measurement of selected 3D-printed materials up to 10 GHz." *2019 Conference on Microwave Techniques (COMITE)*. IEEE, 2019.

[66] Wu, Yingwei, Dmitry Isakov, and Patrick S. Grant. "Fabrication of composite filaments with high dielectric permittivity for fused deposition 3D printing." *Materials* 10.10 (2017): 1218.

A. APPENDIX I: CORRELATION ANALYSIS BETWEEN THE ELECTRIC FIELD OF THE ORIGINAL AND SIMPLIFIED HUMAN MODELS AT 1.5 T

A correlation analysis was conducted between the original human models and simplified human models. The correlation coefficients were calculated for the electric field along the x, y and z direction and the module of the electric field in the human body regions as in Figure 2-8. The correlation coefficients for the Duke model with the three cluster method, different number of clusters (k) and different landmark positions are shown in Table A-I to Table A-III. The results of the Ella model and FATS models are shown in Table A-IV to Table A-VI and Table A-VII to Table A-IX, respectively.

Table A-I. Correlation coefficients for the Duke model at 400 mm landmark.

landmark at 400 mm								
Cluster method 1	k=1		k=2		k=3		k=8	
Correlation coefficient	module	phase	module	phase	module	phase	module	phase
R of Ex_left_arm	0.96	-0.08	0.97	-0.09	0.99	-0.04	1.00	0.00
R of Ey_left_arm	0.93	-0.01	0.95	-0.03	0.99	-0.02	0.99	0.01
R of Ez_left_arm	0.94	-0.09	0.96	-0.12	0.99	-0.07	1.00	0.00
R of E_left_arm	0.94	0.00	0.96	0.00	0.99	0.00	1.00	0.00
R of Ex_right_arm	0.94	-0.06	0.97	-0.17	0.99	-0.11	1.00	0.02
R of Ey_right_arm	0.92	-0.07	0.95	-0.11	0.99	-0.07	0.99	0.01
R of Ez_right_arm	0.91	-0.07	0.95	-0.11	0.99	-0.05	1.00	0.00
R of E_right_arm	0.86	0.00	0.93	0.00	0.99	0.00	0.99	0.00
R of Ex_left_tibia	0.96	-0.08	0.97	-0.09	0.99	-0.04	0.99	-0.01
R of Ey_left_tibia	0.89	-0.02	0.91	-0.01	0.98	0.01	0.99	0.01
R of Ez_left_tibia	0.50	-0.02	0.82	-0.21	0.99	-0.04	0.98	0.09
R of E_left_tibia	0.80	0.00	0.88	0.00	0.99	0.00	0.99	0.00
R of Ex_right_tibia	0.94	0.17	0.96	0.17	0.99	0.04	0.99	0.04
R of Ey_right_tibia	0.90	0.09	0.94	0.09	0.99	0.05	0.99	0.05
R of Ez_right_tibia	0.58	0.14	0.88	0.13	0.99	0.17	0.98	0.11
R of E_right_tibia	0.76	0.00	0.92	0.00	0.99	0.00	0.99	0.00
R of Ex_hip_femur	0.90	-0.06	0.92	-0.13	0.99	-0.09	0.99	0.02
R of Ey_hip_femur	0.93	0.00	0.95	-0.02	0.99	-0.01	0.99	0.02

Table A-I. Correlation coefficients for the Duke model at 400 mm landmark. (continued)

R of Ez_hip_femur	0.93	-0.28	0.95	-0.33	0.99	-0.17	0.99	-0.01
R of E_hip_femur	0.93	0.00	0.95	0.00	0.99	0.00	0.99	0.00
R of Ex_body	0.90	-0.20	0.93	-0.27	0.98	-0.17	0.99	-0.01
R of Ey_body	0.83	-0.13	0.89	-0.17	0.98	-0.11	0.99	0.01
R of Ez_body	0.97	-0.24	0.98	-0.28	0.99	-0.18	1.00	-0.02
R of E_body	0.84	0.00	0.90	0.00	0.98	0.00	0.99	0.00
R of Ex_head	0.93	-0.02	0.94	-0.04	0.98	-0.03	0.99	0.01
R of Ey_head	0.94	0.01	0.95	0.02	0.99	0.01	0.99	0.01
R of Ez_head	0.96	-0.08	0.97	-0.09	0.99	-0.06	0.99	0.01
R of E_head	0.95	0.00	0.96	0.00	0.99	0.00	0.99	0.00
R of Ex_total	0.92	-0.11	0.93	-0.16	0.98	-0.11	0.99	0.00
R of Ey_total	0.91	-0.05	0.93	-0.07	0.98	-0.04	0.99	0.01
R of Ez_total	0.96	-0.20	0.97	-0.23	0.99	-0.15	1.00	-0.02
R of E_total	0.94	0.00	0.96	0.00	0.99	0.00	1.00	0.00
Cluster method 2	k=1		k=2		k=3		k=8	
Correlation coefficient	module	phase	module	phase	module	phase	module	phase
R of Ex_left_arm	0.97	-0.04	0.98	-0.02	1.00	0.00	1.00	0.00
R of Ey_left_arm	0.93	0.01	0.97	0.01	1.00	0.00	1.00	0.00
R of Ez_left_arm	0.94	-0.03	0.98	-0.02	1.00	-0.01	1.00	0.00
R of E_left_arm	0.94	0.00	0.98	0.00	1.00	0.00	1.00	0.00
R of Ex_right_arm	0.94	0.05	0.98	-0.03	1.00	-0.01	1.00	0.00
R of Ey_right_arm	0.92	0.00	0.97	-0.01	1.00	-0.01	1.00	0.00
R of Ez_right_arm	0.92	-0.02	0.98	-0.03	1.00	-0.01	1.00	0.00
R of E_right_arm	0.87	0.00	0.96	0.00	1.00	0.00	1.00	0.00
R of Ex_left_tibia	0.97	-0.10	0.98	-0.06	1.00	-0.02	1.00	0.01
R of Ey_left_tibia	0.90	-0.07	0.96	-0.02	1.00	-0.02	1.00	0.02
R of Ez_left_tibia	0.53	0.00	0.91	-0.12	0.99	-0.02	0.99	0.03
R of E_left_tibia	0.81	0.00	0.94	0.00	1.00	0.00	1.00	0.00
R of Ex_right_tibia	0.94	0.10	0.97	0.04	1.00	-0.04	1.00	-0.01
R of Ey_right_tibia	0.91	0.04	0.97	0.02	0.99	-0.04	0.99	0.01
R of Ez_right_tibia	0.58	0.06	0.93	0.01	0.99	-0.02	0.99	0.02
R of E_right_tibia	0.77	0.00	0.95	0.00	1.00	0.00	1.00	0.00
R of Ex_hip_femur	0.92	0.01	0.96	-0.05	1.00	-0.01	1.00	0.00
R of Ey_hip_femur	0.94	0.02	0.97	0.01	1.00	0.00	1.00	0.00
R of Ez_hip_femur	0.94	-0.10	0.97	-0.10	1.00	0.00	1.00	0.01
R of E_hip_femur	0.95	0.00	0.97	0.00	1.00	0.00	1.00	0.00
R of Ex_body	0.91	-0.04	0.96	-0.04	0.99	-0.04	1.00	0.00
R of Ey_body	0.85	-0.03	0.92	-0.02	0.99	-0.01	1.00	0.00
R of Ez_body	0.97	-0.06	0.98	-0.02	1.00	-0.02	1.00	0.01
R of E_body	0.85	0.00	0.92	0.00	0.99	0.00	0.99	0.00
R of Ex_head	0.94	0.00	0.96	0.00	0.99	-0.01	1.00	0.00

Table A-I. Correlation coefficients for the Duke model at 400 mm landmark. (continued)

R of Ey_head	0.94	0.01	0.96	0.03	0.99	0.00	1.00	0.00
R of Ez_head	0.96	0.00	0.97	0.00	0.99	0.00	1.00	0.00
R of E_head	0.95	0.00	0.96	0.00	0.99	0.00	1.00	0.00
R of Ex_total	0.94	-0.02	0.97	-0.03	0.99	-0.02	1.00	0.00
R of Ey_total	0.92	-0.01	0.96	0.00	0.99	-0.01	1.00	0.00
R of Ez_total	0.97	-0.05	0.98	-0.02	1.00	-0.02	1.00	0.00
R of E_total	0.95	0.00	0.97	0.00	1.00	0.00	1.00	0.00
Cluster method 3	k=1		k=2		k=3		k=8	
Correlation coefficient	module	phase	module	phase	module	phase	module	phase
R of Ex_left_arm	0.97	-0.04	1.00	-0.02	1.00	-0.02	1.00	0.00
R of Ey_left_arm	0.93	0.01	0.99	0.00	0.99	0.00	1.00	0.00
R of Ez_left_arm	0.94	-0.03	1.00	-0.01	1.00	-0.01	1.00	0.00
R of E_left_arm	0.94	0.00	1.00	0.00	1.00	0.00	1.00	0.00
R of Ex_right_arm	0.94	0.05	1.00	-0.01	1.00	-0.02	1.00	0.00
R of Ey_right_arm	0.92	0.00	0.99	0.01	0.99	0.00	1.00	0.00
R of Ez_right_arm	0.92	-0.02	0.99	0.01	0.99	0.00	1.00	0.00
R of E_right_arm	0.87	0.00	0.99	0.00	0.99	0.00	1.00	0.00
R of Ex_left_tibia	0.97	-0.10	0.99	-0.05	0.99	-0.06	1.00	-0.01
R of Ey_left_tibia	0.90	-0.07	0.98	-0.02	0.98	-0.03	1.00	0.00
R of Ez_left_tibia	0.53	0.00	0.96	0.10	0.97	0.05	0.99	0.00
R of E_left_tibia	0.81	0.00	0.98	0.00	0.98	0.00	1.00	0.00
R of Ex_right_tibia	0.94	0.10	0.99	0.04	0.99	0.01	1.00	0.00
R of Ey_right_tibia	0.91	0.04	0.99	0.03	0.98	0.00	1.00	0.00
R of Ez_right_tibia	0.58	0.06	0.97	0.16	0.98	0.10	0.99	0.01
R of E_right_tibia	0.77	0.00	0.98	0.00	0.98	0.00	1.00	0.00
R of Ex_hip_femur	0.92	0.01	0.99	-0.02	0.99	-0.02	1.00	-0.01
R of Ey_hip_femur	0.94	0.02	0.99	0.00	0.99	0.00	1.00	-0.01
R of Ez_hip_femur	0.94	-0.10	0.99	-0.05	0.99	-0.05	1.00	0.00
R of E_hip_femur	0.95	0.00	0.99	0.00	0.99	0.00	1.00	0.00
R of Ex_body	0.91	-0.04	0.98	0.01	0.98	0.00	1.00	0.00
R of Ey_body	0.85	-0.03	0.97	0.01	0.97	0.00	1.00	0.00
R of Ez_body	0.97	-0.06	0.99	0.00	0.99	0.00	1.00	0.01
R of E_body	0.85	0.00	0.96	0.00	0.96	0.00	1.00	0.00
R of Ex_head	0.94	0.00	0.99	0.00	0.99	0.00	0.99	0.00
R of Ey_head	0.94	0.01	0.99	0.00	0.99	0.00	0.99	0.00
R of Ez_head	0.96	0.00	0.99	-0.02	0.99	-0.01	0.99	-0.01
R of E_head	0.95	0.00	0.99	0.00	0.99	0.00	0.99	0.00
R of Ex_total	0.94	-0.02	0.99	0.00	0.99	-0.01	1.00	0.00
R of Ey_total	0.92	-0.01	0.98	0.00	0.98	0.00	1.00	0.00
R of Ez_total	0.97	-0.05	0.99	0.00	0.99	0.00	1.00	0.01
R of E_total	0.95	0.00	0.99	0.00	0.99	0.00	1.00	0.00

Table A-II. Correlation coefficients for the Duke model at 600 mm landmark.

landmark at 600 mm								
Cluster method 1	k=1		k=2		k=3		k=8	
Correlation coefficient	module	phase	module	phase	module	phase	module	phase
R of Ex_left_arm	0.97	0.01	0.98	0.02	1.00	0.01	1.00	0.01
R of Ey_left_arm	0.98	0.02	0.98	0.02	1.00	0.01	1.00	0.01
R of Ez_left_arm	0.95	-0.01	0.97	0.01	0.99	0.02	1.00	0.00
R of E_left_arm	0.98	0.00	0.99	0.00	1.00	0.00	1.00	0.00
R of Ex_right_arm	0.87	0.05	0.92	0.00	0.99	0.03	0.99	0.03
R of Ey_right_arm	0.92	0.02	0.95	0.00	0.99	0.01	0.99	0.02
R of Ez_right_arm	0.92	-0.02	0.95	-0.02	0.99	0.02	0.99	0.00
R of E_right_arm	0.87	0.00	0.93	0.00	0.99	0.00	0.99	0.00
R of Ex_left_tibia	0.91	-0.07	0.94	-0.06	0.99	-0.01	0.99	0.00
R of Ey_left_tibia	0.81	0.02	0.86	-0.02	0.97	0.01	0.98	0.04
R of Ez_left_tibia	0.49	-0.05	0.84	-0.09	0.98	0.06	0.98	0.10
R of E_left_tibia	0.65	0.00	0.82	0.00	0.99	0.00	0.98	0.00
R of Ex_right_tibia	0.99	-0.06	0.99	-0.15	1.00	-0.14	1.00	0.01
R of Ey_right_tibia	0.98	-0.04	0.98	-0.09	1.00	-0.08	1.00	0.01
R of Ez_right_tibia	0.59	0.05	0.85	-0.09	0.99	-0.05	0.98	0.10
R of E_right_tibia	0.94	0.00	0.97	0.00	1.00	0.00	1.00	0.00
R of Ex_hip_femur	0.90	-0.11	0.92	-0.19	0.99	-0.13	0.99	0.02
R of Ey_hip_femur	0.92	-0.02	0.94	-0.05	0.99	-0.03	0.99	0.01
R of Ez_hip_femur	0.96	-0.26	0.97	-0.31	0.99	-0.16	1.00	-0.01
R of E_hip_femur	0.93	0.00	0.95	0.00	0.99	0.00	0.99	0.00
R of Ex_body	0.85	-0.10	0.89	-0.14	0.97	-0.10	0.99	0.00
R of Ey_body	0.85	-0.03	0.90	-0.06	0.98	-0.04	0.99	0.02
R of Ez_body	0.97	-0.24	0.98	-0.27	0.99	-0.17	1.00	-0.01
R of E_body	0.86	0.00	0.90	0.00	0.98	0.00	0.99	0.00
R of Ex_head	0.91	-0.04	0.92	-0.08	0.97	-0.07	0.99	0.01
R of Ey_head	0.93	0.03	0.94	0.04	0.98	0.02	0.99	0.02
R of Ez_head	0.94	-0.04	0.95	-0.07	0.98	-0.06	0.99	0.02
R of E_head	0.94	0.00	0.95	0.00	0.98	0.00	0.99	0.00
R of Ex_total	0.90	-0.09	0.92	-0.14	0.98	-0.09	0.99	0.01
R of Ey_total	0.91	-0.02	0.94	-0.04	0.99	-0.02	0.99	0.01
R of Ez_total	0.96	-0.19	0.97	-0.22	0.99	-0.12	1.00	-0.01
R of E_total	0.93	0.00	0.95	0.00	0.99	0.00	0.99	0.00
Cluster method 2	k=1		k=2		k=3		k=8	
Correlation coefficient	module	phase	module	phase	module	phase	module	phase
R of Ex_left_arm	0.97	0.01	0.99	0.02	1.00	0.00	1.00	0.00
R of Ey_left_arm	0.98	0.01	0.99	0.02	1.00	0.00	1.00	0.00
R of Ez_left_arm	0.95	-0.03	0.98	0.00	1.00	0.00	1.00	0.00
R of E_left_arm	0.98	0.00	0.99	0.00	1.00	0.00	1.00	0.00

Table A-II. Correlation coefficients for the Duke model at 600 mm landmark. (continued)

R of Ex_right_arm	0.88	0.06	0.95	0.01	1.00	0.00	1.00	-0.01
R of Ey_right_arm	0.92	0.03	0.97	0.01	1.00	0.00	1.00	0.00
R of Ez_right_arm	0.92	-0.03	0.97	-0.02	1.00	0.00	1.00	-0.01
R of E_right_arm	0.87	0.00	0.95	0.00	1.00	0.00	1.00	0.00
R of Ex_left_tibia	0.92	-0.10	0.96	-0.06	0.99	-0.02	0.99	0.00
R of Ey_left_tibia	0.82	0.01	0.93	-0.03	0.99	-0.01	0.99	0.00
R of Ez_left_tibia	0.51	-0.07	0.91	-0.08	0.99	0.00	0.99	0.01
R of E_left_tibia	0.66	0.00	0.92	0.00	0.99	0.00	0.99	0.00
R of Ex_right_tibia	0.99	0.04	0.99	-0.02	1.00	-0.02	1.00	0.00
R of Ey_right_tibia	0.98	0.02	0.99	-0.01	1.00	-0.02	1.00	0.00
R of Ez_right_tibia	0.59	0.11	0.92	-0.02	0.99	-0.04	0.99	0.02
R of E_right_tibia	0.94	0.00	0.98	0.00	1.00	0.00	1.00	0.00
R of Ex_hip_femur	0.91	-0.01	0.95	-0.06	1.00	-0.01	1.00	0.00
R of Ey_hip_femur	0.92	0.01	0.96	-0.01	1.00	0.00	1.00	0.00
R of Ez_hip_femur	0.96	-0.09	0.98	-0.08	1.00	-0.01	1.00	0.01
R of E_hip_femur	0.94	0.00	0.97	0.00	1.00	0.00	1.00	0.00
R of Ex_body	0.88	-0.01	0.93	0.00	0.99	-0.03	1.00	0.00
R of Ey_body	0.86	0.00	0.93	0.00	0.99	0.00	1.00	0.00
R of Ez_body	0.97	-0.05	0.98	-0.02	1.00	-0.01	1.00	0.01
R of E_body	0.87	0.00	0.93	0.00	0.99	0.00	1.00	0.00
R of Ex_head	0.93	-0.01	0.96	-0.03	0.99	-0.04	1.00	0.00
R of Ey_head	0.93	0.02	0.96	0.03	0.99	-0.01	1.00	0.01
R of Ez_head	0.96	0.02	0.97	-0.01	0.99	-0.02	1.00	0.01
R of E_head	0.95	0.00	0.97	0.00	1.00	0.00	1.00	0.00
R of Ex_total	0.93	-0.01	0.96	-0.03	1.00	-0.02	1.00	0.00
R of Ey_total	0.92	0.00	0.96	0.00	1.00	0.00	1.00	0.00
R of Ez_total	0.97	-0.05	0.98	-0.03	1.00	0.00	1.00	0.01
R of E_total	0.94	0.00	0.97	0.00	1.00	0.00	1.00	0.00
Cluster method 3	k=1		k=2		k=3		k=8	
Correlation coefficient	module	phase	module	phase	module	phase	module	phase
R of Ex_left_arm	0.97	0.01	1.00	0.00	1.00	0.00	1.00	0.00
R of Ey_left_arm	0.98	0.01	1.00	0.00	1.00	0.00	1.00	0.00
R of Ez_left_arm	0.95	-0.03	1.00	0.00	1.00	0.00	1.00	0.00
R of E_left_arm	0.98	0.00	1.00	0.00	1.00	0.00	1.00	0.00
R of Ex_right_arm	0.88	0.06	0.99	0.03	0.99	0.03	1.00	-0.01
R of Ey_right_arm	0.92	0.03	0.99	0.02	0.99	0.01	1.00	0.00
R of Ez_right_arm	0.92	-0.03	0.99	0.01	0.99	0.01	1.00	0.00
R of E_right_arm	0.87	0.00	0.99	0.00	0.99	0.00	1.00	0.00
R of Ex_left_tibia	0.92	-0.10	0.98	-0.02	0.99	-0.04	1.00	0.00
R of Ey_left_tibia	0.82	0.01	0.98	0.05	0.98	0.03	0.99	0.01
R of Ez_left_tibia	0.51	-0.07	0.97	0.14	0.97	0.08	0.99	0.01

Table A-II. Correlation coefficients for the Duke model at 600 mm landmark. (continued)

R of E_left_tibia	0.66	0.00	0.97	0.00	0.97	0.00	1.00	0.00
R of Ex_right_tibia	0.99	0.04	1.00	0.01	1.00	-0.01	1.00	0.00
R of Ey_right_tibia	0.98	0.02	1.00	0.00	1.00	-0.02	1.00	0.00
R of Ez_right_tibia	0.59	0.11	0.96	0.11	0.97	0.05	0.99	-0.01
R of E_right_tibia	0.94	0.00	0.99	0.00	0.99	0.00	1.00	0.00
R of Ex_hip_femur	0.91	-0.01	0.99	-0.01	0.99	-0.02	1.00	-0.01
R of Ey_hip_femur	0.92	0.01	0.99	0.00	0.99	-0.01	1.00	-0.01
R of Ez_hip_femur	0.96	-0.09	1.00	-0.04	1.00	-0.04	1.00	0.00
R of E_hip_femur	0.94	0.00	0.99	0.00	0.99	0.00	1.00	0.00
R of Ex_body	0.88	-0.01	0.97	0.04	0.97	0.03	1.00	0.01
R of Ey_body	0.86	0.00	0.97	0.01	0.97	0.01	1.00	0.00
R of Ez_body	0.97	-0.05	0.99	-0.01	0.99	-0.01	1.00	0.01
R of E_body	0.87	0.00	0.97	0.00	0.97	0.00	1.00	0.00
R of Ex_head	0.93	-0.01	0.99	-0.01	0.99	-0.01	0.99	0.00
R of Ey_head	0.93	0.02	0.99	0.00	0.99	0.00	0.99	0.00
R of Ez_head	0.96	0.02	0.99	-0.01	0.99	-0.01	0.99	0.00
R of E_head	0.95	0.00	0.99	0.00	0.99	0.00	0.99	0.00
R of Ex_total	0.93	-0.01	0.98	0.00	0.99	0.00	1.00	0.00
R of Ey_total	0.92	0.00	0.99	0.00	0.99	0.00	1.00	0.00
R of Ez_total	0.97	-0.05	0.99	-0.01	0.99	-0.01	1.00	0.00
R of E_total	0.94	0.00	0.99	0.00	0.99	0.00	1.00	0.00

Table A-III. Correlation coefficients for the Duke model at 800 mm landmark.

landmark at 800 mm								
Cluster method 1	k=1		k=2		k=3		k=8	
Correlation coefficient	module	phase	module	phase	module	phase	module	phase
R of Ex_left_arm	0.97	0.02	0.98	0.02	1.00	0.02	1.00	0.01
R of Ey_left_arm	0.98	0.02	0.99	0.02	1.00	0.02	1.00	0.01
R of Ez_left_arm	0.96	0.02	0.98	0.08	1.00	0.07	1.00	0.00
R of E_left_arm	0.98	0.00	0.99	0.00	1.00	0.00	1.00	0.00
R of Ex_right_arm	0.86	0.10	0.92	0.13	0.99	0.13	0.99	0.03
R of Ey_right_arm	0.90	0.01	0.94	-0.02	0.99	0.01	0.99	0.02
R of Ez_right_arm	0.92	0.01	0.96	0.05	0.99	0.07	0.99	0.00
R of E_right_arm	0.89	0.00	0.94	0.00	0.99	0.00	0.99	0.00
R of Ex_left_tibia	0.92	0.00	0.94	0.03	0.99	0.04	0.99	0.01
R of Ey_left_tibia	0.86	0.04	0.90	0.02	0.98	0.03	0.99	0.04
R of Ez_left_tibia	0.49	-0.05	0.85	-0.02	0.98	0.10	0.98	0.10
R of E_left_tibia	0.68	0.00	0.86	0.00	0.99	0.00	0.99	0.00
R of Ex_right_tibia	0.98	-0.07	0.99	-0.14	1.00	-0.12	1.00	0.00
R of Ey_right_tibia	0.98	-0.03	0.99	-0.06	1.00	-0.06	1.00	0.00
R of Ez_right_tibia	0.59	-0.05	0.86	-0.12	0.98	-0.04	0.98	0.08

Table A-III. Correlation coefficients for the Duke model at 800 mm landmark. (continued)

R of E_right_tibia	0.95	0.00	0.97	0.00	1.00	0.00	1.00	0.00
R of Ex_hip_femur	0.90	-0.11	0.92	-0.18	0.98	-0.12	0.99	0.01
R of Ey_hip_femur	0.88	-0.05	0.91	-0.10	0.99	-0.06	0.99	0.01
R of Ez_hip_femur	0.96	-0.22	0.98	-0.27	0.99	-0.15	1.00	-0.01
R of E_hip_femur	0.91	0.00	0.93	0.00	0.99	0.00	0.99	0.00
R of Ex_body	0.84	0.03	0.88	0.06	0.97	0.05	0.99	0.02
R of Ey_body	0.86	0.01	0.90	-0.01	0.98	0.00	0.99	0.02
R of Ez_body	0.96	-0.23	0.96	-0.26	0.99	-0.15	1.00	0.00
R of E_body	0.89	0.00	0.92	0.00	0.99	0.00	0.99	0.00
R of Ex_head	0.90	0.00	0.92	-0.04	0.97	-0.03	0.99	0.01
R of Ey_head	0.90	0.07	0.92	0.07	0.98	0.04	0.99	0.03
R of Ez_head	0.85	0.02	0.87	0.00	0.95	0.02	0.98	0.02
R of E_head	0.92	0.00	0.92	0.00	0.97	0.00	0.99	0.00
R of Ex_total	0.91	-0.07	0.92	-0.10	0.98	-0.06	0.99	0.01
R of Ey_total	0.91	-0.01	0.93	-0.03	0.99	-0.02	0.99	0.01
R of Ez_total	0.95	-0.15	0.96	-0.18	0.99	-0.09	1.00	0.00
R of E_total	0.93	0.00	0.95	0.00	0.99	0.00	0.99	0.00
Cluster method 2	k=1		k=2		k=3		k=8	
Correlation coefficient	module	phase	module	phase	module	phase	module	phase
R of Ex_left_arm	0.98	0.01	0.99	0.02	1.00	0.00	1.00	0.00
R of Ey_left_arm	0.98	0.01	0.99	0.01	1.00	0.00	1.00	0.00
R of Ez_left_arm	0.96	-0.04	0.99	0.01	1.00	0.01	1.00	0.00
R of E_left_arm	0.98	0.00	0.99	0.00	1.00	0.00	1.00	0.00
R of Ex_right_arm	0.86	0.02	0.94	0.04	1.00	0.01	1.00	-0.01
R of Ey_right_arm	0.91	0.03	0.96	0.01	1.00	0.00	1.00	0.00
R of Ez_right_arm	0.92	-0.03	0.97	-0.01	1.00	0.01	1.00	-0.01
R of E_right_arm	0.89	0.00	0.96	0.00	1.00	0.00	1.00	0.00
R of Ex_left_tibia	0.92	-0.05	0.96	-0.01	0.99	-0.01	0.99	0.00
R of Ey_left_tibia	0.87	0.03	0.95	0.01	0.99	0.00	0.99	0.01
R of Ez_left_tibia	0.50	-0.09	0.91	-0.03	0.99	0.01	0.99	0.02
R of E_left_tibia	0.69	0.00	0.93	0.00	0.99	0.00	0.99	0.00
R of Ex_right_tibia	0.99	0.02	0.99	-0.02	1.00	-0.01	1.00	0.00
R of Ey_right_tibia	0.98	0.01	0.99	0.00	1.00	-0.01	1.00	0.00
R of Ez_right_tibia	0.59	0.01	0.91	-0.03	0.99	0.00	0.99	0.02
R of E_right_tibia	0.95	0.00	0.99	0.00	1.00	0.00	1.00	0.00
R of Ex_hip_femur	0.91	-0.01	0.95	-0.06	1.00	-0.01	1.00	0.00
R of Ey_hip_femur	0.89	-0.01	0.95	-0.03	1.00	-0.01	1.00	0.00
R of Ez_hip_femur	0.97	-0.07	0.99	-0.07	1.00	-0.01	1.00	0.00
R of E_hip_femur	0.92	0.00	0.96	0.00	1.00	0.00	1.00	0.00
R of Ex_body	0.86	-0.01	0.92	0.04	0.99	0.00	1.00	0.00
R of Ey_body	0.86	0.02	0.93	0.01	0.99	0.01	1.00	0.00

Table A-III. Correlation coefficients for the Duke model at 800 mm landmark. (continued)

R of Ez_body	0.96	-0.06	0.98	-0.04	1.00	0.00	1.00	0.01
R of E_body	0.90	0.00	0.95	0.00	0.99	0.00	1.00	0.00
R of Ex_head	0.93	-0.01	0.96	-0.04	0.99	-0.04	1.00	0.00
R of Ey_head	0.91	0.03	0.94	0.01	0.99	-0.02	0.99	0.01
R of Ez_head	0.89	0.00	0.94	-0.02	0.98	-0.02	0.99	0.01
R of E_head	0.94	0.00	0.96	0.00	0.99	0.00	1.00	0.00
R of Ex_total	0.93	-0.02	0.96	-0.03	1.00	-0.01	1.00	0.00
R of Ey_total	0.92	0.00	0.96	-0.01	1.00	0.00	1.00	0.00
R of Ez_total	0.97	-0.05	0.99	-0.04	1.00	0.00	1.00	0.01
R of E_total	0.94	0.00	0.97	0.00	1.00	0.00	1.00	0.00
Cluster method 3	k=1		k=2		k=3		k=8	
Correlation coefficient	module	phase	module	phase	module	phase	module	phase
R of Ex_left_arm	0.98	0.01	1.00	0.01	1.00	0.00	1.00	0.00
R of Ey_left_arm	0.98	0.01	1.00	0.00	1.00	0.00	1.00	0.00
R of Ez_left_arm	0.96	-0.04	1.00	0.00	1.00	0.01	1.00	0.00
R of E_left_arm	0.98	0.00	1.00	0.00	1.00	0.00	1.00	0.00
R of Ex_right_arm	0.86	0.02	0.99	0.04	0.99	0.04	1.00	-0.01
R of Ey_right_arm	0.91	0.03	0.99	0.01	0.99	0.01	1.00	0.00
R of Ez_right_arm	0.92	-0.03	0.99	0.01	1.00	0.02	1.00	0.00
R of E_right_arm	0.89	0.00	0.99	0.00	0.99	0.00	1.00	0.00
R of Ex_left_tibia	0.92	-0.05	0.99	0.00	0.99	-0.01	1.00	0.01
R of Ey_left_tibia	0.87	0.03	0.98	0.05	0.98	0.03	1.00	0.00
R of Ez_left_tibia	0.50	-0.09	0.97	0.14	0.97	0.09	0.99	0.01
R of E_left_tibia	0.69	0.00	0.98	0.00	0.98	0.00	1.00	0.00
R of Ex_right_tibia	0.99	0.02	1.00	0.00	1.00	-0.01	1.00	0.00
R of Ey_right_tibia	0.98	0.01	1.00	0.00	1.00	-0.01	1.00	0.00
R of Ez_right_tibia	0.59	0.01	0.96	0.09	0.97	0.05	0.99	0.00
R of E_right_tibia	0.95	0.00	0.99	0.00	0.99	0.00	1.00	0.00
R of Ex_hip_femur	0.91	-0.01	0.99	0.00	0.99	-0.02	1.00	-0.01
R of Ey_hip_femur	0.89	-0.01	0.99	-0.01	0.99	-0.01	1.00	-0.01
R of Ez_hip_femur	0.97	-0.07	1.00	-0.04	1.00	-0.04	1.00	0.00
R of E_hip_femur	0.92	0.00	0.99	0.00	0.99	0.00	1.00	0.00
R of Ex_body	0.86	-0.01	0.97	0.04	0.97	0.04	1.00	0.00
R of Ey_body	0.86	0.02	0.97	0.01	0.97	0.01	1.00	0.00
R of Ez_body	0.96	-0.06	0.99	-0.02	0.99	-0.02	1.00	0.00
R of E_body	0.90	0.00	0.98	0.00	0.98	0.00	1.00	0.00
R of Ex_head	0.93	-0.01	0.99	-0.02	0.99	-0.02	0.99	0.00
R of Ey_head	0.91	0.03	0.98	0.00	0.98	-0.01	0.98	-0.01
R of Ez_head	0.89	0.00	0.98	-0.03	0.98	-0.04	0.98	-0.01
R of E_head	0.94	0.00	0.99	0.00	0.99	0.00	0.99	0.00
R of Ex_total	0.93	-0.02	0.99	0.00	0.99	-0.01	1.00	0.00

Table A-III. Correlation coefficients for the Duke model at 800 mm landmark. (continued)

R of Ey_total	0.92	0.00	0.99	0.00	0.99	0.00	1.00	0.00
R of Ez_total	0.97	-0.05	0.99	-0.02	1.00	-0.02	1.00	0.00
R of E_total	0.94	0.00	0.99	0.00	0.99	0.00	1.00	0.00

Table A-IV. Correlation coefficients for the Ella model at 400 mm landmark.

landmark at 400 mm								
Cluster method 1	k=1		k=2		k=3		k=8	
Correlation coefficient	module	phase	module	phase	module	phase	module	phase
R of Ex_left_arm	0.92	-0.03	0.94	-0.03	0.99	0.00	1.00	0.01
R of Ey_left_arm	0.91	-0.01	0.94	0.00	0.99	0.02	1.00	0.00
R of Ez_left_arm	0.89	-0.07	0.94	-0.07	0.99	-0.02	1.00	0.00
R of E_left_arm	0.90	0.00	0.94	0.00	1.00	0.00	1.00	0.00
R of Ex_right_arm	0.93	0.01	0.95	-0.10	0.99	-0.07	1.00	0.01
R of Ey_right_arm	0.93	-0.02	0.95	-0.06	0.99	-0.04	1.00	0.00
R of Ez_right_arm	0.90	-0.08	0.95	-0.10	0.99	-0.04	1.00	0.00
R of E_right_arm	0.93	0.00	0.96	0.00	1.00	0.00	1.00	0.00
R of Ex_left_tibia	0.92	-0.04	0.94	0.00	0.99	0.04	1.00	0.01
R of Ey_left_tibia	0.81	0.11	0.86	0.10	0.99	0.09	1.00	0.04
R of Ez_left_tibia	0.68	-0.09	0.88	-0.12	0.99	0.07	0.99	0.06
R of E_left_tibia	0.81	0.00	0.89	0.00	0.99	0.00	1.00	0.00
R of Ex_right_tibia	0.95	0.05	0.96	0.02	0.99	-0.02	1.00	0.03
R of Ey_right_tibia	0.88	0.03	0.91	0.03	0.99	0.05	1.00	0.03
R of Ez_right_tibia	0.78	0.24	0.90	0.24	0.98	0.18	0.99	0.05
R of E_right_tibia	0.92	0.00	0.96	0.00	1.00	0.00	1.00	0.00
R of Ex_hip_femur	0.91	-0.16	0.93	-0.22	0.99	-0.15	1.00	0.01
R of Ey_hip_femur	0.91	0.00	0.93	-0.02	0.99	-0.01	1.00	0.01
R of Ez_hip_femur	0.94	-0.39	0.96	-0.35	0.99	-0.12	1.00	0.01
R of E_hip_femur	0.94	0.00	0.95	0.00	0.99	0.00	1.00	0.00
R of Ex_body	0.92	-0.19	0.94	-0.23	0.98	-0.16	1.00	0.00
R of Ey_body	0.87	-0.08	0.91	-0.10	0.98	-0.05	1.00	0.01
R of Ez_body	0.97	-0.29	0.98	-0.28	0.99	-0.15	1.00	-0.01
R of E_body	0.92	0.00	0.94	0.00	0.99	0.00	1.00	0.00
R of Ex_head	0.95	-0.03	0.96	-0.04	0.99	-0.03	0.99	0.00
R of Ey_head	0.94	0.01	0.95	0.02	0.99	0.02	0.99	0.01
R of Ez_head	0.95	-0.09	0.96	-0.09	0.99	-0.05	0.99	0.00
R of E_head	0.96	0.00	0.97	0.00	0.99	0.00	0.99	0.00
R of Ex_total	0.92	-0.16	0.93	-0.20	0.99	-0.12	1.00	0.01
R of Ey_total	0.91	-0.04	0.93	-0.05	0.99	-0.02	1.00	0.01
R of Ez_total	0.96	-0.25	0.98	-0.24	0.99	-0.12	1.00	-0.01
R of E_total	0.95	0.00	0.96	0.00	0.99	0.00	1.00	0.00
Cluster method 2	k=1		k=2		k=3		k=8	

Table A-IV. Correlation coefficients for the Ella model at 400 mm landmark. (continued)

Correlation coefficient	module	phase	module	phase	module	phase	module	Phase
R of Ex_left_arm	0.93	-0.01	0.96	0.01	1.00	0.00	1.00	0.00
R of Ey_left_arm	0.92	0.00	0.96	0.02	1.00	0.00	1.00	0.00
R of Ez_left_arm	0.90	-0.03	0.96	0.00	1.00	0.00	1.00	-0.01
R of E_left_arm	0.91	0.00	0.96	0.00	1.00	0.00	1.00	0.00
R of Ex_right_arm	0.94	0.08	0.97	-0.01	1.00	-0.01	1.00	0.00
R of Ey_right_arm	0.93	0.03	0.97	0.01	1.00	-0.01	1.00	0.00
R of Ez_right_arm	0.91	-0.01	0.97	-0.01	1.00	-0.01	1.00	0.00
R of E_right_arm	0.93	0.00	0.97	0.00	1.00	0.00	1.00	0.00
R of Ex_left_tibia	0.93	-0.07	0.96	0.00	1.00	0.00	1.00	0.00
R of Ey_left_tibia	0.84	0.05	0.93	0.04	1.00	0.01	1.00	0.02
R of Ez_left_tibia	0.72	-0.11	0.94	-0.09	0.99	0.00	0.99	0.02
R of E_left_tibia	0.84	0.00	0.95	0.00	1.00	0.00	1.00	0.00
R of Ex_right_tibia	0.95	0.04	0.98	0.00	1.00	-0.03	1.00	0.02
R of Ey_right_tibia	0.91	0.02	0.96	0.01	1.00	-0.01	1.00	0.02
R of Ez_right_tibia	0.80	0.11	0.94	0.07	0.99	-0.01	0.99	0.02
R of E_right_tibia	0.93	0.00	0.98	0.00	1.00	0.00	1.00	0.00
R of Ex_hip_femur	0.92	-0.02	0.96	-0.05	1.00	-0.03	1.00	0.01
R of Ey_hip_femur	0.91	0.03	0.95	0.02	1.00	0.00	1.00	0.00
R of Ez_hip_femur	0.95	-0.18	0.98	-0.09	1.00	0.00	1.00	0.00
R of E_hip_femur	0.96	0.00	0.97	0.00	1.00	0.00	1.00	0.00
R of Ex_body	0.94	-0.03	0.96	-0.02	0.99	-0.04	1.00	0.00
R of Ey_body	0.88	-0.01	0.93	0.00	0.99	-0.01	1.00	0.00
R of Ez_body	0.98	-0.07	0.99	-0.01	1.00	-0.01	1.00	-0.01
R of E_body	0.93	0.00	0.95	0.00	0.99	0.00	1.00	0.00
R of Ex_head	0.96	0.00	0.96	0.00	0.99	-0.02	0.99	0.00
R of Ey_head	0.95	0.02	0.96	0.04	0.99	0.01	0.99	0.00
R of Ez_head	0.95	-0.02	0.96	-0.01	0.99	-0.02	0.99	0.00
R of E_head	0.96	0.00	0.97	0.00	0.99	0.00	0.99	0.00
R of Ex_total	0.94	-0.04	0.97	-0.04	1.00	-0.03	1.00	0.00
R of Ey_total	0.92	0.00	0.95	0.01	1.00	-0.01	1.00	0.00
R of Ez_total	0.97	-0.07	0.99	-0.01	1.00	-0.01	1.00	-0.01
R of E_total	0.96	0.00	0.97	0.00	1.00	0.00	1.00	0.00
Cluster method 3	k=1		k=2		k=3		k=8	
Correlation coefficient	module	phase	module	phase	module	phase	module	phase
R of Ex_left_arm	0.93	-0.01	0.99	-0.02	1.00	-0.01	1.00	-0.01
R of Ey_left_arm	0.92	0.00	0.99	-0.02	1.00	-0.01	1.00	-0.01
R of Ez_left_arm	0.90	-0.03	0.99	-0.03	1.00	-0.01	1.00	0.00
R of E_left_arm	0.91	0.00	0.99	0.00	1.00	0.00	1.00	0.00
R of Ex_right_arm	0.94	0.08	1.00	0.05	1.00	0.02	1.00	0.01
R of Ey_right_arm	0.93	0.03	0.99	0.01	1.00	0.01	1.00	0.00

Table A-IV. Correlation coefficients for the Ella model at 400 mm landmark. (continued)

R of Ez_right_arm	0.91	-0.01	0.99	-0.01	1.00	0.00	1.00	0.00
R of E_right_arm	0.93	0.00	0.99	0.00	1.00	0.00	1.00	0.00
R of Ex_left_tibia	0.93	-0.07	0.99	-0.01	0.99	-0.02	1.00	0.00
R of Ey_left_tibia	0.84	0.05	0.99	0.04	0.99	0.04	1.00	0.01
R of Ez_left_tibia	0.72	-0.11	0.98	0.08	0.98	0.03	1.00	0.04
R of E_left_tibia	0.84	0.00	0.99	0.00	0.99	0.00	1.00	0.00
R of Ex_right_tibia	0.95	0.04	1.00	-0.01	1.00	0.00	1.00	0.00
R of Ey_right_tibia	0.91	0.02	0.99	-0.01	0.99	0.01	1.00	0.00
R of Ez_right_tibia	0.80	0.11	0.97	0.04	0.98	0.05	1.00	0.03
R of E_right_tibia	0.93	0.00	0.99	0.00	0.99	0.00	1.00	0.00
R of Ex_hip_femur	0.92	-0.02	1.00	0.00	0.99	-0.02	1.00	-0.01
R of Ey_hip_femur	0.91	0.03	1.00	0.00	0.99	0.00	1.00	0.00
R of Ez_hip_femur	0.95	-0.18	1.00	0.01	1.00	-0.04	1.00	0.00
R of E_hip_femur	0.96	0.00	1.00	0.00	1.00	0.00	1.00	0.00
R of Ex_body	0.94	-0.03	0.98	-0.03	0.99	0.00	1.00	0.00
R of Ey_body	0.88	-0.01	0.96	-0.03	0.98	-0.01	0.99	0.00
R of Ez_body	0.98	-0.07	0.99	-0.03	1.00	-0.01	1.00	0.00
R of E_body	0.93	0.00	0.97	0.00	0.98	0.00	0.99	0.00
R of Ex_head	0.96	0.00	0.98	-0.02	0.99	-0.01	0.99	0.00
R of Ey_head	0.95	0.02	0.98	-0.01	0.99	0.00	0.99	0.00
R of Ez_head	0.95	-0.02	0.98	-0.02	0.99	-0.02	0.99	0.00
R of E_head	0.96	0.00	0.98	0.00	0.99	0.00	0.99	0.00
R of Ex_total	0.94	-0.04	0.99	-0.01	0.99	-0.01	1.00	0.00
R of Ey_total	0.92	0.00	0.98	-0.01	0.99	0.00	0.99	0.00
R of Ez_total	0.97	-0.07	0.99	-0.03	1.00	-0.01	1.00	0.00
R of E_total	0.96	0.00	0.99	0.00	0.99	0.00	1.00	0.00

Table A-V. Correlation coefficients for the Ella model at 600 mm landmark.

landmark at 600 mm								
Cluster method 1	k=1		k=2		k=3		k=8	
Correlation coefficient	module	phase	module	phase	module	phase	module	phase
R of Ex_left_arm	0.94	0.04	0.95	0.03	1.00	0.02	1.00	0.01
R of Ey_left_arm	0.96	0.02	0.97	0.02	1.00	0.01	1.00	0.00
R of Ez_left_arm	0.88	0.04	0.93	0.01	0.99	0.02	1.00	0.00
R of E_left_arm	0.95	0.00	0.97	0.00	1.00	0.00	1.00	0.00
R of Ex_right_arm	0.83	0.18	0.88	0.11	0.99	0.10	1.00	0.02
R of Ey_right_arm	0.91	0.05	0.93	0.02	0.99	0.02	1.00	0.01
R of Ez_right_arm	0.86	0.07	0.92	0.04	0.99	0.06	1.00	0.01
R of E_right_arm	0.87	0.00	0.91	0.00	0.99	0.00	1.00	0.00
R of Ex_left_tibia	0.85	0.00	0.88	0.04	0.99	0.08	0.99	0.03
R of Ey_left_tibia	0.81	0.07	0.87	0.01	0.98	0.04	0.99	0.05

Table A-V. Correlation coefficients for the Ella model at 600 mm landmark. (continued)

R of Ez_left_tibia	0.69	-0.07	0.90	-0.04	0.99	0.10	0.99	0.05
R of E_left_tibia	0.72	0.00	0.85	0.00	0.99	0.00	0.99	0.00
R of Ex_right_tibia	0.98	-0.06	0.98	-0.11	1.00	-0.11	1.00	0.00
R of Ey_right_tibia	0.96	-0.03	0.97	-0.06	1.00	-0.06	1.00	0.01
R of Ez_right_tibia	0.77	0.02	0.88	-0.06	0.98	-0.04	0.99	0.04
R of E_right_tibia	0.97	0.00	0.98	0.00	1.00	0.00	1.00	0.00
R of Ex_hip_femur	0.87	-0.15	0.90	-0.18	0.98	-0.12	1.00	0.00
R of Ey_hip_femur	0.88	-0.04	0.91	-0.06	0.99	-0.02	1.00	0.01
R of Ez_hip_femur	0.96	-0.35	0.98	-0.31	1.00	-0.11	1.00	0.00
R of E_hip_femur	0.92	0.00	0.93	0.00	0.99	0.00	1.00	0.00
R of Ex_body	0.86	-0.03	0.88	-0.06	0.97	-0.05	1.00	0.00
R of Ey_body	0.88	0.00	0.91	-0.01	0.98	0.00	0.99	0.01
R of Ez_body	0.97	-0.30	0.98	-0.29	0.99	-0.13	1.00	0.00
R of E_body	0.91	0.00	0.92	0.00	0.98	0.00	1.00	0.00
R of Ex_head	0.95	-0.07	0.95	-0.08	0.98	-0.06	0.99	0.00
R of Ey_head	0.90	0.03	0.92	0.03	0.98	0.03	0.99	0.01
R of Ez_head	0.94	-0.11	0.95	-0.10	0.98	-0.06	0.99	0.00
R of E_head	0.96	0.00	0.96	0.00	0.99	0.00	0.99	0.00
R of Ex_total	0.88	-0.13	0.89	-0.15	0.98	-0.09	1.00	0.01
R of Ey_total	0.90	-0.02	0.92	-0.03	0.99	-0.01	1.00	0.01
R of Ez_total	0.96	-0.24	0.97	-0.22	0.99	-0.09	1.00	0.00
R of E_total	0.93	0.00	0.94	0.00	0.99	0.00	1.00	0.00
Cluster method 2	k=1		k=2		k=3		k=8	
Correlation coefficient	module	phase	module	phase	module	phase	module	phase
R of Ex_left_arm	0.94	0.04	0.96	0.03	1.00	0.00	1.00	0.00
R of Ey_left_arm	0.96	0.03	0.98	0.03	1.00	0.00	1.00	0.00
R of Ez_left_arm	0.90	0.04	0.96	0.02	1.00	0.00	1.00	0.00
R of E_left_arm	0.96	0.00	0.97	0.00	1.00	0.00	1.00	0.00
R of Ex_right_arm	0.85	0.11	0.91	0.04	1.00	0.01	1.00	-0.01
R of Ey_right_arm	0.91	0.05	0.95	0.03	1.00	0.00	1.00	0.00
R of Ez_right_arm	0.89	0.05	0.96	0.02	1.00	0.01	1.00	0.00
R of E_right_arm	0.88	0.00	0.94	0.00	1.00	0.00	1.00	0.00
R of Ex_left_tibia	0.85	-0.08	0.92	-0.02	1.00	0.00	1.00	0.01
R of Ey_left_tibia	0.83	0.09	0.93	0.02	1.00	0.01	1.00	0.02
R of Ez_left_tibia	0.71	-0.13	0.94	-0.06	0.99	0.01	0.99	0.02
R of E_left_tibia	0.75	0.00	0.93	0.00	1.00	0.00	0.99	0.00
R of Ex_right_tibia	0.98	0.02	0.99	-0.01	1.00	-0.02	1.00	0.01
R of Ey_right_tibia	0.97	0.01	0.98	0.00	1.00	-0.02	1.00	0.01
R of Ez_right_tibia	0.80	0.07	0.94	-0.02	0.99	-0.03	0.99	0.02
R of E_right_tibia	0.97	0.00	0.99	0.00	1.00	0.00	1.00	0.00
R of Ex_hip_femur	0.90	-0.05	0.95	-0.04	1.00	-0.03	1.00	0.00

Table A-V. Correlation coefficients for the Ella model at 600 mm landmark. (continued)

R of Ey_hip_femur	0.89	0.00	0.94	0.00	1.00	0.00	1.00	0.00
R of Ez_hip_femur	0.97	-0.16	0.99	-0.09	1.00	-0.01	1.00	0.00
R of E_hip_femur	0.94	0.00	0.97	0.00	1.00	0.00	1.00	0.00
R of Ex_body	0.90	0.03	0.94	0.04	0.99	-0.02	1.00	0.00
R of Ey_body	0.89	0.02	0.93	0.02	0.99	0.00	0.99	0.00
R of Ez_body	0.98	-0.09	0.99	-0.02	1.00	0.00	1.00	0.00
R of E_body	0.93	0.00	0.95	0.00	0.99	0.00	1.00	0.00
R of Ex_head	0.96	-0.03	0.97	-0.02	0.99	-0.04	1.00	0.00
R of Ey_head	0.91	0.03	0.93	0.03	0.99	0.00	0.99	0.00
R of Ez_head	0.95	-0.05	0.96	-0.02	0.99	-0.03	0.99	0.00
R of E_head	0.96	0.00	0.97	0.00	0.99	0.00	1.00	0.00
R of Ex_total	0.92	-0.05	0.95	-0.03	1.00	-0.02	1.00	0.00
R of Ey_total	0.91	0.00	0.95	0.01	1.00	0.00	1.00	0.00
R of Ez_total	0.97	-0.09	0.99	-0.03	1.00	0.00	1.00	0.00
R of E_total	0.95	0.00	0.97	0.00	1.00	0.00	1.00	0.00
Cluster method 3	k=1		k=2		k=3		k=8	
Correlation coefficient	module	phase	module	phase	module	phase	module	phase
R of Ex_left_arm	0.94	0.04	1.00	-0.01	1.00	0.01	1.00	0.00
R of Ey_left_arm	0.96	0.03	1.00	0.00	1.00	0.00	1.00	0.00
R of Ez_left_arm	0.90	0.04	0.99	-0.02	1.00	0.00	1.00	0.00
R of E_left_arm	0.96	0.00	1.00	0.00	1.00	0.00	1.00	0.00
R of Ex_right_arm	0.85	0.11	0.99	0.00	0.99	0.03	1.00	-0.01
R of Ey_right_arm	0.91	0.05	1.00	0.01	1.00	0.02	1.00	0.00
R of Ez_right_arm	0.89	0.05	0.99	0.00	1.00	0.02	1.00	0.00
R of E_right_arm	0.88	0.00	0.99	0.00	1.00	0.00	1.00	0.00
R of Ex_left_tibia	0.85	-0.08	0.99	0.01	0.99	0.00	1.00	0.01
R of Ey_left_tibia	0.83	0.09	0.99	0.05	0.99	0.05	1.00	0.02
R of Ez_left_tibia	0.71	-0.13	0.97	0.07	0.98	0.02	1.00	0.03
R of E_left_tibia	0.75	0.00	0.98	0.00	0.99	0.00	1.00	0.00
R of Ex_right_tibia	0.98	0.02	1.00	0.00	1.00	-0.01	1.00	0.00
R of Ey_right_tibia	0.97	0.01	1.00	0.00	1.00	-0.01	1.00	0.00
R of Ez_right_tibia	0.80	0.07	0.97	0.01	0.98	0.02	1.00	0.01
R of E_right_tibia	0.97	0.00	1.00	0.00	1.00	0.00	1.00	0.00
R of Ex_hip_femur	0.90	-0.05	1.00	0.00	1.00	-0.02	1.00	-0.01
R of Ey_hip_femur	0.89	0.00	1.00	0.00	0.99	0.00	1.00	0.00
R of Ez_hip_femur	0.97	-0.16	1.00	0.00	1.00	-0.03	1.00	0.00
R of E_hip_femur	0.94	0.00	1.00	0.00	1.00	0.00	1.00	0.00
R of Ex_body	0.90	0.03	0.97	-0.03	0.98	0.02	0.99	0.01
R of Ey_body	0.89	0.02	0.96	-0.01	0.98	0.00	0.98	0.00
R of Ez_body	0.98	-0.09	0.99	-0.01	1.00	-0.02	1.00	0.00
R of E_body	0.93	0.00	0.97	0.00	0.98	0.00	0.99	0.00

Table A-V. Correlation coefficients for the Ella model at 600 mm landmark. (continued)

R of Ex_head	0.96	-0.03	0.98	-0.04	0.99	-0.01	0.99	0.00
R of Ey_head	0.91	0.03	0.97	-0.01	0.98	0.01	0.99	0.00
R of Ez_head	0.95	-0.05	0.98	-0.04	0.99	-0.02	0.99	0.00
R of E_head	0.96	0.00	0.99	0.00	0.99	0.00	0.99	0.00
R of Ex_total	0.92	-0.05	0.99	-0.01	0.99	-0.01	1.00	0.00
R of Ey_total	0.91	0.00	0.98	0.00	0.99	0.00	0.99	0.00
R of Ez_total	0.97	-0.09	0.99	-0.01	1.00	-0.02	1.00	0.00
R of E_total	0.95	0.00	0.99	0.00	0.99	0.00	1.00	0.00

Table A-VI. Correlation coefficients for the Ella model at 800 mm landmark.

landmark at 800 mm								
Cluster method 1	k=1		k=2		k=3		k=8	
Correlation coefficient	module	phase	module	phase	module	phase	module	phase
R of Ex_left_arm	0.95	0.04	0.96	0.03	1.00	0.02	1.00	0.00
R of Ey_left_arm	0.97	0.04	0.98	0.03	1.00	0.01	1.00	0.00
R of Ez_left_arm	0.90	0.04	0.94	0.02	0.99	0.03	1.00	0.01
R of E_left_arm	0.96	0.00	0.97	0.00	1.00	0.00	1.00	0.00
R of Ex_right_arm	0.87	0.22	0.90	0.21	1.00	0.17	1.00	0.01
R of Ey_right_arm	0.90	0.00	0.93	-0.02	0.99	0.00	1.00	0.01
R of Ez_right_arm	0.89	0.09	0.94	0.08	0.99	0.09	1.00	0.01
R of E_right_arm	0.88	0.00	0.92	0.00	0.99	0.00	1.00	0.00
R of Ex_left_tibia	0.92	0.05	0.94	0.08	0.99	0.08	1.00	0.01
R of Ey_left_tibia	0.88	0.06	0.92	0.05	0.98	0.05	1.00	0.02
R of Ez_left_tibia	0.70	-0.01	0.89	0.00	0.99	0.09	0.99	0.04
R of E_left_tibia	0.86	0.00	0.92	0.00	0.99	0.00	1.00	0.00
R of Ex_right_tibia	0.97	-0.03	0.98	-0.07	1.00	-0.08	1.00	0.00
R of Ey_right_tibia	0.97	0.02	0.98	0.00	1.00	-0.02	1.00	0.00
R of Ez_right_tibia	0.82	-0.03	0.91	-0.08	0.99	-0.03	0.99	0.03
R of E_right_tibia	0.97	0.00	0.98	0.00	1.00	0.00	1.00	0.00
R of Ex_hip_femur	0.85	-0.04	0.87	-0.04	0.98	-0.03	1.00	0.00
R of Ey_hip_femur	0.84	-0.08	0.89	-0.11	0.99	-0.03	1.00	0.02
R of Ez_hip_femur	0.96	-0.29	0.97	-0.27	1.00	-0.10	1.00	0.00
R of E_hip_femur	0.90	0.00	0.92	0.00	0.98	0.00	1.00	0.00
R of Ex_body	0.86	0.17	0.88	0.17	0.97	0.10	1.00	0.00
R of Ey_body	0.89	0.03	0.91	0.02	0.98	0.03	0.99	0.01
R of Ez_body	0.96	-0.31	0.97	-0.28	0.99	-0.11	1.00	0.00
R of E_body	0.92	0.00	0.93	0.00	0.98	0.00	1.00	0.00
R of Ex_head	0.94	-0.01	0.94	-0.02	0.98	-0.01	0.99	0.00
R of Ey_head	0.85	0.08	0.89	0.08	0.97	0.07	0.98	0.02
R of Ez_head	0.89	-0.07	0.91	-0.04	0.96	0.02	0.98	0.02
R of E_head	0.93	0.00	0.94	0.00	0.98	0.00	0.99	0.00

Table A-VI. Correlation coefficients for the Ella model at 800 mm landmark. (continued)

R of Ex_total	0.87	-0.03	0.89	-0.02	0.98	-0.01	1.00	0.00
R of Ey_total	0.91	-0.01	0.93	-0.02	0.99	0.00	1.00	0.01
R of Ez_total	0.95	-0.21	0.96	-0.19	0.99	-0.06	1.00	0.00
R of E_total	0.93	0.00	0.94	0.00	0.99	0.00	1.00	0.00
Cluster method 2	k=1		k=2		k=3		k=8	
Correlation coefficient	module	phase	module	phase	module	phase	module	phase
R of Ex_left_arm	0.95	0.03	0.97	0.03	1.00	0.00	1.00	0.00
R of Ey_left_arm	0.97	0.03	0.98	0.03	1.00	0.00	1.00	0.00
R of Ez_left_arm	0.91	0.04	0.96	0.01	1.00	0.00	1.00	0.00
R of E_left_arm	0.97	0.00	0.98	0.00	1.00	0.00	1.00	0.00
R of Ex_right_arm	0.87	0.08	0.92	0.07	1.00	0.03	1.00	-0.01
R of Ey_right_arm	0.91	0.02	0.95	0.00	1.00	0.00	1.00	0.00
R of Ez_right_arm	0.90	0.02	0.97	0.01	1.00	0.01	1.00	0.00
R of E_right_arm	0.89	0.00	0.94	0.00	1.00	0.00	1.00	0.00
R of Ex_left_tibia	0.92	-0.02	0.96	0.02	1.00	0.01	1.00	0.00
R of Ey_left_tibia	0.89	0.05	0.95	0.04	1.00	0.01	1.00	0.01
R of Ez_left_tibia	0.72	-0.04	0.94	0.00	0.99	0.01	0.99	0.01
R of E_left_tibia	0.87	0.00	0.96	0.00	1.00	0.00	1.00	0.00
R of Ex_right_tibia	0.97	0.03	0.98	0.01	1.00	-0.01	1.00	0.00
R of Ey_right_tibia	0.97	0.02	0.99	0.02	1.00	0.00	1.00	0.00
R of Ez_right_tibia	0.84	0.02	0.95	-0.02	0.99	-0.01	0.99	0.01
R of E_right_tibia	0.97	0.00	0.99	0.00	1.00	0.00	1.00	0.00
R of Ex_hip_femur	0.90	-0.03	0.94	-0.01	1.00	-0.01	1.00	0.00
R of Ey_hip_femur	0.86	-0.05	0.93	-0.04	1.00	-0.01	1.00	0.00
R of Ez_hip_femur	0.97	-0.13	0.99	-0.08	1.00	-0.01	1.00	0.00
R of E_hip_femur	0.92	0.00	0.96	0.00	1.00	0.00	1.00	0.00
R of Ex_body	0.88	0.08	0.92	0.11	0.99	0.02	1.00	-0.01
R of Ey_body	0.89	0.03	0.93	0.03	0.99	0.01	0.99	0.00
R of Ez_body	0.97	-0.11	0.99	-0.04	1.00	0.00	1.00	0.00
R of E_body	0.94	0.00	0.95	0.00	1.00	0.00	1.00	0.00
R of Ex_head	0.95	-0.03	0.97	-0.03	0.99	-0.03	0.99	0.00
R of Ey_head	0.86	0.01	0.91	0.00	0.98	-0.01	0.99	0.00
R of Ez_head	0.90	-0.09	0.92	-0.04	0.98	-0.02	0.99	0.00
R of E_head	0.94	0.00	0.96	0.00	0.99	0.00	0.99	0.00
R of Ex_total	0.92	-0.02	0.95	0.00	1.00	-0.01	1.00	0.00
R of Ey_total	0.92	0.00	0.95	0.00	1.00	0.00	1.00	0.00
R of Ez_total	0.97	-0.09	0.99	-0.04	1.00	0.00	1.00	0.00
R of E_total	0.95	0.00	0.97	0.00	1.00	0.00	1.00	0.00
Cluster method 3	k=1		k=2		k=3		k=8	
Correlation coefficient	module	phase	module	phase	module	phase	module	phase
R of Ex_left_arm	0.95	0.03	1.00	0.00	1.00	0.01	1.00	0.00

Table A-VI. Correlation coefficients for the Ella model at 800 mm landmark. (continued)

R of Ey_left_arm	0.97	0.03	1.00	0.00	1.00	0.00	1.00	0.00
R of Ez_left_arm	0.91	0.04	0.99	-0.01	1.00	0.00	1.00	0.00
R of E_left_arm	0.97	0.00	1.00	0.00	1.00	0.00	1.00	0.00
R of Ex_right_arm	0.87	0.08	1.00	0.00	1.00	0.01	1.00	-0.01
R of Ey_right_arm	0.91	0.02	1.00	0.01	1.00	0.01	1.00	0.00
R of Ez_right_arm	0.90	0.02	0.99	0.00	1.00	0.01	1.00	0.00
R of E_right_arm	0.89	0.00	1.00	0.00	1.00	0.00	1.00	0.00
R of Ex_left_tibia	0.92	-0.02	0.99	0.00	0.99	0.00	1.00	0.00
R of Ey_left_tibia	0.89	0.05	0.99	0.02	0.99	0.03	1.00	0.01
R of Ez_left_tibia	0.72	-0.04	0.98	0.04	0.98	0.02	1.00	0.02
R of E_left_tibia	0.87	0.00	0.99	0.00	0.99	0.00	1.00	0.00
R of Ex_right_tibia	0.97	0.03	1.00	0.00	1.00	0.00	1.00	0.00
R of Ey_right_tibia	0.97	0.02	1.00	0.00	1.00	0.00	1.00	0.00
R of Ez_right_tibia	0.84	0.02	0.97	0.01	0.98	0.01	1.00	0.00
R of E_right_tibia	0.97	0.00	1.00	0.00	1.00	0.00	1.00	0.00
R of Ex_hip_femur	0.90	-0.03	1.00	-0.01	1.00	-0.01	1.00	0.00
R of Ey_hip_femur	0.86	-0.05	0.99	0.00	0.99	-0.01	1.00	0.00
R of Ez_hip_femur	0.97	-0.13	1.00	0.00	1.00	-0.02	1.00	0.00
R of E_hip_femur	0.92	0.00	1.00	0.00	1.00	0.00	1.00	0.00
R of Ex_body	0.88	0.08	0.98	-0.02	0.99	0.02	0.99	0.01
R of Ey_body	0.89	0.03	0.97	0.00	0.98	0.00	0.98	0.01
R of Ez_body	0.97	-0.11	0.99	0.01	1.00	-0.03	1.00	0.00
R of E_body	0.94	0.00	0.99	0.00	0.99	0.00	0.99	0.00
R of Ex_head	0.95	-0.03	0.98	-0.02	0.99	-0.02	0.99	0.00
R of Ey_head	0.86	0.01	0.95	-0.01	0.98	0.00	0.98	0.00
R of Ez_head	0.90	-0.09	0.95	-0.02	0.98	-0.04	0.98	0.00
R of E_head	0.94	0.00	0.97	0.00	0.99	0.00	0.99	0.00
R of Ex_total	0.92	-0.02	0.99	-0.01	0.99	-0.01	1.00	0.00
R of Ey_total	0.92	0.00	0.99	0.00	0.99	0.00	0.99	0.00
R of Ez_total	0.97	-0.09	1.00	0.00	1.00	-0.02	1.00	0.00
R of E_total	0.95	0.00	0.99	0.00	1.00	0.00	1.00	0.00

Table A-VII. Correlation coefficients for the FATS model at 400 mm landmark.

landmark at 400 mm								
Cluster method 1	k=1		k=2		k=3		k=8	
Correlation coefficient	module	phase	module	phase	module	phase	module	phase
R of Ex_left_arm	0.94	-0.07	0.96	-0.09	0.96	-0.08	1.00	0.02
R of Ey_left_arm	0.86	-0.14	0.91	-0.12	0.91	-0.12	1.00	0.02
R of Ez_left_arm	0.88	-0.17	0.94	-0.17	0.93	-0.17	1.00	0.01
R of E_left_arm	0.90	0.00	0.95	0.00	0.94	0.00	1.00	0.00
R of Ex_right_arm	0.94	0.02	0.95	-0.04	0.95	-0.02	1.00	0.03

Table A-VII. Correlation coefficients for the FATS model at 400 mm landmark. (continued)

R of Ey_right_arm	0.91	-0.09	0.94	-0.09	0.94	-0.09	1.00	0.01
R of Ez_right_arm	0.88	-0.15	0.94	-0.15	0.93	-0.14	1.00	0.01
R of E_right_arm	0.91	0.00	0.95	0.00	0.95	0.00	1.00	0.00
R of Ex_left_tibia	0.96	0.01	0.97	-0.02	0.97	-0.01	1.00	0.02
R of Ey_left_tibia	0.93	0.10	0.95	0.08	0.95	0.06	1.00	0.01
R of Ez_left_tibia	0.80	0.04	0.84	-0.03	0.85	-0.01	0.99	0.03
R of E_left_tibia	0.95	0.00	0.96	0.00	0.96	0.00	1.00	0.00
R of Ex_right_tibia	0.93	-0.09	0.95	-0.10	0.96	-0.09	1.00	0.01
R of Ey_right_tibia	0.94	-0.21	0.96	-0.19	0.96	-0.16	1.00	0.02
R of Ez_right_tibia	0.75	-0.08	0.81	-0.13	0.85	-0.11	0.99	0.02
R of E_right_tibia	0.93	0.00	0.95	0.00	0.96	0.00	1.00	0.00
R of Ex_hip_femur	0.78	-0.13	0.84	-0.20	0.84	-0.19	1.00	0.02
R of Ey_hip_femur	0.83	-0.05	0.87	-0.09	0.86	-0.08	1.00	0.02
R of Ez_hip_femur	0.89	-0.56	0.93	-0.48	0.93	-0.46	1.00	0.00
R of E_hip_femur	0.86	0.00	0.90	0.00	0.91	0.00	1.00	0.00
R of Ex_body	0.82	-0.31	0.87	-0.32	0.88	-0.30	1.00	0.01
R of Ey_body	0.69	-0.36	0.79	-0.37	0.78	-0.35	1.00	0.02
R of Ez_body	0.94	-0.52	0.96	-0.47	0.96	-0.44	1.00	0.00
R of E_body	0.77	0.00	0.85	0.00	0.84	0.00	1.00	0.00
R of Ex_head	0.78	-0.15	0.83	-0.20	0.84	-0.17	0.99	0.02
R of Ey_head	0.84	-0.02	0.88	-0.03	0.88	-0.03	0.99	0.02
R of Ez_head	0.93	-0.21	0.95	-0.17	0.95	-0.14	0.99	0.01
R of E_head	0.85	0.00	0.90	0.00	0.90	0.00	0.99	0.00
R of Ex_total	0.82	-0.23	0.87	-0.25	0.88	-0.24	1.00	0.01
R of Ey_total	0.73	-0.25	0.81	-0.27	0.81	-0.26	1.00	0.02
R of Ez_total	0.91	-0.43	0.95	-0.39	0.95	-0.37	1.00	0.00
R of E_total	0.86	0.00	0.91	0.00	0.91	0.00	1.00	0.00
Cluster method 2	k=1		k=2		k=3		k=8	
Correlation coefficient	module	phase	module	phase	module	phase	module	phase
R of Ex_left_arm	0.95	-0.02	0.98	-0.01	0.98	-0.01	1.00	0.00
R of Ey_left_arm	0.87	-0.08	0.96	0.00	0.96	0.00	1.00	0.00
R of Ez_left_arm	0.92	-0.09	0.99	-0.03	0.99	-0.03	1.00	0.00
R of E_left_arm	0.92	0.00	0.98	0.00	0.98	0.00	1.00	0.00
R of Ex_right_arm	0.95	0.09	0.98	-0.02	0.98	-0.03	1.00	0.00
R of Ey_right_arm	0.91	-0.02	0.97	-0.01	0.97	-0.02	1.00	0.00
R of Ez_right_arm	0.92	-0.06	0.98	-0.03	0.98	-0.03	1.00	0.00
R of E_right_arm	0.92	0.00	0.98	0.00	0.98	0.00	1.00	0.00
R of Ex_left_tibia	0.96	-0.02	0.98	0.00	0.98	0.01	1.00	0.00
R of Ey_left_tibia	0.95	0.01	0.98	0.05	0.98	0.05	1.00	0.00
R of Ez_left_tibia	0.85	0.05	0.94	-0.11	0.95	-0.09	0.99	0.00
R of E_left_tibia	0.96	0.00	0.98	0.00	0.98	0.00	1.00	0.00

Table A-VII. Correlation coefficients for the FATS model at 400 mm landmark. (continued)

R of Ex_right_tibia	0.97	0.03	0.99	0.00	0.99	0.01	1.00	0.00
R of Ey_right_tibia	0.97	-0.06	0.99	-0.01	0.99	0.00	1.00	0.00
R of Ez_right_tibia	0.90	-0.02	0.98	-0.06	0.98	-0.04	1.00	0.00
R of E_right_tibia	0.97	0.00	0.99	0.00	0.99	0.00	1.00	0.00
R of Ex_hip_femur	0.87	-0.05	0.95	-0.08	0.95	-0.08	1.00	0.01
R of Ey_hip_femur	0.86	-0.02	0.94	-0.02	0.95	-0.02	1.00	0.00
R of Ez_hip_femur	0.94	-0.26	0.98	-0.13	0.98	-0.11	1.00	-0.01
R of E_hip_femur	0.92	0.00	0.97	0.00	0.97	0.00	1.00	0.00
R of Ex_body	0.88	-0.11	0.95	-0.06	0.95	-0.05	1.00	-0.01
R of Ey_body	0.76	-0.17	0.90	-0.07	0.91	-0.06	1.00	-0.01
R of Ez_body	0.96	-0.17	0.98	-0.06	0.98	-0.05	1.00	0.00
R of E_body	0.80	0.00	0.91	0.00	0.90	0.00	1.00	0.00
R of Ex_head	0.83	-0.02	0.90	-0.06	0.92	-0.04	0.99	0.00
R of Ey_head	0.85	0.02	0.92	0.02	0.93	0.02	0.99	0.00
R of Ez_head	0.93	-0.02	0.97	-0.03	0.97	-0.01	1.00	0.00
R of E_head	0.86	0.00	0.93	0.00	0.94	0.00	0.99	0.00
R of Ex_total	0.89	-0.09	0.95	-0.06	0.96	-0.05	1.00	0.00
R of Ey_total	0.79	-0.13	0.92	-0.06	0.92	-0.05	1.00	-0.01
R of Ez_total	0.95	-0.15	0.98	-0.05	0.98	-0.05	1.00	0.00
R of E_total	0.90	0.00	0.96	0.00	0.96	0.00	1.00	0.00
Cluster method 3	k=1		k=2		k=3		k=8	
Correlation coefficient	module	phase	module	phase	module	phase	module	phase
R of Ex_left_arm	0.95	-0.02	0.99	-0.03	0.99	-0.03	0.00	-0.02
R of Ey_left_arm	0.87	-0.08	0.97	-0.03	0.98	-0.02	1.00	-0.01
R of Ez_left_arm	0.92	-0.09	0.98	-0.02	0.99	-0.01	1.00	0.00
R of E_left_arm	0.92	0.00	0.98	0.00	0.99	0.00	1.00	0.00
R of Ex_right_arm	0.95	0.09	0.99	0.00	0.99	-0.02	1.00	-0.01
R of Ey_right_arm	0.91	-0.02	0.98	-0.02	0.99	-0.02	1.00	-0.01
R of Ez_right_arm	0.92	-0.06	0.98	-0.03	0.99	-0.03	1.00	0.00
R of E_right_arm	0.92	0.00	0.98	0.00	0.99	0.00	1.00	0.00
R of Ex_left_tibia	0.96	-0.02	0.99	-0.01	0.99	-0.01	1.00	-0.01
R of Ey_left_tibia	0.95	0.01	0.98	0.01	0.98	0.02	1.00	0.00
R of Ez_left_tibia	0.85	0.05	0.91	0.07	0.93	0.02	0.99	0.01
R of E_left_tibia	0.96	0.00	0.98	0.00	0.98	0.00	1.00	0.00
R of Ex_right_tibia	0.97	0.03	0.99	0.00	0.99	-0.01	1.00	-0.01
R of Ey_right_tibia	0.97	-0.06	0.99	0.01	0.99	0.00	1.00	0.00
R of Ez_right_tibia	0.90	-0.02	0.96	0.04	0.97	0.01	0.99	0.00
R of E_right_tibia	0.97	0.00	0.99	0.00	0.99	0.00	1.00	0.00
R of Ex_hip_femur	0.87	-0.05	0.99	-0.03	0.99	-0.05	1.00	-0.02
R of Ey_hip_femur	0.86	-0.02	0.99	-0.01	0.99	-0.01	1.00	-0.01
R of Ez_hip_femur	0.94	-0.26	0.99	-0.01	0.99	-0.02	1.00	-0.01

Table A-VII. Correlation coefficients for the FATS model at 400 mm landmark. (continued)

R of E_hip_femur	0.92	0.00	0.99	0.00	0.99	0.00	1.00	0.00
R of Ex_body	0.88	-0.11	0.97	-0.02	0.98	-0.03	0.99	0.00
R of Ey_body	0.76	-0.17	0.95	-0.01	0.96	-0.01	0.99	0.00
R of Ez_body	0.96	-0.17	0.99	-0.01	0.99	-0.01	1.00	0.00
R of E_body	0.80	0.00	0.95	0.00	0.96	0.00	0.99	0.00
R of Ex_head	0.83	-0.02	0.92	-0.01	0.93	-0.03	0.98	0.00
R of Ey_head	0.85	0.02	0.92	0.00	0.93	0.01	0.98	0.00
R of Ez_head	0.93	-0.02	0.96	0.00	0.96	0.00	0.99	0.00
R of E_head	0.86	0.00	0.93	0.00	0.93	0.00	0.98	0.00
R of Ex_total	0.89	-0.09	0.98	-0.02	0.98	-0.03	0.99	0.00
R of Ey_total	0.79	-0.13	0.96	-0.01	0.96	-0.01	0.99	0.00
R of Ez_total	0.95	-0.15	0.99	-0.01	0.99	-0.01	1.00	0.00
R of E_total	0.90	0.00	0.97	0.00	0.98	0.00	1.00	0.00

Table A-VIII. Correlation coefficients for the FATS model at 600 mm landmark.

landmark at 600 mm								
Cluster method 1	k=1		k=2		k=3		k=8	
Correlation coefficient	module	phase	module	phase	module	phase	module	phase
R of Ex_left_arm	0.93	0.08	0.95	0.06	0.95	0.04	1.00	0.02
R of Ey_left_arm	0.92	0.05	0.94	0.02	0.94	0.02	1.00	0.02
R of Ez_left_arm	0.88	-0.05	0.93	-0.06	0.93	-0.09	1.00	0.00
R of E_left_arm	0.93	0.00	0.96	0.00	0.95	0.00	1.00	0.00
R of Ex_right_arm	0.90	0.14	0.93	0.09	0.93	0.07	1.00	0.03
R of Ey_right_arm	0.87	0.00	0.91	-0.01	0.91	-0.02	1.00	0.02
R of Ez_right_arm	0.88	-0.08	0.93	-0.07	0.93	-0.10	1.00	0.00
R of E_right_arm	0.89	0.00	0.93	0.00	0.93	0.00	1.00	0.00
R of Ex_left_tibia	0.82	0.13	0.86	0.10	0.86	0.09	0.99	0.04
R of Ey_left_tibia	0.80	0.09	0.87	0.04	0.88	0.03	0.99	0.05
R of Ez_left_tibia	0.65	0.09	0.83	0.00	0.79	0.00	0.98	0.05
R of E_left_tibia	0.68	0.00	0.83	0.00	0.79	0.00	0.99	0.00
R of Ex_right_tibia	0.97	-0.09	0.97	-0.14	0.97	-0.09	1.00	0.03
R of Ey_right_tibia	0.96	-0.05	0.97	-0.08	0.97	-0.05	1.00	0.03
R of Ez_right_tibia	0.74	-0.01	0.86	-0.10	0.84	-0.06	0.99	0.05
R of E_right_tibia	0.94	0.00	0.96	0.00	0.96	0.00	1.00	0.00
R of Ex_hip_femur	0.79	-0.25	0.86	-0.30	0.86	-0.27	1.00	0.02
R of Ey_hip_femur	0.80	-0.09	0.85	-0.14	0.84	-0.12	1.00	0.03
R of Ez_hip_femur	0.93	-0.49	0.96	-0.41	0.96	-0.38	1.00	0.00
R of E_hip_femur	0.87	0.00	0.91	0.00	0.92	0.00	1.00	0.00
R of Ex_body	0.76	-0.21	0.82	-0.23	0.83	-0.25	1.00	0.02
R of Ey_body	0.66	-0.30	0.76	-0.34	0.76	-0.34	0.99	0.03
R of Ez_body	0.93	-0.55	0.96	-0.48	0.96	-0.46	1.00	0.00

Table A-VIII. Correlation coefficients for the FATS model at 600 mm landmark. (continued)

R of E_body	0.76	0.00	0.84	0.00	0.83	0.00	1.00	0.00
R of Ex_head	0.79	-0.18	0.84	-0.26	0.85	-0.22	0.99	0.01
R of Ey_head	0.87	0.01	0.90	-0.02	0.90	-0.02	0.99	0.01
R of Ez_head	0.91	-0.20	0.93	-0.19	0.93	-0.16	0.99	0.00
R of E_head	0.87	0.00	0.90	0.00	0.91	0.00	0.99	0.00
R of Ex_total	0.79	-0.20	0.84	-0.22	0.86	-0.22	1.00	0.02
R of Ey_total	0.73	-0.19	0.81	-0.22	0.81	-0.22	1.00	0.02
R of Ez_total	0.90	-0.43	0.94	-0.39	0.94	-0.38	1.00	0.00
R of E_total	0.84	0.00	0.90	0.00	0.90	0.00	1.00	0.00
Cluster method 2	k=1		k=2		k=3		k=8	
Correlation coefficient	module	phase	module	phase	module	phase	module	phase
R of Ex_left_arm	0.95	0.02	0.98	0.04	0.98	0.03	1.00	0.01
R of Ey_left_arm	0.92	0.02	0.97	0.03	0.97	0.02	1.00	0.00
R of Ez_left_arm	0.92	-0.09	0.98	-0.01	0.98	-0.02	1.00	0.00
R of E_left_arm	0.93	0.00	0.98	0.00	0.98	0.00	1.00	0.00
R of Ex_right_arm	0.92	0.06	0.97	0.02	0.97	-0.01	1.00	0.00
R of Ey_right_arm	0.87	0.01	0.96	0.00	0.96	0.00	1.00	0.00
R of Ez_right_arm	0.91	-0.08	0.98	-0.02	0.98	-0.03	1.00	0.00
R of E_right_arm	0.89	0.00	0.97	0.00	0.97	0.00	1.00	0.00
R of Ex_left_tibia	0.84	0.02	0.93	-0.01	0.94	0.00	0.99	0.01
R of Ey_left_tibia	0.86	0.09	0.95	0.00	0.95	0.00	0.99	0.01
R of Ez_left_tibia	0.73	0.03	0.96	-0.05	0.96	-0.04	0.99	0.00
R of E_left_tibia	0.73	0.00	0.96	0.00	0.95	0.00	0.99	0.00
R of Ex_right_tibia	0.97	0.05	0.99	0.00	0.99	0.00	1.00	0.01
R of Ey_right_tibia	0.97	0.02	0.99	0.01	0.99	0.02	1.00	0.00
R of Ez_right_tibia	0.79	0.05	0.97	-0.02	0.97	0.00	0.99	0.00
R of E_right_tibia	0.95	0.00	0.99	0.00	0.99	0.00	1.00	0.00
R of Ex_hip_femur	0.87	-0.07	0.95	-0.08	0.95	-0.08	1.00	0.01
R of Ey_hip_femur	0.82	-0.02	0.94	-0.03	0.94	-0.03	1.00	0.00
R of Ez_hip_femur	0.96	-0.19	0.99	-0.09	0.99	-0.08	1.00	0.00
R of E_hip_femur	0.91	0.00	0.96	0.00	0.97	0.00	1.00	0.00
R of Ex_body	0.86	-0.11	0.94	-0.04	0.94	-0.04	1.00	0.00
R of Ey_body	0.73	-0.19	0.89	-0.08	0.89	-0.07	1.00	-0.01
R of Ez_body	0.96	-0.21	0.98	-0.08	0.98	-0.07	1.00	-0.01
R of E_body	0.80	0.00	0.91	0.00	0.91	0.00	1.00	0.00
R of Ex_head	0.86	-0.05	0.92	-0.10	0.94	-0.08	0.99	-0.01
R of Ey_head	0.88	0.01	0.94	0.01	0.95	0.01	0.99	0.00
R of Ez_head	0.93	-0.04	0.96	-0.08	0.97	-0.05	1.00	-0.01
R of E_head	0.90	0.00	0.95	0.00	0.95	0.00	0.99	0.00
R of Ex_total	0.88	-0.11	0.95	-0.06	0.95	-0.06	1.00	0.00
R of Ey_total	0.80	-0.13	0.92	-0.06	0.92	-0.06	1.00	0.00

Table A-VIII. Correlation coefficients for the FATS model at 600 mm landmark. (continued)

R of Ez_total	0.95	-0.18	0.98	-0.07	0.98	-0.06	1.00	0.00
R of E_total	0.89	0.00	0.95	0.00	0.95	0.00	1.00	0.00
volume weighting	k=1		k=2		k=3		k=8	
Cluster method 3	module	phase	module	phase	module	phase	module	phase
R of Ex_left_arm	0.95	0.02	0.99	-0.04	0.99	-0.02	1.00	-0.01
R of Ey_left_arm	0.92	0.02	0.98	-0.02	0.99	-0.01	1.00	-0.01
R of Ez_left_arm	0.92	-0.09	0.98	-0.03	0.99	-0.01	1.00	0.00
R of E_left_arm	0.93	0.00	0.98	0.00	0.99	0.00	1.00	0.00
R of Ex_right_arm	0.92	0.06	0.99	-0.02	0.99	-0.02	1.00	-0.01
R of Ey_right_arm	0.87	0.01	0.98	-0.01	0.99	-0.01	1.00	0.00
R of Ez_right_arm	0.91	-0.08	0.98	-0.04	0.99	-0.03	1.00	0.00
R of E_right_arm	0.89	0.00	0.98	0.00	0.99	0.00	1.00	0.00
R of Ex_left_tibia	0.84	0.02	0.94	0.05	0.95	0.02	0.99	0.01
R of Ey_left_tibia	0.86	0.09	0.92	0.07	0.94	0.04	0.99	0.01
R of Ez_left_tibia	0.73	0.03	0.84	0.07	0.90	0.01	0.99	0.00
R of E_left_tibia	0.73	0.00	0.86	0.00	0.91	0.00	0.99	0.00
R of Ex_right_tibia	0.97	0.05	0.99	-0.02	0.99	-0.04	1.00	-0.01
R of Ey_right_tibia	0.97	0.02	0.98	0.00	0.99	-0.01	1.00	-0.01
R of Ez_right_tibia	0.79	0.05	0.88	0.04	0.92	0.00	0.99	-0.01
R of E_right_tibia	0.95	0.00	0.97	0.00	0.98	0.00	1.00	0.00
R of Ex_hip_femur	0.87	-0.07	0.99	-0.03	1.00	-0.05	1.00	-0.02
R of Ey_hip_femur	0.82	-0.02	0.99	-0.01	0.99	-0.01	1.00	-0.01
R of Ez_hip_femur	0.96	-0.19	0.99	0.00	1.00	-0.01	1.00	-0.01
R of E_hip_femur	0.91	0.00	0.99	0.00	0.99	0.00	1.00	0.00
R of Ex_body	0.86	-0.11	0.97	-0.03	0.98	-0.02	0.99	0.00
R of Ey_body	0.73	-0.19	0.95	-0.02	0.96	-0.01	0.99	0.00
R of Ez_body	0.96	-0.21	0.99	-0.01	0.99	-0.01	1.00	0.00
R of E_body	0.80	0.00	0.95	0.00	0.97	0.00	0.99	0.00
R of Ex_head	0.86	-0.05	0.94	-0.01	0.95	-0.04	0.99	0.00
R of Ey_head	0.88	0.01	0.95	0.01	0.95	0.01	0.99	0.00
R of Ez_head	0.93	-0.04	0.96	0.02	0.97	-0.01	0.99	-0.01
R of E_head	0.90	0.00	0.95	0.00	0.96	0.00	0.99	0.00
R of Ex_total	0.88	-0.11	0.98	-0.02	0.98	-0.03	1.00	-0.01
R of Ey_total	0.80	-0.13	0.96	-0.01	0.97	-0.01	0.99	0.00
R of Ez_total	0.95	-0.18	0.99	-0.01	0.99	-0.01	1.00	0.00
R of E_total	0.89	0.00	0.97	0.00	0.98	0.00	1.00	0.00

Table A-IX. Correlation coefficients for the FATS model at 800 mm landmark.

landmark at 800 mm								
Cluster method 1	k=1		k=2		k=3		k=8	
Correlation coefficient	module	phase	module	phase	module	phase	module	phase

Table A-IX. Correlation coefficients for the FATS model at 800 mm landmark. (continued)

R of Ex_left_arm	0.95	0.13	0.96	0.12	0.96	0.09	1.00	0.01
R of Ey_left_arm	0.95	0.07	0.97	0.05	0.96	0.04	1.00	0.02
R of Ez_left_arm	0.89	0.01	0.94	0.01	0.94	-0.03	1.00	0.00
R of E_left_arm	0.96	0.00	0.97	0.00	0.97	0.00	1.00	0.00
R of Ex_right_arm	0.91	0.20	0.93	0.19	0.93	0.10	1.00	0.02
R of Ey_right_arm	0.88	0.01	0.92	-0.01	0.92	-0.01	1.00	0.01
R of Ez_right_arm	0.89	-0.04	0.94	-0.03	0.94	-0.07	1.00	0.00
R of E_right_arm	0.90	0.00	0.94	0.00	0.94	0.00	1.00	0.00
R of Ex_left_tibia	0.82	0.15	0.86	0.12	0.86	0.10	0.99	0.04
R of Ey_left_tibia	0.77	0.10	0.84	0.03	0.85	0.04	0.99	0.06
R of Ez_left_tibia	0.67	0.05	0.85	-0.01	0.81	-0.01	0.98	0.05
R of E_left_tibia	0.68	0.00	0.82	0.00	0.79	0.00	0.99	0.00
R of Ex_right_tibia	0.96	-0.07	0.97	-0.12	0.97	-0.07	1.00	0.03
R of Ey_right_tibia	0.95	0.00	0.96	-0.04	0.96	-0.01	1.00	0.03
R of Ez_right_tibia	0.72	0.01	0.86	-0.06	0.83	-0.03	0.98	0.05
R of E_right_tibia	0.91	0.00	0.95	0.00	0.94	0.00	1.00	0.00
R of Ex_hip_femur	0.82	-0.28	0.87	-0.32	0.88	-0.27	1.00	0.03
R of Ey_hip_femur	0.74	-0.18	0.82	-0.24	0.81	-0.20	1.00	0.04
R of Ez_hip_femur	0.94	-0.42	0.96	-0.36	0.96	-0.32	1.00	0.00
R of E_hip_femur	0.84	0.00	0.90	0.00	0.90	0.00	1.00	0.00
R of Ex_body	0.70	-0.11	0.77	-0.15	0.79	-0.20	0.99	0.03
R of Ey_body	0.66	-0.23	0.75	-0.29	0.75	-0.29	0.99	0.03
R of Ez_body	0.92	-0.58	0.95	-0.50	0.95	-0.48	1.00	0.00
R of E_body	0.82	0.00	0.88	0.00	0.88	0.00	1.00	0.00
R of Ex_head	0.82	-0.06	0.85	-0.14	0.86	-0.12	0.99	0.00
R of Ey_head	0.92	0.05	0.93	0.02	0.93	0.02	0.99	0.01
R of Ez_head	0.82	-0.04	0.85	-0.07	0.87	-0.08	0.99	-0.01
R of E_head	0.88	0.00	0.90	0.00	0.91	0.00	0.99	0.00
R of Ex_total	0.79	-0.20	0.84	-0.22	0.85	-0.22	1.00	0.02
R of Ey_total	0.76	-0.15	0.82	-0.18	0.82	-0.18	1.00	0.03
R of Ez_total	0.89	-0.41	0.93	-0.36	0.93	-0.35	1.00	0.00
R of E_total	0.84	0.00	0.90	0.00	0.90	0.00	1.00	0.00
Cluster method 2	k=1		k=2		k=3		k=8	
Correlation coefficient	module	phase	module	phase	module	phase	module	phase
R of Ex_left_arm	0.96	0.02	0.98	0.06	0.98	0.04	1.00	0.00
R of Ey_left_arm	0.95	0.02	0.98	0.03	0.98	0.02	1.00	0.00
R of Ez_left_arm	0.93	-0.08	0.98	0.00	0.99	-0.02	1.00	0.00
R of E_left_arm	0.96	0.00	0.99	0.00	0.99	0.00	1.00	0.00
R of Ex_right_arm	0.92	-0.06	0.97	0.05	0.97	0.00	1.00	0.00
R of Ey_right_arm	0.88	0.01	0.96	0.01	0.96	0.00	1.00	0.00
R of Ez_right_arm	0.91	-0.09	0.98	-0.01	0.98	-0.03	1.00	0.00

Table A-IX. Correlation coefficients for the FATS model at 800 mm landmark. (continued)

R of E_right_arm	0.90	0.00	0.98	0.00	0.97	0.00	1.00	0.00
R of Ex_left_tibia	0.84	0.02	0.94	0.01	0.94	0.02	0.99	0.01
R of Ey_left_tibia	0.85	0.09	0.95	0.00	0.95	0.00	0.99	0.01
R of Ez_left_tibia	0.74	0.01	0.96	-0.03	0.96	-0.02	0.99	0.00
R of E_left_tibia	0.73	0.00	0.96	0.00	0.96	0.00	0.99	0.00
R of Ex_right_tibia	0.97	0.06	0.99	0.00	0.99	0.01	1.00	0.01
R of Ey_right_tibia	0.96	0.05	0.99	0.02	0.99	0.02	1.00	0.01
R of Ez_right_tibia	0.78	0.05	0.97	-0.01	0.97	0.00	0.99	0.00
R of E_right_tibia	0.93	0.00	0.99	0.00	0.99	0.00	1.00	0.00
R of Ex_hip_femur	0.87	-0.05	0.95	-0.08	0.95	-0.07	1.00	0.01
R of Ey_hip_femur	0.76	-0.04	0.92	-0.06	0.92	-0.05	1.00	0.00
R of Ez_hip_femur	0.96	-0.14	0.99	-0.07	0.99	-0.06	1.00	0.00
R of E_hip_femur	0.88	0.00	0.96	0.00	0.96	0.00	1.00	0.00
R of Ex_body	0.82	-0.12	0.92	-0.03	0.93	-0.04	1.00	0.00
R of Ey_body	0.72	-0.15	0.89	-0.07	0.89	-0.07	1.00	-0.01
R of Ez_body	0.96	-0.24	0.98	-0.10	0.98	-0.09	1.00	-0.01
R of E_body	0.85	0.00	0.94	0.00	0.94	0.00	1.00	0.00
R of Ex_head	0.89	-0.04	0.94	-0.10	0.95	-0.08	0.99	-0.01
R of Ey_head	0.92	0.02	0.96	0.02	0.96	0.02	0.99	0.00
R of Ez_head	0.91	-0.08	0.95	-0.17	0.95	-0.12	0.99	-0.01
R of E_head	0.93	0.00	0.96	0.00	0.97	0.00	0.99	0.00
R of Ex_total	0.88	-0.11	0.95	-0.06	0.95	-0.06	1.00	0.00
R of Ey_total	0.81	-0.10	0.93	-0.06	0.93	-0.05	1.00	0.00
R of Ez_total	0.95	-0.17	0.99	-0.08	0.99	-0.07	1.00	0.00
R of E_total	0.89	0.00	0.96	0.00	0.96	0.00	1.00	0.00
Cluster method 3	k=1		k=2		k=3		k=8	
Correlation coefficient	module	phase	module	phase	module	phase	module	phase
R of Ex_left_arm	0.96	0.02	0.99	-0.02	1.00	-0.01	1.00	0.00
R of Ey_left_arm	0.95	0.02	0.99	-0.02	0.99	-0.01	1.00	0.00
R of Ez_left_arm	0.93	-0.08	0.98	-0.03	0.99	-0.01	1.00	0.00
R of E_left_arm	0.96	0.00	0.99	0.00	0.99	0.00	1.00	0.00
R of Ex_right_arm	0.92	-0.06	0.99	-0.05	0.99	-0.02	1.00	-0.01
R of Ey_right_arm	0.88	0.01	0.98	0.00	0.99	0.00	1.00	0.00
R of Ez_right_arm	0.91	-0.09	0.98	-0.05	0.99	-0.03	1.00	0.00
R of E_right_arm	0.90	0.00	0.98	0.00	0.99	0.00	1.00	0.00
R of Ex_left_tibia	0.84	0.02	0.93	0.04	0.95	0.03	0.99	0.01
R of Ey_left_tibia	0.85	0.09	0.91	0.06	0.93	0.03	0.99	0.01
R of Ez_left_tibia	0.74	0.01	0.85	0.04	0.91	0.00	0.99	0.00
R of E_left_tibia	0.73	0.00	0.86	0.00	0.91	0.00	0.99	0.00
R of Ex_right_tibia	0.97	0.06	0.98	-0.03	0.99	-0.05	1.00	-0.01
R of Ey_right_tibia	0.96	0.05	0.98	-0.01	0.98	-0.02	1.00	-0.01

Table A-IX. Correlation coefficients for the FATS model at 800 mm landmark. (continued)

R of Ez_right_tibia	0.78	0.05	0.87	0.03	0.92	-0.01	0.99	0.00
R of E_right_tibia	0.93	0.00	0.96	0.00	0.97	0.00	1.00	0.00
R of Ex_hip_femur	0.87	-0.05	0.99	-0.02	0.99	-0.04	1.00	-0.01
R of Ey_hip_femur	0.76	-0.04	0.97	-0.01	0.98	-0.02	1.00	-0.01
R of Ez_hip_femur	0.96	-0.14	0.99	0.00	1.00	-0.01	1.00	-0.01
R of E_hip_femur	0.88	0.00	0.98	0.00	0.99	0.00	1.00	0.00
R of Ex_body	0.82	-0.12	0.97	-0.03	0.97	-0.02	0.99	0.00
R of Ey_body	0.72	-0.15	0.95	-0.01	0.96	-0.01	0.99	-0.01
R of Ez_body	0.96	-0.24	0.99	-0.02	0.99	-0.02	1.00	-0.01
R of E_body	0.85	0.00	0.97	0.00	0.97	0.00	0.99	0.00
R of Ex_head	0.89	-0.04	0.95	-0.01	0.96	-0.04	0.99	-0.01
R of Ey_head	0.92	0.02	0.96	0.01	0.97	0.01	0.99	0.00
R of Ez_head	0.91	-0.08	0.96	0.07	0.96	-0.01	0.99	-0.02
R of E_head	0.93	0.00	0.97	0.00	0.97	0.00	0.99	0.00
R of Ex_total	0.88	-0.11	0.98	-0.03	0.99	-0.03	1.00	-0.01
R of Ey_total	0.81	-0.10	0.97	-0.01	0.97	-0.01	1.00	0.00
R of Ez_total	0.95	-0.17	0.99	-0.01	0.99	-0.01	1.00	0.00
R of E_total	0.89	0.00	0.97	0.00	0.98	0.00	1.00	0.00

B. Appendix II: The detailed tissues in the two clusters of the chosen tissue-reduced virtual family models at 1.5 T

The detailed tissues in the two clusters and their corresponding parameters of the final chosen tissue-reduced virtual family models are shown in Table to Table for the Duke model, Ella model and FATS model, respectively.

Table B-I. The detailed tissues in the two clusters and their corresponding parameters of the chosen tissue-reduced Duke models.

	Cluster 1	Cluster 2
σ (S/m)	0.11	0.67
ε_r	18.38	76.58
	Air_internal	Adrenal_gland
	Bone	Artery
	Bronchi_lumen	Bladder
	Esophagus_lumen	Blood_vessel
	Fat	Brain_grey_matter
	Lung	Brain_white_matter
	Mandible	Bronchi
	Marrow_red	Cartilage
	Patella	Cerebellum
	Pharynx	Cerebrospinal_fluid
	SAT	Commissura_anterior
	Skull	Commissura_posterior
	Teeth	Connective_tissue
	Trachea_lumen	Cornea
	Vertebrae	Diaphragm
		Ear_cartilage
		Ear_skin
		Epididymis
		Esophagus
		Eye_lens
		Eye_Sclera
		Eye_vitreous_humor
		Gallbladder
		Heart_lumen
		Heart_muscle
		Hippocampus
		Hypophysis

Table B-I. The detailed tissues in the two clusters and their corresponding parameters of the chosen tissue-reduced Duke models. (continued)

		Hypothalamus
		Intervertebral_disc
		Kidney_cortex
		Kidney_medulla
		Large_intestine
		Large_intestine_lumen
		Larynx
		Liver
		Medulla_oblongata
		Meniscus
		Midbrain
		Mucosa
		Muscle
		Nerve
		Pancreas
		Penis
		Pinealbody
		Pons
		Prostate
		Skin
		Small_intestine
		Small_intestine_lumen
		Spinal_cord
		Spleen
		Stomach
		Stomach_lumen
		Tendon_Ligament
		Testis
		Thalamus
		Thymus
		Thyroid_gland
		Tongue
		Trachea
		Ureter_Urethra
		Vein

Table B-II. The detailed tissues in the two clusters and their corresponding parameters of the chosen tissue-reduced Ella models.

	Cluster 1	Cluster 2
σ (S/m)	0.07	0.63

Table B-II. The detailed tissues in the two clusters and their corresponding parameters of the chosen tissue-reduced Ella models. (continued)

ε_r	14.11	72.03
	Bone	Adrenal_gland
	Fat	Air_internal
	Mandible	Artery
	Patella	Bladder
	SAT	Blood_vessel
	Skull	Brain_grey_matter
	Teeth	Brain_white_matter
	Vertebrae	Breast
		Bronchi
		Bronchi_lumen
		Cartilage
		Cerebellum
		Cerebrospinal_fluid
		Connective_tissue
		Cornea
		Diaphragm
		Ear_cartilage
		Ear_skin
		Esophagus
		Esophagus_lumen
		Eye_lens
		Eye_Sclera
		Eye_vitreous_humor
		Gallbladder
		Heart_lumen
		Heart_muscle
		Hippocampus
		Hypophysis
		Hypothalamus
		Intervertebral_disc
		Kidney_cortex
		Kidney_medulla
		Large_intestine
		Large_intestine_lumen
		Larynx
		Liver
		Lung
		Marrow_red
		Medulla_oblongata

Table B-II. The detailed tissues in the two clusters and their corresponding parameters of the chosen tissue-reduced Ella models. (continued)

		Meniscus
		Midbrain
		Mucosa
		Muscle
		Nerve
		Ovary
		Pancreas
		Pharynx
		Pinealbody
		Pons
		Skin
		Small_intestine
		Small_intestine_lumen
		Spinal_cord
		Spleen
		Stomach
		Stomach_lumen
		Tendon_Ligament
		Thalamus
		Thymus
		Thyroid_gland
		Tongue
		Trachea
		Trachea_lumen
		Ureter_Urethra
		Uterus
		Vagina
		Vein

Table B-III. The detailed tissues in the two clusters and their corresponding parameters of the chosen tissue-reduced FATS models.

	Cluster 1	Cluster 2
σ (S/m)	0.07	0.63
ε_r	13.88	72.97
	Fat	Air_internal
	SAT	Bronchi_lumen
	Bone	Esophagus_lumen
	Patella	Pharynx
	Skull	Trachea_lumen
	Teeth	Marrow_red

Table B-III. The detailed tissues in the two clusters and their corresponding parameters of the chosen tissue-reduced FATS models. (continued)

	Vertebrae	Humerus_marrow_left
	Humerus_left	Humerus_marrow_right
	Humerus_right	Tibia_marrow_left
	Tibia_left	Tibia_marrow_right
	Tibia_right	Fibula_marrow_left
	Fibula_left	Fibula_marrow_right
	Fibula_right	Femur_marrow_left
	Femur_left	Femur_marrow_right
	Femur_right	Calcaneus_marrow_left
	Calcaneus_left	Calcaneus_marrow_right
	Calcaneus_right	Talus_marrow_left
	Talus_left	Talus_marrow_right
	Talus_right	Ulna_marrow_right
	Cochlea_Ductus_semicirculares	Radius_marrow_right
	Ulna_right	Ulna_marrow_left
	Radius_right	Radius_marrow_left
	Metacarpus_I_right	Eye_lens
	proximalis_I_right	Bladder
	proximalis_II_right	Lung
	proximalis_III_right	Brain_white_matter
	proximalis_IV_right	Commissura_anterior
	proximalis_V_right	Commissura_posterior
	media_II_right	Nerve
	media_III_right	Spinal_cord
	media_IV_right	Penis
	media_V_right	Ureter_Urethra
	distalis_I_right	Ductus_deferens
	distalis_II_right	Ear_skin
	distalis_III_right	Skin
	distalis_IV_right	Liver
	distalis_V_right	Cartilage
	Ulna_left	Ear_cartilage
	Radius_left	Intervertebral_disc
	Metacarpus_I_left	Larynx
	proximalis_I_left	Meniscus
	proximalis_II_left	Connective_tissue
	proximalis_III_left	Tendon_Ligament
	proximalis_IV_left	Mucosa
	proximalis_V_left	Brain_grey_matter
	media_II_left	Hippocampus

Table B-III. The detailed tissues in the two clusters and their corresponding parameters of the chosen tissue-reduced FATS models. (continued)

	media_III_left	Thalamus
	media_IV_left	Bronchi
	media_V_left	Trachea
	distalis_I_left	Large_intestine
	distalis_II_left	Tongue
	distalis_III_left	Heart_muscle
	distalis_IV_left	Diaphragm
	distalis_V_left	Large_intestine_lumen
		Muscle
		Small_intestine_lumen
		Stomach_lumen
		Cerebellum
		Midbrain
		Pons
		Medulla_oblongata
		Kidney_cortex
		Kidney_medulla
		Spleen
		Adrenal_gland
		Hypophysis
		Hypothalamus
		Pancreas
		Thyroid_gland
		Pinealbody
		Nodus_lymphaticus
		Parotid_gland
		Esophagus
		Stomach
		Eye_Sclera
		Epididymis
		Prostate
		Testis
		Glandula_vesiculosa
		Cornea
		Artery
		Heart_lumen
		Vein
		Gallbladder
		Eye_vitreous_humor
		Small_intestine
		Cerebrospinal_fluid

C. APPENDIX III: CONVERGENCE CHECK FOR MESH SIZE

The maximum mesh size for the human models was set to 2 mm to balance the accuracy of results and time for simulation. More simulations were conducted with mesh size set to 1.5 mm, 2.5 mm, and 3 mm. The device used for the mesh study is the plate and screw system implanted on the rib in the Duke model at 0 mm landmark position. The device and results are shown in Figure C-1.

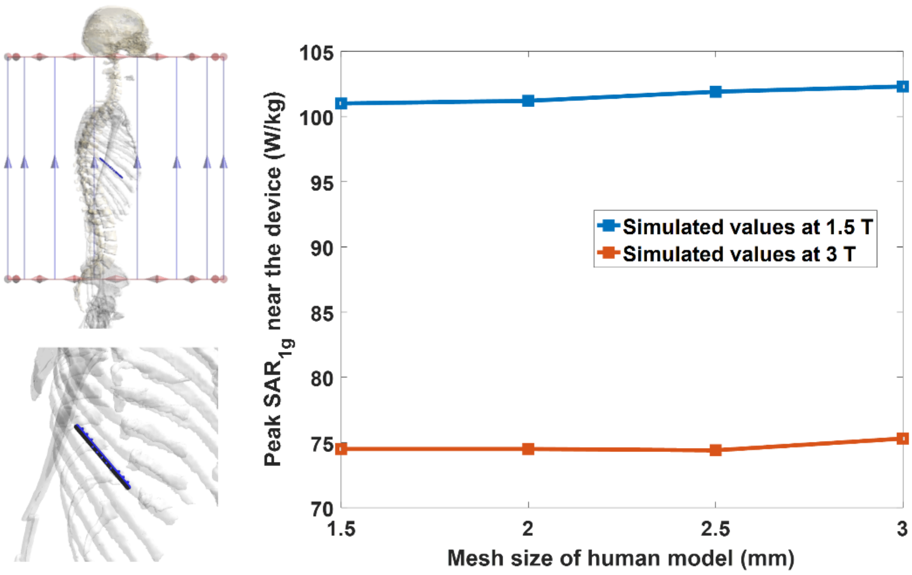

Figure C-1. The device used for mesh study and results of the peak SAR_{1g} near the device.

Compared to the values of peak SAR_{1g} near the device at 1.5 mm mesh size, the values of peak SAR_{1g} near the device at 2 mm mesh size have relative errors as 0.2% at 1.5 T and 0% at 3 T.

The ASTM phantom was used to investigate the mesh size's influence on the incident electric field. The mesh size for the gel was set to 1 mm, 2 mm, 2.5 mm and 5 mm. The curves of the modulus of tangential incident electric field at 3 T are shown in Figure C-2. The relative errors between the tangential incident electric field with 2 mm mesh size and with 1 mm mesh size is less than 1%. Thus the 2 mm mesh size is acceptable for the analysis of tangential incident electric field at 3 T. And the wavelength at 1.5 T is larger than that at 3 T, so the 2 mm mesh size is also acceptable at 1.5 T.

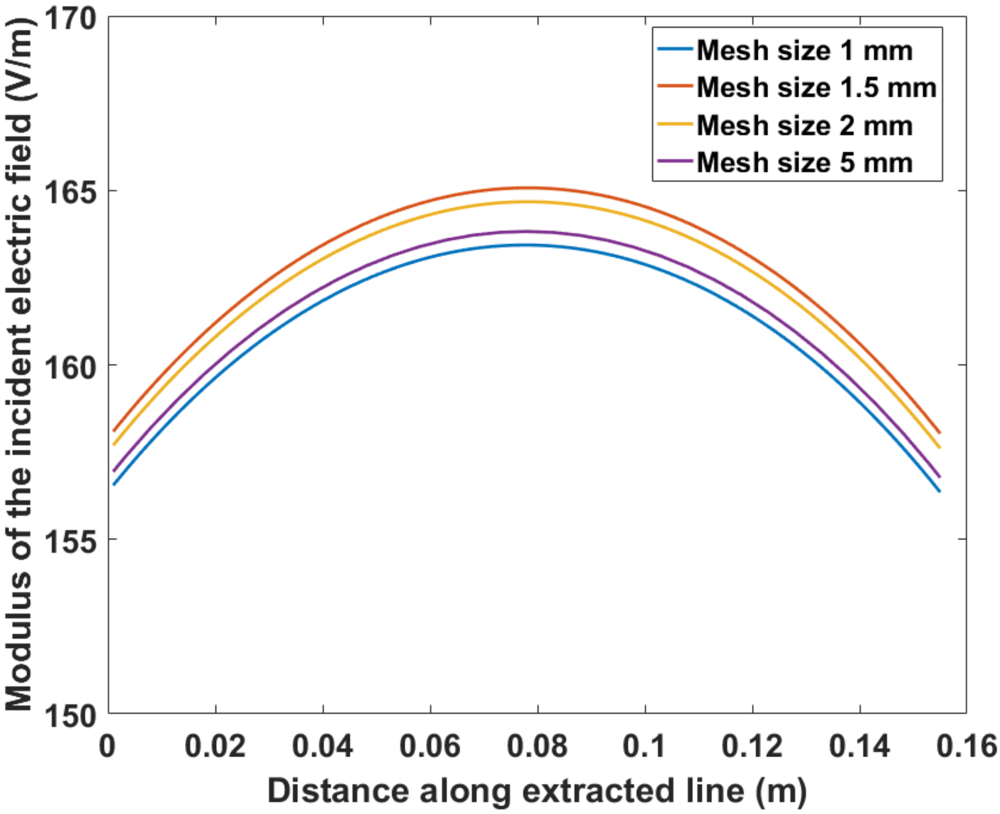

Figure C-2. Results of the modulus of the tangential incident electric field in ASTM phantom.

D. APPENDIX IV: UNCERTAINTY ANALYSIS

The uncertainty analysis was conducted for this study to consider the uncertainty coming from the loading position of the human models and the device, the grid resolution of the human models and the device, and the human tissues' properties. These uncertainty sources in this study were considered independent and the combined uncertainty was calculated as [53], [54]

$$u_c(y) = \sqrt{\sum_{i=1}^{m} c_i^2 \cdot u^2(x_i)}, \quad \text{(D-1)}$$

where the y is a function of m parameters x_1, x_2, …, x_m, c_i is the sensitivity coefficient calculated by $\partial y/\partial x_i$, $u(x_i)$ is the standard uncertainty of each parameter and $u_c(y)$ is the combined uncertainty. In this study, the function y is the value of peak SAR_{1g} near the device. To get the ∂y, the plate and screw system implanted on the rib in the Duke model at 0 mm landmark was used for simulations.

For the loading position of human models as the parameters x_i, the Duke model was moved by 20 mm in *x*, *y*, and *z* directions and the ∂x_i is 20 mm. For the loading position of device, the device was moved by 1 mm in *x*, *y*, and *z* directions and the ∂x_i is 1 mm. For the grid resolution, the mesh size of the human model was changed by 0.5 mm (∂x_i is 0.5 mm) and the mesh size of the device was changed by 0.1 mm (∂x_i is 0.1 mm). The main tissues near the hotspot are the bone, muscle, and skin. Thus, their properties were considered for this uncertainty analysis. The electrical conductivities, relative permittivities of these tissues were changed by 25% at 1.5 T (∂x_i is 25%) and 10% at 3 T (∂x_i is 10%)

[55]. The densities of these tissues were changed by 7% (∂x_i is 7%) at 1.5 T and 3 T based on the IT'IS database [56]. Assuming that all the parameters are uniform distributions, the standard uncertainty of each parameter can be calculated by the upper and lower limits of the parameter [54], which is the $\partial x_i/\sqrt{3}$.

The data of the parameter variation (∂x_i), SAR_{1g} variation (∂y), sensitivity coefficients ($\partial y/\partial x_i$) and standard uncertainty of each parameter ($u(x_i)$) are shown in Table D-I for 1.5 T and Table D-II for 3 T.

Table D-I. Data for combined uncertainty calculation at 1.5 T.

Loading position					
	Direction	∂x_i (mm)	∂y (W/kg)	$\partial y/\partial x_i$	$u(x_i)$ (mm)
Human position	x	20	-2.6	-0.13	11.55
	y	20	3.1	0.16	11.55
	z	20	-2.7	-0.13	11.55
Device position	x	1	1.5	1.51	0.58
	y	1	0.3	0.26	0.58
	z	1	-0.8	-0.76	0.58
Grid resolution					
		∂x_i (mm)	∂y (W/kg)	$\partial y/\partial x_i$	$u(x_i)$ (mm)
Maximum mesh size	Human	0.5	0.7	1.41	0.29
	Device	0.1	-0.6	-6.15	0.06
Human tissues' properties					
Tissues	Properties	∂x_i	∂y (W/kg)	$\partial y/\partial x_i$	$u(x_i)$
Bone	σ	25%	-0.3	-1.08	14.43%
	ε_r	25%	1.7	6.79	14.43%
	ρ	7%	0.6	8.36	4.04%
Muscle	σ	25%	-0.3	-1.10	14.43%
	εr	25%	4.3	17.27	14.43%
	ρ	7%	0.2	3.43	4.04%
Fat	σ	25%	0.0	0.04	14.43%
	εr	25%	1.2	4.90	14.43%
	ρ	7%	1.0	13.72	4.04%

Table D-II. Data for combined uncertainty calculation at 3 T.

Loading position					
	Direction	∂x_i (mm)	∂y (W/kg)	$\partial y/\partial x_i$	$u(x_i)$ (mm)
Human position	x	20	1.1	0.05	11.55
	y	20	3.6	0.18	11.55
	z	20	1.6	0.08	11.55
Device position	x	1	1.2	1.23	0.58
	y	1	0.4	0.44	0.58
	z	1	-0.3	-0.27	0.58
Grid resolution					
		∂x_i (mm)	∂y (W/kg)	$\partial y/\partial x_i$	$u(x_i)$ (mm)
Maximum mesh size	Human	0.5	-0.1	-0.13	0.29
	Device	0.1	-0.6	-5.71	0.06
Human tissues' properties					
Tissues	Properties	∂x_i	∂y (W/kg)	$\partial y/\partial x_i$	$u(x_i)$
Bone	σ	10%	-0.3	-2.58	5.77%
	ε_r	10%	0.1	1.12	5.77%
	ρ	7%	0.4	6.11	4.04%
Muscle	σ	10%	-4.4	-43.96	5.77%
	εr	10%	0.4	4.41	5.77%
	ρ	7%	0.2	2.58	4.04%
Fat	σ	10%	-0.4	-3.91	5.77%
	εr	10%	0.4	4.08	5.77%
	ρ	7%	0.1	1.54	4.04%

Based on the data in Table D-I and Table D-II and the formula (D-1), the combined uncertainties were calculated as 4.12% at 1.5 T and 4.86% at 3 T.

E. Appendix V: The SAR_{1G} in tissue-reduced human models with and without Σ-scaling vs. the SAR_{1G} in original human models

To show that the σ-scaling is needed and useful, the SAR_{1g} in the tissue-reduced human models with and without σ-scaling vs. the SAR_{1g} in the original human model at 1.5 T is shown in Figure E-1. The σ-scaling does not help the correlation coefficient for the shown results, but it makes the slope of the fitting straight line closer to 1. It means that the fitting straight line of the data is closer to the y=x line with the σ-scaling. Thus, the σ-scaling makes the values of SAR_{1g} in tissue-reduced human models generally match better with those in original human models based on the slopes of the fitting straight lines. However, the σ-scaling used in this study has its limits. For some studied cases, the relative errors between the SAR_{1g} in the tissue-reduced human models and the SAR_{1g} in the original human models become larger with the σ-scaling. These cases are listed in Table E-I. For around 2/3 of all studied cases, the relative errors between the SAR_{1g} values in the tissue-reduced human models and the SAR_{1g} values in the original human models are smaller with the σ-scaling than those without the σ-scaling. The proposed σ-scaling is a simple method to calibrate the influence of surrounding tissues' electrical conductivities on the SAR. In this study, the values of electrical conductivities used for the σ-scaling were the averaged values in a 10 mm * 10 mm * 10 mm cubic near the hotspots. But the tissues inside the cubic can be very complex and the averaged electrical conductivities may not be accurate enough. In detail, assuming that one hotspot is near the tip of the device, the electrical conductivity of the tissue wrapping the tip could be significantly different from the averaged electrical conductivity in the cubic. That will lead to some inaccuracy in the scaled results. More improvements may be necessary in the future for this scaling method to increase the accuracy of the used electrical conductivities.

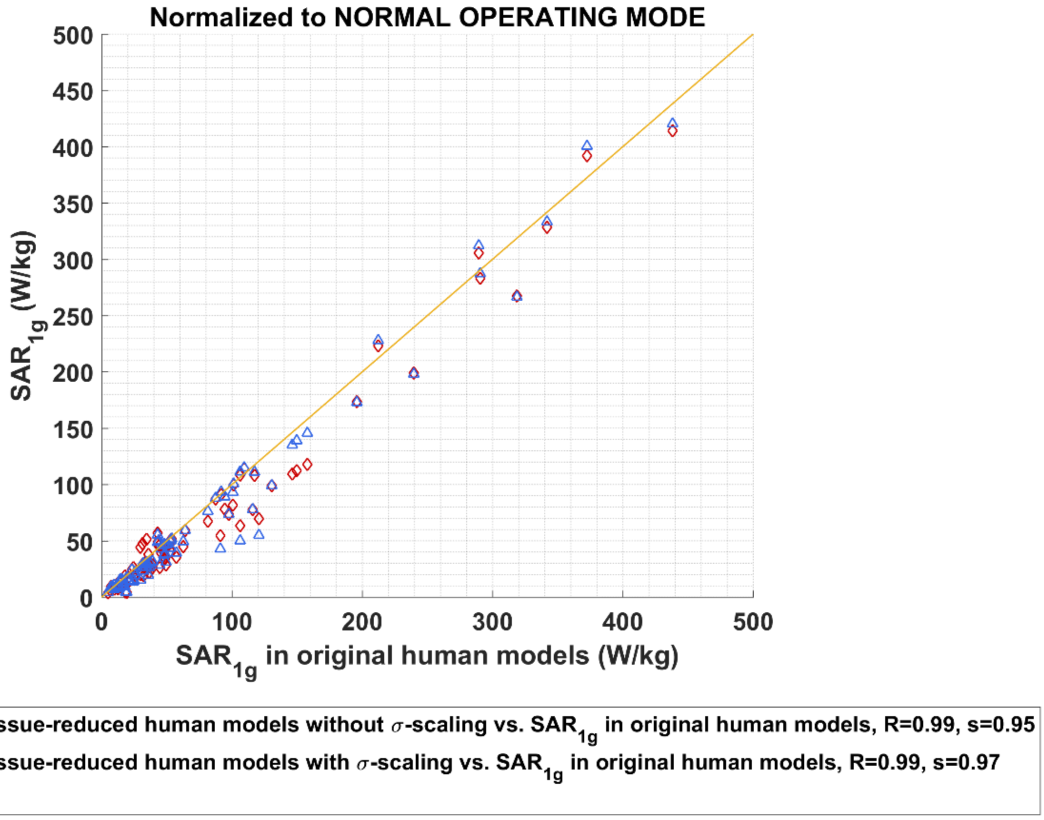

Figure E-1. The SAR_{1g} in the tissue-reduced human models with and without σ-scaling vs. the SAR_{1g} in the original human models.

Table E-I. Results for the cases when the relative errors between the SAR_{1g} in the tissue-reduced human models and the SAR_{1g} in the original human models become larger with the σ-scaling.

Human models, device, implanted region, landmark position	SAR_{1g} in original human models (W/kg)	Averaged σ in original human models (S/m)	SAR_{1g} in tissue-reduced human models without σ-scaling (W/kg)	Averaged σ in tissue-reduced human models (S/m)	SAR_{1g} in tissue-reduced human models with σ-scaling (W/kg)	Relative errors without σ-scaling	Relative errors with σ-scaling
Duke, screw, ankle, 0 mm	24.5	0.21	18.0	0.33	13.6	-26.37%	-44.47%
Duke, screw, ankle, 100 mm	30.1	0.21	20.1	0.33	15.1	-33.21%	-49.83%
Duke, screw, ankle, -100 mm	24.9	0.21	19.3	0.33	14.5	-22.67%	-41.84%
Duke, plate and screw, C4, 0 mm	31.9	0.61	29.8	0.62	29.7	-6.61%	-6.98%
Duke, plate and screw, C4, 100 mm	21.9	0.49	15.0	0.57	14.2	-31.46%	-35.11%
Duke, plate and screw, fibula, 0 mm	239.6	0.62	198.9	0.63	198	-17.00%	-17.36%
Duke, plate and screw, fibula, 100 mm	318.6	0.62	267.5	0.63	266.3	-16.04%	-16.43%

Table E-I. Results for the cases when the relative errors between the SAR_{1g} in the tissue-reduced human models and the SAR_{1g} in the original human models become larger with the σ-scaling. (Continued)

Duke, plate and screw, fibula, -100 mm	195.9	0.62	173.7	0.63	172.9	-11.34%	-11.76%
Duke, plate and screw, rib, -100 mm	109.3	0.56	114.0	0.55	114.8	4.33%	5.05%
Ella, pedicle screw, neck, 100 mm	91.8	0.68	91.1	0.62	93.5	-0.69%	1.89%
Ella, pedicle screw, neck, -100 mm	106.4	0.68	108.4	0.62	111.2	1.86%	4.49%
Ella, screw, ankle, 0 mm	32.8	0.40	30.0	0.43	29.1	-8.34%	-11.15%
Ella, screw, ankle, -100 mm	31.7	0.40	27.6	0.43	26.8	-12.87%	-15.52%
Ella, screw, pelvic, 100 mm	13.9	0.57	14.5	0.53	14.8	4.37%	6.80%
Ella, plate and screw, fibula, 0 mm	289.4	0.65	305.7	0.60	312.2	5.65%	7.88%
Ella, plate and screw, fibula, 100 mm	372.6	0.65	392.0	0.60	400.4	5.22%	7.47%
Ella, plate and screw, fibula, -100 mm	212.3	0.65	223.2	0.60	227.9	5.15%	7.37%

Table E-I. Results for the cases when the relative errors between the SAR_{1g} in the tissue-reduced human models and the SAR_{1g} in the original human models become larger with the σ-scaling. (Continued)

Ella, plate and screw, rib, 0 mm	106.2	0.35	63.3	0.59	50	-40.41%	-52.92%
Ella, plate and screw, rib, 100 mm	91.2	0.35	54.5	0.59	43	-40.30%	-52.86%
Ella, plate and screw, rib, -100 mm	120.7	0.35	69.5	0.59	54.9	-42.41%	-54.51%
FATS, pedicle screw, neck, 100 mm	43.8	1.01	45.5	0.61	49.9	3.91%	13.90%
FATS, screw, ankle, 0 mm	24.3	0.12	26.2	0.30	13.4	8.10%	-44.81%
FATS, screw, ankle, 100 mm	36.0	0.12	38.1	0.30	19.4	5.96%	-46.10%
FATS, screw, ankle, -100 mm	17.9	0.12	18.7	0.31	9.4	4.67%	-47.44%
FATS, screw, pelvic, 0 mm	10.7	0.50	8.6	0.51	8.6	-19.56%	-19.73%
FATS, screw, pelvic, 100 mm	17.4	0.48	13.1	0.50	12.9	-24.30%	-25.69%
FATS, screw, pelvic, -100 mm	9.8	0.48	6.9	0.50	6.8	-28.95%	-30.29%

Table E-I. Results for the cases when the relative errors between the SAR_{1g} in the tissue-reduced human models and the SAR_{1g} in the original human models become larger with the σ-scaling. (Continued)

FATS, plate and screw, C4, 0 mm	6.7	0.50	6.5	0.32	8.1	-3.12%	21.24%
FATS, plate and screw, C4, 100 mm	8.2	0.51	7.8	0.33	9.7	-4.77%	18.62%